university of groningen / faculty of mathematics and natural sciences / kapteyn astronomical institute

Master thesis

Backreaction in cosmic Swiss cheese

Author:
Hans Buist

Supervisor:
Rien van de Weijgaert

February 26, 2011

Contents

1 Introduction

Cosmology, from the Greek *kosmos* (universe) and *logia* (knowledge), is the science that tries to understand the universe as a whole. Ever since ancient times we have been trying to understand the universe and our place within the cosmos. With the advent of precision cosmology, our universe seems to be known better than ever before. The sky is observed with unprecedented detail, allowing us to look back in time almost to the Big Bang.

At the same time we have realized that the largest part of our universe is not understood. The latest results from observations of the Cosmic Microwave Background (Komatsu et al. 2011) show that the energy content of the universe consists for less than 5% of ordinary baryons. On the other hand, 22% of the content is dark matter, which is the matter that is predicted to explain the observed motion of stars and galaxies. But an overwhelming 73% of the content is dark energy, which is the energy required to explain the (accelerating) expansion of our universe.

While dark matter can be explained with new fundamental particles that may perhaps be found in collider experiments, dark energy poses a much larger problem for cosmology. This master thesis revolves around one alternative for dark energy, developed by Thomas Buchert, the so-called *cosmic backreaction*. In the following paragraphs we will see how we reached the age of precision cosmology, starting with the ancient times. After that, we will have a short introduction to alternatives of dark energy (including cosmic backreaction). The last part of the introduction will feature the overview of the research project.

1.1 A changing view of the cosmos

For the ancients, not only the sky was the limit, but also the eye was the limit. Our eyes limited us to observing the moon, the sun, the wandering planets and the distant fixed stars in the 'heavens'. Very often, the 'heavens' were seen like a dome over the Earth, fitted with small bright lights. In this context it is not surprising that the geocentric view on the cosmos by Ptolemaeus would be the dominant for many centuries (see figure 1.1).

Figure 1.1: Ptolemaic view of the universe with the Earth at the centre. This early solar system model relied heavily on epicycles. These are small circular orbits that an object makes while it orbits Earth. We know today that the orbits of planets are elliptical. Sometimes 'adding epicycles' is used to refer to repairing badly designed theories using increasingly more new features. This unfair, because we can show that epicycles are comparable to the first two terms of a Fourier series of an ellipse. This means that epicycles are the second order approximation of an ellipse. (Image by Peter Apian, *Cosmographia*, Antwerp 1524)

In the Age of Enlightenment a renewed interest in science appeared with a greater focus on systematic observation and rational explanation. One of the first new ideas to spread through Europe was the heliocentric model by Niklaus Copernicus. His idea was again based on circular orbits, which can not fit the observations better than the geocentric model. The heliocentric model did not get a rigid foundation until Johannes Kepler empirically discovered his laws of planetary motion. He proved that the orbit of planets are elliptical, without the need for epicycles (see also Stanton 2011).

The discovery of the telescope at the beginning of the 17th century further boosted the exploration of the cosmos. Soon after Galileo Galilei started observing with his self-built telescope, he discovered the moons of Jupiter and the phases of Venus. This was the first evidence that not all heavenly bodies orbited Earth. He also discovered that the Milky Way was not a smooth cloud, but a dense collection of stars. His discoveries changed the view of the cosmos, and indicated that perhaps the Earth was not central in the cosmos. This lead to a growing acceptance of Copernicus' ideas.

Kepler's findings would stand at the basis for the postulation of the gravitational inverse-square force law by Robert Hooke. A real breakthrough came when Isaac Newton combined these ideas in his Principia into a comprehensive work on the laws of motion. In this work Newton carefully explained how the motion of planets can be explained using the universal law of gravity. The impact of his Principia was enormous and would lay the foundations of modern physics.

The heliocentric model also did a prediction which would turn out very useful. Given that the Earth orbits the Sun in one year, one expects that nearby objects move with respect to the distant background during the year. This displacement, or "parallax" is inversely proportional to the distance of the object, so that the parallax can be used to infer distances. It did take until 1838 when Friedrich Bessel made the first successful observation of a stellar parallax. It was realized that our solar system resides in the Milky Way, which was found to be an enormous disk of stars and gas.

Figure 1.2: Panorama view of the Milky Way (image by ESO) with many dust clouds near the disk. The early studies by Jacobus Kapteyn had underestimated galactic extinction to such an extent that the galaxy seemed much smaller than it actually is. The dusty clouds in the galaxy especially obscure much light towards the disk of the Milky Way. Observations of the Galactic Halo would eventually lead to the discovery of Kapteyn's underestimation.

In 1916, Jacobus Kapteyn took the effort to organise the first international collaboration to map out the stars in the Milky Way. He found that the galaxy was lens shaped, 40,000 light years across and with the Sun 2,000 light years from the centre (Kapteyn 1922). Strangely, the density seemed to increase away from the centre. Soon thereafter it was realized that the model was wrong because interstellar dust had blocked our line of sight (see figure 1.2). Above and below the Milky Way, dense groups of stars had been observed, the globular clusters. These groups were found far beyond the edge of the Kapteyn universe. The understanding of our galaxy changed dramatically when astronomers realized that globular clusters were in fact part of the Milky Way. The Milky Way was found to be at least 100,000 light years across with the Sun 30,000 light years away from the galactic centre. It had become clear that not even our Sun was in the centre of the universe.

The exploration of the cosmos continued with further observations of nebulae. Nebulae were extended dim objects with a gaseous appearance, which we now know includes galaxies and planetary nebulae. The discovery of spectral lines in the Sun by Joseph von Fraunhofer proved important for understanding nebulae. It was found that a large portion of them had spectra just like our Sun and other stars. At the time it was not known how far away these nebulae were. Either the Milky Way was the whole universe, and nebulae were part of it, or the nebulae were themselves "island universes" like our own Milky Way, residing much further away.

This debate was resolved in 1924 when the first Cepheid stars were found in the Andromeda Galaxy (M31) by Edwin Hubble. Cepheids are stars which pulsate at a frequency directly related to their luminosity. Knowing their intrinsic luminosity then allows the estimation of their distance, which proved that M31 should lie far beyond the edge of the Milky Way. So the further we explored space, the more we realized that we do not live in a special place in the universe.

1.2 Relativistic Cosmology

In 1916, Albert Einstein presented his General Relativity theory which attempted to bring gravity and special relativity together. It only took him until 1917 to apply his new theory to the cosmos as a whole, thereby starting the field of relativistic cosmology. In his theory he assumed that the universe was static, as the velocities observed in the galaxy seemed relatively low. He also assumed the universe to be of finite extent, with an isotropic and homogeneous density. On the smallest scales the universe was clearly not uniform, but just like we can take the shape of the Earth as a sphere (ignoring mountains), we can also assume the universe to be homogeneous. To keep the universe static, he took the freedom to introduce the cosmological constant Λ in his field equations. This constant matched with the density so that the universe would not expand or contract.

But the assumption of a static universe proved wrong. Already in 1915, Vesto Slipher published an article in which he showed that the shift of absorption lines in some nebulae corresponds with large recession velocities, but no explanation was found for this phenomena. In 1922, Alexander Friedmann found a solution to Einsteins field equations for an expanding space with a uniform and isotropic density. Independently, Georges Lemaître, a Belgian priest, discovered the same solution in 1927. He realized that an expanding space might explain the observation of the recession velocities of galaxies. This was settled in 1929 when Edwin Hubble published his results which clearly indicated that an approximately linear relation existed between distance and recession velocity. This led Einstein to withdraw his cosmological constant, because it had no use anymore.

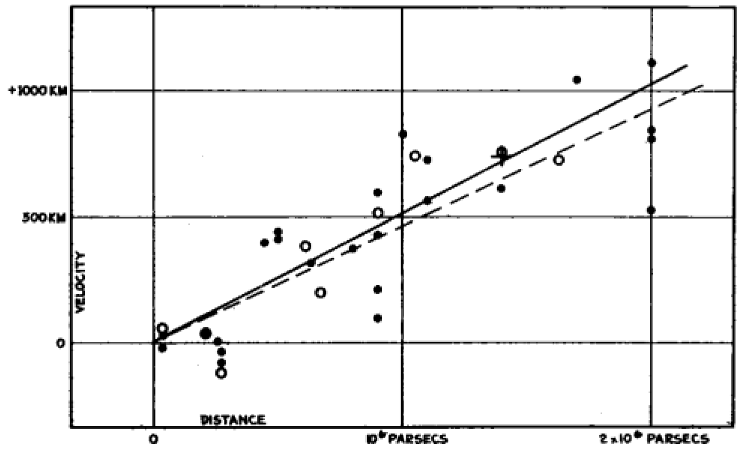

Figure 1.3: The Hubble diagram (Hubble 1929). In this diagram, Edwin Hubble showed the linear relation between the distance of galaxies and their recession velocity. The proportionality constant between recession velocity and distance is known as the Hubble constant H_0. The estimate by Hubble for H_0 was approximately 500 km/s/Mpc, but it proved to be too large, mainly due to systematic errors. Only in recent years, convergence is seen in the value for H_0 around 70 km/s/Mpc, while before the value ranged between 50 and 90 km/s/Mpc. The main problem was that the distance calibration depends on certain astrophysical characteristics of stars, making the estimate difficult if the necessary astrophysics are not known precisely.

The discovery of the expanding universe led to the postulation that the universe started in a point, the Big Bang (first called the primeval atom). Another point of evidence for this idea came when two radio astronomers, Arno Penzias and Robert Wilson, serendipitously discovered relic radiation of the Big Bang. This relic radiation, or Cosmic Microwave Background (CMB), had already been predicted in 1948 by cosmologists Gamow, Alpher and Herman. It took until the 1960s when the work of Zel'dovich, Peebles and Dicke led to a real interest in observing the effect. They predicted a black body spectrum at a temperature of around 5 K with tiny temperature fluctuations imposed. The CMB was created when electrons and protons for the first time combined to form hydrogen. This decoupled the electrons and photons, causing them to stream freely through the universe. The fluctuations in the CMB are mainly caused by the imprint of density fluctuations in the primordial plasma. A smaller contribution comes from distortions by high-energy electrons in galaxy clusters (the Sunyaev-Zel'dovich effect). This distortion occurs when the CMB photons cross clusters when moving towards us.

1.3 Into the dark: The advent of dark energy

The discovery of the CMB led the way for doing precision cosmology. A lot of effort was put into the exact measurement of the CMB and its fluctuations. It was not until 1992 when the team of the Cosmic Background Explorer (COBE) published the first observation of the anisotropies of the CMB (see figure 1.4). The CMB was found to be an almost perfect black body with a temperature of 2.725 K. It was almost isotropic, with very tiny fluctuations of order 10^{-5}. The fluctuations were found to be Gaussian in nature and thought to have been generated by quantum noise. These fluctuations were expanded by a factor 10^{60} in a short inflationary phase just after the Big Bang. This would also explain why the fluctuations were so extremely small, causing the universe to be almost exactly isotropic.

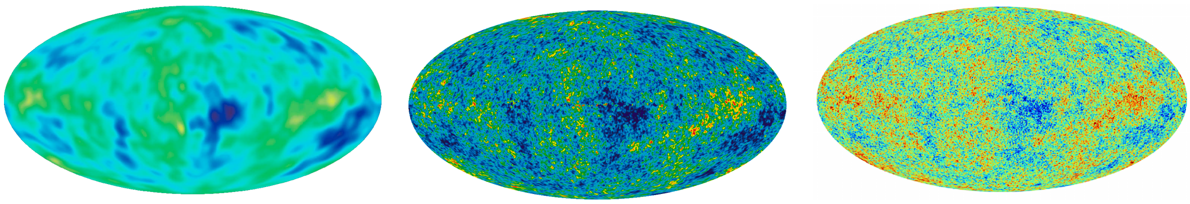

Figure 1.4: 20 Years of observing the Cosmic Microwave Background. Left: The Cosmic Background Explorer (COBE) satellite was launched in 1989 and proved the first detection of the full blackbody spectrum and its fluctuations. Middle: The Wilkinson Microwave Anisotropy Probe (WMAP) was launched in 2001 and became a great improvement over COBE, opening up the era of precision cosmology. Right: The Planck satellite was launched in 2009 and will hopefully improve the resolution even more. This image shows a simulation of the detail at which we may be probing the CMB. The more precise the observations become, the better we can understand the primordial densities, but also the effect from nearby large structures on the CMB.

Another important observable are supernovae IA: luminous explosions of white dwarf stars that accreted matter from a binary companion until they reach the Chandresakhar mass ($\approx 1.4 M_{\odot}$). The light emission from a supernova is characteristic for its intrinsic luminosity, so that the brightness observed on Earth is a direct measure of its distance. In 1998 and 1999, two large surveys of very distant supernovae were presented which indicated that the supernovae were much dimmer than expected (Riess et al. 1998; Perlmutter et al. 1999, see figure 1.5). This could be explained if the expansion of the universe was accelerating.

Until 1998, cosmologists had expected that the universe was decelerating, but this was apparently wrong. To explain the acceleration, the cosmological constant Λ had to be reintroduced, now as 'dark energy'. This time the effect was not to keep the universe static, but to make it expand much faster. Dark energy is a dynamical feature in cosmology, which is present everywhere and has a negative pressure. This negative pressure is unlike anything we know in ordinary physics, and tends to push the universe apart. The difference between Λ and dark energy is that the cosmological constant is a geometrical constant, while dark energy is dynamic. This will become more clear in the next chapter.

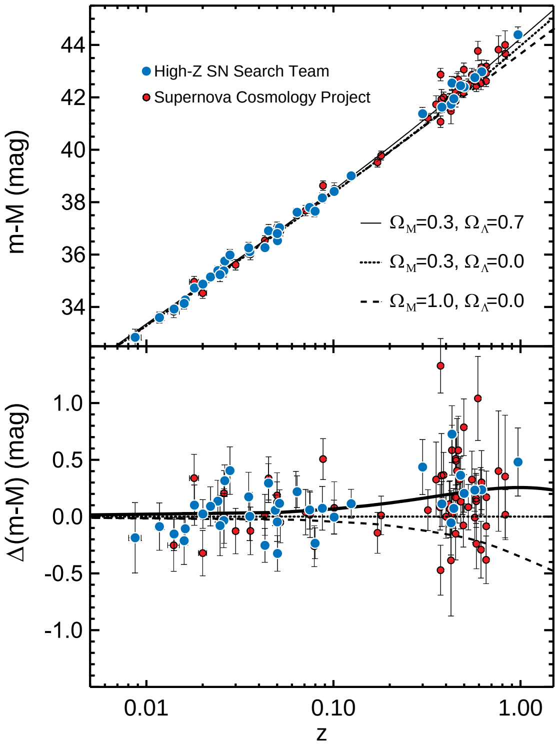

Figure 1.5: The Hubble diagrams from the High Z Supernovae Team (Riess et al. 1998) and the Supernovae Cosmology Project (Perlmutter et al. 1999). The upper diagram shows the observed luminosity-redshift relation compared with an accelerating ΛCDM universe, an open universe and an Einstein-de Sitter universe (the next chapter explains these further). The bottom diagram shows the same results, but with the expectations for an open universe subtracted. The observations seem to indicate that the expansion of the universe is accelerating. The large scatter is probably caused by anisotropies of the Hubble flow on the sky (McClure & Dyer 2007).

In 2001 the Wilkinson Microwave Anisotropy Probe (WMAP) was launched, the successor of COBE, which could measure the CMB with much higher precision. The first results from WMAP came in 2003 (Spergel et al. 2003). The most valuable information of the CMB is found using a decomposition in spherical harmonics, resulting in the so-called *power spectrum*. The power at different spatial frequencies can be directly related to several cosmological parameters, including the curvature of space. WMAP found that the universe is flat to within 1%. This number is determined by the density of matter and dark energy, and together with the Supernovae result, it was found that dark energy represents a staggering 73% of the content of the universe with matter making up the the remaining 27%.

Another line of work came through the work on the Big Bang nucleosynthesis (Schramm & Turner 1998). By carefully observing the abundances of elements in the universe such as Deuterium, Helium and Lithium, it was found that the universe should contain about 5% baryonic matter, of which about 0.4% has already been observed as stars, planets and gas. The remaining part of the matter should be there, but its identity remains unknown. The baryonic part is likely to be intergalactic gas, while the non-baryonic part is postulated as 'dark matter'. Dark matter is gravitationally present, but barely interacts with other particles otherwise.

Due to the constraints on the formation of galaxies, the currently accepted paradigm is that of *cold* dark matter. In this case, *cold* means particles that were non-relativistic at the moment of recombination, as opposed to *warm* or *hot* dark matter, which moved at relativistic velocities at recombination. If particles are too 'warm', then the (dominant) dark matter particles would smooth out the structures in the primordial plasma, possibly preventing even the formation of large structures such as galaxies.

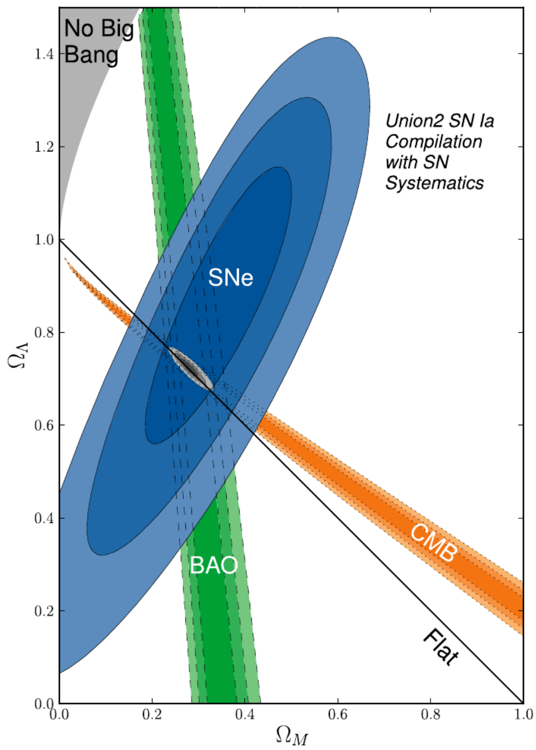

Figure 1.6: Likelihood plot of the dark energy content Ω_Λ vs matter content Ω_m with 1, 2 and 3-σ error contours. This image shows the results for distant supernovae (SNe), Cosmic Microwave Background (CMB) and the large scale structure (BAO). The small grey circle in the middle shows the combined result for all data sets, clearly pointing towards a universe which is dominated by dark energy (Amanullah et al. 2010)

The match with other projects that investigated cosmology would turn out to be remarkable (see figure 1.6). Years of observing the large scale distribution of matter with the Sloan Digital Sky Survey confirmed that about 1/3 of the universe consisted of matter (Tegmark et al. 2004). At the same time, the distribution still contains much information about the initial density field through so-called Baryonic Acoustic Oscillations (BAO's, see Eisenstein et al. 2005). These oscillations are 'acoustic waves' from the primordial plasma that were frozen into the matter distribution at the time of recombination. The result is a stronger correlation between structures today at distance of around 150 Mpc, making the BAO's a cosmic ruler.

Combining the evidence, we arrive at the 'concordant ΛCDM cosmology', which currently gives us the following characteristic results of our universe:

- the age of the universe is 13.7 billion years;
- the universe is flat within 1%;
- less than 5% of the energy content of the universe is made up of baryons;
- dark matter takes up 22 % of the universe;
- dark energy takes up 73 % of the universe.

1.4 Fundamental issues with dark energy and dark matter

Dark energy, has been thoroughly investigated by theoreticians. The closest we have come in our understanding is dark energy as a cosmological vacuum energy. But any realizable concept of this in particle physics is still many orders of magnitude larger (10^{120}) than the cosmological constant. An alternative to this is seeing dark energy as a time-evolving field. This is known as 'quintessence' (literally: fifth element), and behaves as an anti-gravity field. But apart from introducing more degrees of freedom, this theory seems not to have much more fundamental explanatory power.

Another interesting point is that Λ has such a value that it becomes dominant around $z \approx 1$. An important effect of Λ is that it stops structure formation when it starts to dominate. Had Λ been larger, then galaxies would not have formed. It almost seems like the universe was fine tuned for life as we know it. This is often used to support the anthropic principle, but perhaps we can find a deeper understanding for this coincidence which may be related to the formation of structure itself.

At the same time, no single dark matter particle has been found in our detectors. But dark matter at least has a reasonable chance of being detected nearby, for example in our solar system (see Buist 2009). On the other hand, the cosmological constant seems to act only on cosmological scales, therefore making any local experiments impossible. This brings us to the uncomfortable conclusion that even though we know exactly where to look, and how much to expect, we do not have a single clue of the nature of the dark stuff in our universe. Perhaps we can find some alternatives?

1.5 Alternatives to dark energy

As indicated before, a fundamental physical explanation has not yet been found for dark energy. This has led a number of cosmologists to investigate the underlying assumptions for cosmology. The working base of cosmology is the Cosmological Principle, which is a cosmological version of the Copernican principle:

- the laws of physics are the same everywhere.
- the universe is perfectly homogeneous and isotropic on the largest scales,

The first part tells us we can apply the laws of physics everywhere, which seems a reasonable assumption. The second part tells that the universe looks the same everywhere for every observer. This also means that on the largest scales the universe becomes a smooth and homogeneous density field, and even weaker: perhaps only in a statistical sense. Therefore, often only homogeneous and isotropic densities are used in cosmological models. This was already done by Einstein in his first model, because solving the evolution of the universe otherwise becomes a tremendously non-linear problem.

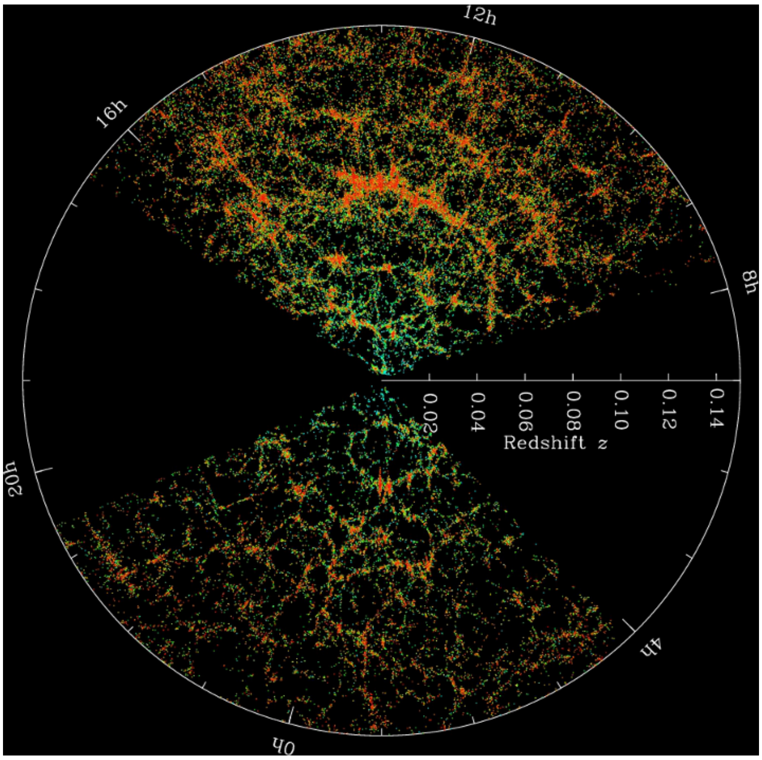

Figure 1.7: The Galaxy Distribution of the Sloan Digital Sky Survey (SDSS). In this image we see that the galaxies seem to cluster to a Cosmic Web, consisting of clusters, walls and voids. The maximum distance of this sample is approximately 480 Mpc h^{-1}. (Credit: M. Blanton and the Sloan Digital Sky Survey)

For the early universe this assumption seems valid, because the CMB showed that the primordial universe was almost perfectly isotropic and homogeneous. At later times structures form, such as stars, galaxies and clusters of galaxies, which together make an impressive pattern: the Cosmic Web (see figure 1.7). At least up to scales of 100 Mpc h^{-1} there is no homogeneity, and strong non-linear structures may develop. The structures we see above 100 Mpc h^{-1}, such as the Sloan Great Wall in the upper part, are still compatible with being a fluctuation of a homogeneous random distribution. Whether we really have reached the 'end of greatness' will only be known by performing larger and deeper surveys on the sky.

Given these very basic assumptions, several alternatives have been proposed to eliminate (part of) the need for dark energy. Notice that we do not really observe an acceleration of the expansion. What we do measure is a change in the luminosity-redshift relation. This means that valid alternatives should either result in an apparent acceleration, or try to modify the luminosity-redshift relation. The general direction of research can be summarized along three lines (Célérier 2007):

- special observers, particularly in a void;
- light propagation through a clumpy universe;
- average dynamics of the universe.

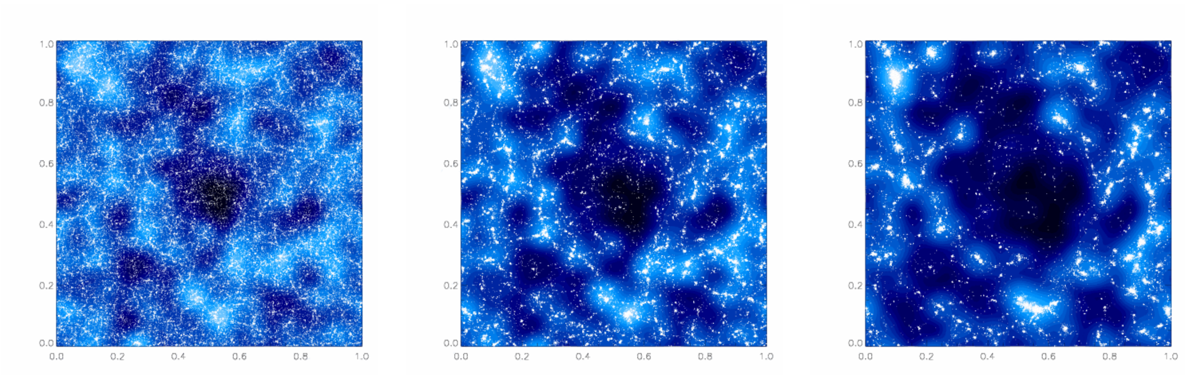

Figure 1.8: Expansion of a void in co-moving space from $a = 0.05$ to $a = 1$. These images were taken from an n-body simulation of a void by Erwin Platen (van de Weygaert & Platen 2009). As we see, the initial trough expands, while at the edge a ridge of structures are formed. As light moves inward, it experiences an ever increasing expansion, which causes a redshift of the light that increases with the distance of the source to the observer. An observer who assumes to live in a homogeneous universe could falsely interpret this effect as the accelerated expansion of space.

The special observer. This assumes we ourselves can be found near the centre of some gigantic void, with the supernovae outside of the void. The void should not really be empty, but they have a density that is about a half or a third of the average density in the universe. The idea is that the two groups of supernovae in the Hubble diagram would represent galaxies in the void and outside of the void respectively. The expansion rate becomes larger as one moves inward of the void, so that light that passes through gets redshifted. The more distant the source, the more redshifted the light gets. This might sufficiently adjust the distance scale, so that an observer that assumes an homogeneous universe observes an apparent acceleration (Clifton et al. 2008). In essence this idea questions the Copernican principle, because to match the redshift-luminosity relation the observer needs to be reasonably close to the centre of the void. In case the void is very large, then the CMB should also contain a signature of the void through the Sunyaev-Zel'dovich effect, which constrains the maximum size. The problem for this model is that the constraints are tightm making the special observer seem unlikely (Tomita 2009).

Light propagation through a clumpy universe. In this model it is assumed that clusters and voids together disturb the light as it is moving towards us. Such a model is often created by making a Swiss cheese: a group of spherical voids and overdensities are placed in a background space and the light propagation is computed. It seems that the effect is the same as obtained with weak lensing. The distribution of the voids and clumps is quite constrained, especially by the CMB, if any effect should be obtained towards an apparent acceleration (Clifton et al. 2009).

Average dynamics of the universe. Another more conservative point of view is to tweak our assumptions on cosmology. In cosmology we assume that the universe is homogeneous at the largest scales. Structures like our Milky Way are seen as only minor perturbations that do not influence the evolution of the cosmos. The result is that the cosmos evolves as a homogeneous fluid, without any feedback from the formation of structure. But on small scales, the universe is not homogeneous, and is only homogeneous in an average sense. In determining the evolution of the universe as a whole, we assume that we can take the average universe as the background. Thomas Buchert has explored the idea that pherhaps this implicit averaging could cause an apparent acceleration (Buchert & Ehlers 1997; Buchert 2000). His method relies on the spatial averaging of the scalar part of the Einstein equations, which is then rewritten in a form that reduces to the Friedmann equations for a strictly homogeneous model.

1.6 Overview

In this Groot Onderzoek project the goal was to investigate the magnitude of the cosmic backreaction as proposed by Thomas Buchert. For this the main tool would be to use spherical models, which can be straightforwardly evolved and used to extract observables related to backreaction. The focus is towards voids, in the hope that their larger than average acceleration might give significant backreaction. Eventually the models can be combined in a sort of Swiss-cheese hole model, in which a background universe is filled with spherical voids (that do not overlap) to simulate a portion of space.

The main questions for the project are therefore:

- **Is cosmic backreaction an alternative to dark energy?**
- How to integrate backreaction in the spherical model
- How to generate a universe filled with voids (i.e. Swiss cheese)
- Can we obtain backreaction using spherical voids in a background universe?

In the following chapters, we will first give a general overview of cosmology, learning methods that are useful later on when generating the initial conditions for the model. Then we continue to spherical models, in which spherical voids or blobs can be evolved in time to see how their mass distribution changes. These profiles need initial density profiles, for which we use Gaussian random fields. Having obtained the model and the initial conditions, we want to make a reasonable cheese. We took a cubic box and used the Sheth-van de Weygaert distribution of voids (Sheth & van de Weygaert 2004), which is used to model the sizes and the amount of voids in the model universe. The goal in this writing was to give a reasonably complete overview of the methods that we used and sometimes, the tricks that were learned or discovered.

2 Cosmology

At the large scales that we observe in our universe, the most important force is that of gravity. Comparing with the other three forces in nature it is by far the weakest, but it has an infinite range. Combined with the fact that one cannot shield gravity (unlike electromagnetic forces) makes gravity the dominant force in our universe. Currently, our best tool for describing the forces on the scale of the universe is Einstein's General Relativity (Einstein 1915). Originally, this theory was mainly directed at combining Special Relativity and gravity, but mostly in a local sense. It was soon realized that General Relativity could be used on our cosmos, even allowing us to speak of the universe as a whole. The discovery of the cosmological expansion and the link with the expanding solutions in General Relativity certainly boosted the interest in Relativistic Cosmology.

In the following paragraphs, we will walk through some of the theory involved in Relativistic Cosmology. We start with General Relativity, then we show how structure formation occurs in the linear regime and finally we will take a short look at certain aspects of non-linear structure formation.

2.1 General Relativity

One of the fundamental changes from Newtonian gravity to General Relativity is the introduction of space-time curvature. Whereas Newtonian gravity and Special Relativity assume flat space, General Relativity allows mass to curve space and time. It is exactly this curvature that sets particles in motion, but it is the particles that curve spacetime. These ideas are embodied in the Einstein field equations (Einstein 1915)

$$G^{\mu\nu} = \frac{8\pi G}{c^4} T^{\mu\nu} \ . \tag{2.1}$$

On the left hand side $G^{\mu\nu}$ is the Einstein tensor, which embodies the curvature of space-time. On the right-hand side $T^{\mu\nu}$ is the energy-momentum tensor, which contains terms relating to the matter in space-time. The proportionality factor $\frac{8\pi G}{c^4}$ was chosen in such a way that ordinary gravity emerges in the non-relativistic regime. The Einstein field equation looks very simple, but it is actually a majestic workhorse with 20 underlying differential equations and boundary conditions such as the continuity equation $\nabla_\kappa T^{\mu\nu} = 0$.

The curvature in the field equation is handled by the Einstein tensor, which itself is composed of the Ricci tensor and the Ricci scalar,

$$G^{\mu\nu} = R^{\mu\nu} - \frac{1}{2} g^{\mu\nu} R \ . \tag{2.2}$$

The Ricci tensor translates how the spacetime metric evolves and deviates from ordinary flat space. The Ricci scalar and tensor are itself contractions of the more general Riemann curvature tensor R^d_{adb}. On the right-hand side, finding the solution is often tried by using a solution close to Newtonian theory or Special Relativity. In the weak-field limit this can leads to self-consistent solutions, but in the strong-field this can no longer be done and a proper treatment of the equations of motion is required.

The cosmological principle provides a method to simplify solving the Einstein equation.

- The universe is isotropic and homogeneous at the largest scales,
- The laws of physics are the same everywhere.

The last of these is the required assumption that we can apply our locally known theories to the whole cosmos. The first part asserts that the universe is homogeneous and isotropic on large scales. Clumpiness on smaller scales averages out, so that a global behaviour of the cosmos can be obtained. We do not know if the principle holds exactly, as we currently see large structures up to sizes of 100 Mpc (such as the Sloan Great Wall) that are definitely not homogeneous. However, if the universe remains clumpy even on the largest scales, then cosmology becomes impossible because no global behaviour can be taken out.

In the Einstein field equations there is still room for one more component proportional to the metric $g^{\mu\nu}$. Einstein introduced this as the Cosmological Constant. It conserves energy, it is divergence free and therefore exactly this term is allowed [1]. The cosmological constant is constrained to be small, so that we cannot its effects on scales of a galaxy and smaller.

$$G^{\mu\nu} + g^{\mu\nu}\Lambda = \frac{8\pi G}{c^4} T^{\mu\nu} \ . \tag{2.3}$$

We have the freedom to place the constant either at the curvature or at the energy-momentum side. This is exactly the difference between the cosmological constant (part of the metric) and dark energy (dynamic).

$$T^{\mu\nu}_\Lambda = -\frac{\Lambda c^4}{8\pi G} g^{\mu\nu} \ . \tag{2.4}$$

[1] Newtonian theory also allows a cosmological constant, where it appears as a force $F(r) = \Lambda c^2 r$. This is the only force next to the $1/r^2$ law that satisfies that outside a spherical mass distribution, the force can be treated as if it were concentrated in point.

We will later see that this corresponds to a dynamic entity with a negative pressure, unlike anything we know from ordinary physics.

The result of solving the Einstein field equations will be the metric that describes spacetime. For cosmological purposes, this is exactly our goal. We could also look at light moving through space, which would involve solving the Geodesic equation,

$$\frac{d^2x^\lambda}{dt^2} + \Gamma^\lambda_{\mu\nu}\frac{dx^\mu}{dt}\frac{dx^\nu}{dt} = 0 \ , \tag{2.5}$$

where $\Gamma^\lambda_{\mu\nu}$ is the Christoffel symbol which embodies parallel transport on a curved spacetime. The geodesic equation describes how a free particle would move through the curved universe.

2.2 A cosmic metric

One very important class of solutions to the Einstein field equations are the Friedmann universes. They describe expanding isotropic and homogeneous spacetimes with flat, negative or postive global curvature. First discovered by Friedmann in the 1920s (Friedman 1922; Friedmann 1924), they were rediscovered and popularized by Lemaître (Lemaître 1927). The corresponding isotropic and homogeneous metric was discovered by Robertson and Walker (Robertson 1935; Walker 1935). Generally accepted today is then to refer to this as the Friedman-Lemaitre-Robertson-Walker metric (FLRW). The key ingredient to the FLRW metric is that space expands. This is brought in by seperating the position dependance in the comoving distance x and time dependence in the expansion factor a,

$$r(x,t) = a(t)x \ , \tag{2.6}$$

where we define $a(t_0) \equiv 1$ with t_0 today. This means that comoving and physical distance are equal today. The cosmological expansion is then given by the Hubble velocity, which we can rewrite as a Hubble law

$$v_H = \dot{a}(t)x = \frac{\dot{a}(t)}{a(t)}a(t)x = H(t)r(x,t) \ , \tag{2.7}$$

where the Hubble parameter is defined as $H(t) \equiv \dot{a}(t)/a(t)$, so that nearby we exactly find Hubble's law $v_H = H_0 r$ (with $H(t_0) \equiv H_0$). Using these coordinates, the FLRW metric becomes

$$ds^2 = -c^2dt^2 + a^2(t)\left(dx^2 + S_k(x)^2\left[d\theta^2 + \sin^2\theta d\phi^2\right]\right) \ , \tag{2.8}$$

with $k = +1, 0, -1$ corresponding to positive, zero or negative curvature of space (elliptic, flat or hyperbolic spaces respectively). The function $S_k(x)$ is given by

$$S_k(x) = \begin{cases} R_c \sin(\frac{x}{R_c}) & k > 0 \ , \\ r & k = 0 \ , \\ R_c \sinh(\frac{x}{R_c}) & k < 0 \ , \end{cases} \tag{2.9}$$

with R_c the radius of curvature at t_0. The FLRW-metric is not really found from the Einstein equations, but it is derived using the constraints of isotropy and homogeneity. The freedom of the expansion of space is determined by the energy-momentum tensor so that the Einstein equations are solved.

A related energy-momentum tensor also has to be isotropic and homogeneous. In the Friedmann models, we assume that the universe is filled with a perfect fluid, so effectively, we expect galaxies on a large scale to behave like particles of a fluid. The energy-momentum tensor is then given by

$$T^{\mu\nu} = \left(\rho + \frac{p}{c^2}\right) u^\mu u^\nu + g^{\mu\nu} p \tag{2.10}$$

with u^μ the four-velocity of a particle in the fluid and p the relativistic isotropic pressure. Looking at the term for Λ, we see that to fit in we need $p_\Lambda = -\rho_\Lambda c^2$ with $\rho_\Lambda = \frac{\Lambda c^2}{8\pi G}$. The conclusion is that the cosmological constant has a negative pressure, unlike normal matter which has approximately zero (relativistic!) pressure. For radiation like the CMB the pressure is given by $p_\gamma = \frac{1}{3}\rho_\gamma c^2$ with $\rho_\gamma c^2$ the photon energy density. Generally, we can include any component by summing to a total pressure and a total density, i.e. $\rho = \sum_i \rho_i$ and $p = \sum_i p_i$. If we then solve the Einstein field equations we will see how the universe evolves on the FLRW metric.

2.3 The Friedmann equations

The solutions to the perfect fluid on the FLRW metric consist of two equations, namely the energy equation and the acceleration equation

$$\begin{aligned} H^2 &= \frac{8\pi G}{3}\rho - \frac{kc^2}{R_c^2 a^2} \ , \\ \frac{\ddot{a}}{a} &= \frac{4\pi G}{3}\rho \ . \end{aligned} \tag{2.11}$$

These equations are also known as the Friedmann equations, relating the expansion of space to the density in space. From these, a third equation can be derived

$$\dot{\rho} = -3\frac{\dot{a}}{a}\left(\rho + \frac{p}{c^2}\right) \ . \tag{2.12}$$

which is also known as the continuity equation. These equations describe the evolution of a homogeneous, isotropic universe with density ρ and relativistic pressure p. The Gaussian curvature κ is not a free parameter, but it is instead fixed by the boundary conditions on the density $\rho(t_0)$ and the Hubble constant H_0. We can try to determine the curvature in a meaningful way by evaluating the energy equation at t_0,

$$\frac{kc^2}{R_c^2} = \frac{8\pi G}{3}\rho_0 - H_0^2 \ , \tag{2.13}$$

with $\rho_0 = \rho(t_0)$. The next step in rewriting the Friedmann equations is to use the continuity equation to find how the different density components evolve with time. To do this we use the relativistic pressure equations and solve for $\rho(a)$, resulting in the following evolutions

$$
\begin{aligned}
\rho_m(a) &= \rho_{m,0} a^{-3} \ , \\
\rho_\gamma(a) &= \rho_{\gamma,0} a^{-4}, \\
\rho_\Lambda(a) &= \rho_{\Lambda,0} \ .
\end{aligned}
\tag{2.14}
$$

In our universe, at very early times ($a \ll 1$) radiation will dominate the expansion, until at some moment matter takes over. This already happens before the moment of last scattering, so that radiation is almost never important when considering the post-recombination universe. As the universe expands, matter has a long phase of dominance, until it dilutes enough so that the cosmological constant Λ can take over. When that happens, the universe remains to expand and accelerate forever.

A useful step in describing the Friedmann equations is by introducing the unitless density parameter $\Omega = \rho/\rho_{cr}$, where ρ_{cr} is the critical density for which the universe is exactly flat,

$$
\rho_{cr} \equiv \frac{3H^2}{8\pi G} \Rightarrow 4\pi G \rho = \frac{3}{2}\Omega H^2 \ . \tag{2.15}
$$

We can use the critical density to rewrite the evolution of the different energy components of the universe,

$$
\begin{aligned}
H^2\Omega_m &= H_0^2\, \Omega_{m,0}\, a^{-3} \ , \\
H^2\Omega_\gamma &= H_0^2\, \Omega_{\gamma,0}\, a^{-4} \ , \\
H^2\Omega_\Lambda &= H_0^2\, \Omega_{\Lambda,0} \ , \\
\frac{kc^2}{R_c^2 a^2} &= H_0^2 \left(\Omega_{m,0} + \Omega_{\gamma,0} + \Omega_{\Lambda,0} - 1\right) \ .
\end{aligned}
\tag{2.16}
$$

If the universe is flat, the total density parameter $\Omega = 1$. Using all of the above equations in the Friedmann equations results in

$$
\begin{aligned}
H^2 &= H_0^2 \left(\frac{\Omega_{m,0}}{a^3} + \frac{\Omega_{\gamma,0}}{a^4} + \Omega_{\Lambda,0} + \frac{\Omega_{k,0}}{a^2} \right) \ , \\
\frac{\ddot{a}}{a} &= H_0^2 \left(-\frac{\Omega_{m,0}}{2a^3} + \Omega_{\Lambda,0} \right) \ .
\end{aligned}
\tag{2.17}
$$

In the next section we will try to discuss several solutions with Λ, matter and curvature, while ignoring radiation, as it is mainly important in the pre-CMB era (figure 2.1).

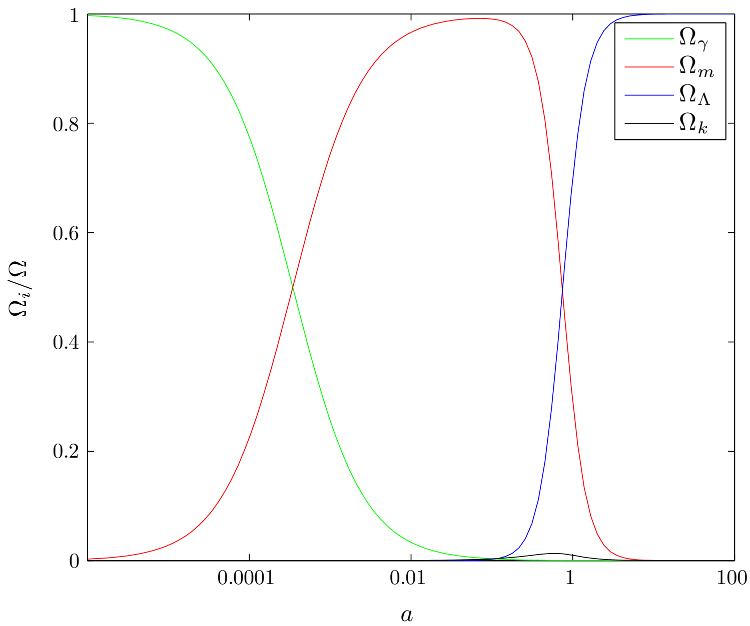

Figure 2.1: Importance of the different components of our universe over time. In the concordance model, radiation is only dominant before recombination at $a \approx 10^{-3}$. Matter quickly takes over and this goes on until near $a = 1$ the cosmological constant Λ takes over. Because space-time is flat to within 1%, the curvature is almost completely irrelevant. In this plot the curvature was exaggerated so that it would show up.

2.4 Categories of solutions

Before we solve the equations of motion we try to categorize the solutions. We first notice that both Friedmann equations can be integrated and solved to find the expansion of the universe. The acceleration equation is the derivative of the Hubble equation, so that the latter includes one extra integral of motion, namely the curvature. It turns out that analysis of the Hubble equation is enough to classify the solutions. Ignoring radiation, our next step is to recognize that we can separate a cubic polynomial in the Hubble equation

$$\frac{\dot{a}^2 a}{H_0^2} = \Omega_{\Lambda,0} a^3 + (1 - \Omega_{m,0} - \Omega_{\Lambda,0}) a + \Omega_{m,0} \ . \tag{2.18}$$

One can quickly realise that the roots in these equations are fundamental for the fate of the universe (see figure 2.2). When the universe reaches a point where the expansion rate $\dot{a}$ becomes zero, this indicates turnaround towards collapse ($\ddot{a} < 0$), a bounce ($\ddot{a} > 0$) or a loitering phase ($\ddot{a} = 0$). Universes without a real positive root therefore never reach a point of turn around, and expand forever.

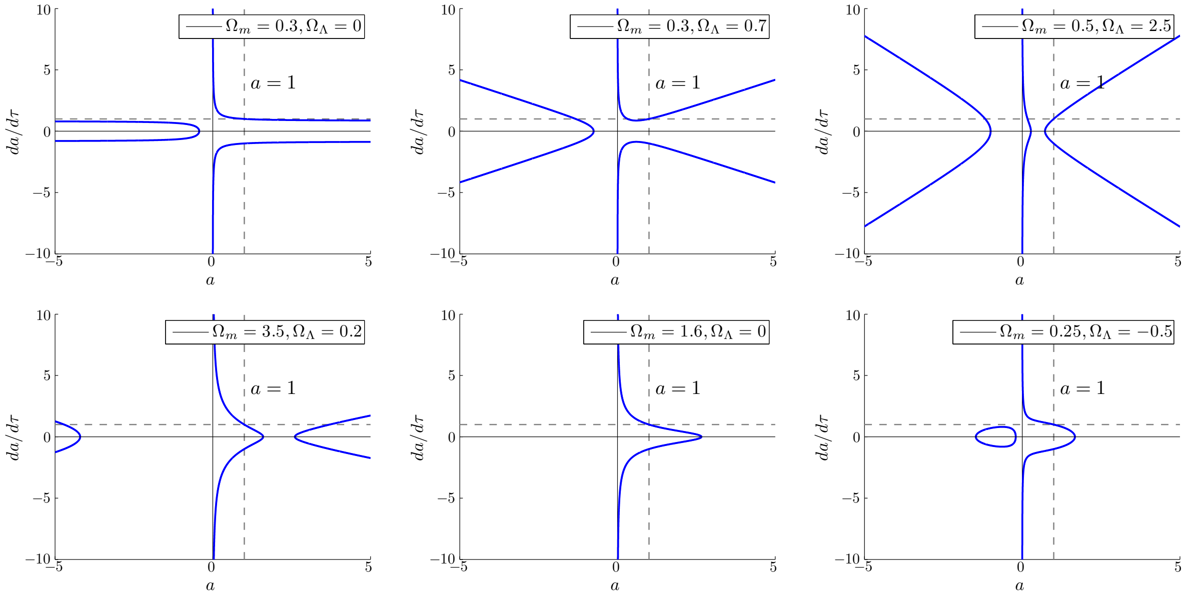

Figure 2.2: Phase diagrams ($da/d\tau$ vs a) plotted for several cosmological models. Top left: open matter only universe, which evolves towards an empty universe ($\dot{a}$ = cst, 1 negative root). Top, middle: ΛCDM universe, evolving towards a de Sitter universe ($\dot{a} = a$, one negative root, 2 complex roots). Top right: bouncing universe (2 positive roots and 1 negative root). Bottom left: collapsing universe, dominated by matter (2 positive roots and one negative root, as in the bouncing case). Bottom centre: closed matter only universe (one positive root). Bottom right: Λ dominated collapsing universe (in this case 1 positive and 2 negative roots, but sometimes 1 positive and 2 complex roots, see e.g. figure 2.3). These images show that positive roots are a key ingredient to determining the collapse of a universe.

For collapsing universes, expansion starts at $a = 0$ and moves towards the root. The (smallest) root should be at $a \geq 1$, because the solution has to reach $a = 1$ (boundary condition) while the expansion factor never reaches beyond the root. At the root, a phase of collapse is set in. For bouncing universes, the largest root should be at $a \leq 1$, because expansion comes from $a = \infty$ and moves towards a minimum below $a = 1$ and then moves back to infinity. Loitering universes are a special case, as they can have their root at any positive a. For a loitering universe, the matter and Λ content are such that the smallest and the largest positive root come together. It turns out that this exactly happens on the boundary between Λ-dominated expanding universes and bouncing or collapsing $\Lambda > 0$ universes.

So far we have only discussed the roots, but we can also just do the math. For cosmology we are lucky, because the polynomial (equation 2.18) is already in reduced form (i.e. without a square). In that case the discriminant D can be written down as

$$D = \left(\frac{p}{2}\right)^2 + \left(\frac{q}{3}\right)^3 \;\; ; \;\; p = \frac{\Omega_{m,0}}{\Omega_{\Lambda,0}} \;\; ; \;\; q = \frac{1 - \Omega_{m,0} - \Omega_{\Lambda,0}}{\Omega_{\Lambda,0}} \; . \tag{2.19}$$

For $D > 0$ we have 3 real roots, for $D < 0$ we have 1 real root and 2 complex conjugate roots, and for $D = 0$ all roots are real, while at least 2 roots are equal. For universes with only matter the discriminant is undefined, and the polynomial reduces to a linear equation (1 root). For Λ-only universes the polynomial reduces to a cubic equation (2 roots). In both cases the roots can be found relatively straightforward.

We really would like to know where in the parameter space of Ω_m and Ω_Λ we can find solutions with a positive root. This is not directly possible with the discriminant, but we can use it to separate regions with equal discriminant. We will see that these regions exactly match with the different solutions. The next step is therefore to see where the roots of the discriminant equation can be found. We find the following boundaries where $D = 0$,

$$
\begin{aligned}
\Omega_\Lambda^B &= \begin{cases} 4\Omega_m \left[\cosh\left(\frac{1}{3}\cosh^{-1}\left(\frac{1}{\Omega_m} - 1\right)\right)\right]^3 & \text{if } \Omega_\Lambda > 0,\ \Omega_m < 0.5\ , \\ 4\Omega_m \left[\cos\left(\frac{1}{3}\cos^{-1}\left(\frac{1}{\Omega_m} - 1\right)\right)\right]^3 & \text{if } \Omega_\Lambda > 0,\ \Omega_m \geq 0.5\ , \end{cases} \\
\Omega_\Lambda^C &= \quad 4\Omega_m \left[\cos\left(\frac{1}{3}\cos^{-1}\left(\frac{1}{\Omega_m} - 1\right) + \frac{4\pi}{3}\right)\right]^3 \qquad \text{if } \Omega_\Lambda > 0,\ \Omega_m > 1\ , \\
\Omega_\Lambda^D &= \begin{cases} 4\Omega_m \left[\cos\left(\frac{1}{3}\cos^{-1}\left(\frac{1}{\Omega_m} - 1\right) - \frac{4\pi}{3}\right)\right]^3 & \text{if } -0.25 < \Omega_\Lambda < 0,\ 0.5 \leq \Omega_m < 1\ , \\ 4\Omega_m \left[\cos\left(\frac{1}{3}\cos^{-1}\left(\frac{1}{\Omega_m} - 1\right) - \frac{4\pi}{3}\right)\right]^3 & \text{if } \Omega_\Lambda \leq -0.25,\ \Omega_m \geq 0.5\ . \end{cases}
\end{aligned}
\tag{2.20}
$$

These boundaries are shown in figure 2.3. Ω_Λ^C is the boundary of the collapsing region with $\Omega_\Lambda > 0$, Ω_Λ^B represents the boundary with the Big Bounce region and Ω_Λ^D represents the bottom curve in the collapsing region, where it only marks a mathematical difference in the set of collapsing solutions. It turns out that these boundary lines for $\Omega_\Lambda > 0$ represent loitering universes (see also Peacock 1999; Percival 2005).

A table with an overview of all classes of universes can be found in the index, with their corresponding roots and solutions. The most relevant of these universes are those for which $\Omega \geq 0$ and $\Omega_m \approx 0 - 2$. Observations seem to rule out the loitering, bouncing and collapsing universes. These findings will become important later on, as we will see that spherical perturbations in space behave like mini-universes, and their fate is equally well determined using the fate diagram.

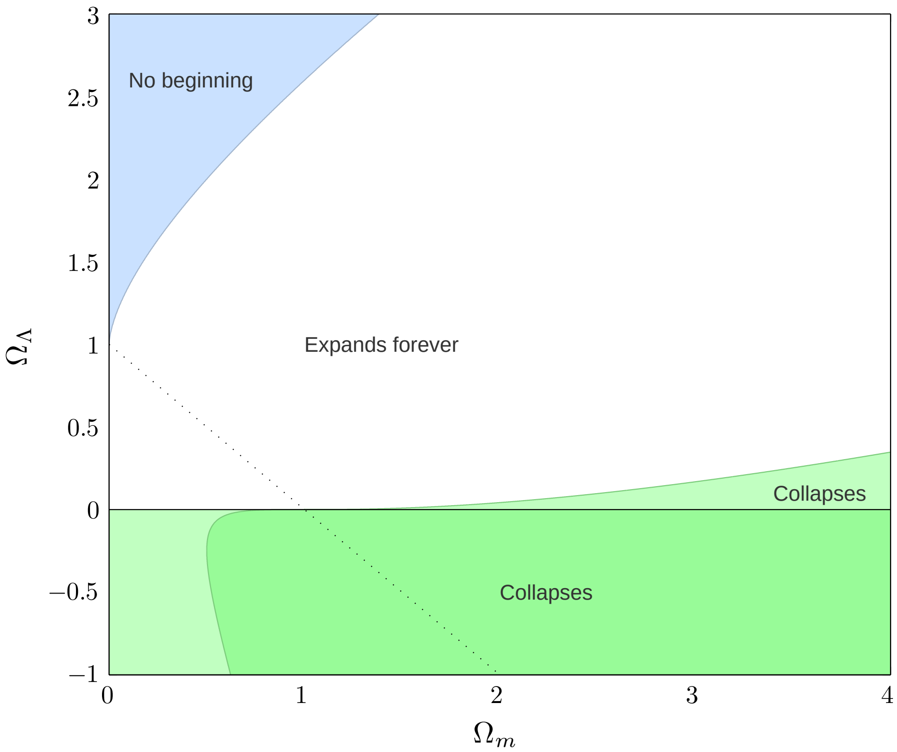

Figure 2.3: Fate diagram for Ω_m and Ω_Λ. The boundary curves are those where the discriminant of the Hubble equation vanishes. The black dashed line shows flat universes ($\Omega_m + \Omega_\Lambda = 1$. When a universe starts in any of these 'sectors' (including the separation by the flatness line), it can never reach another sector as it evolves. The same holds for the horizontal axis, where $\Lambda = 0$ and remains so, except for the Einstein-de Sitter universe at $\Omega_m = 1$ which is the start for many Λ universes. This also holds for the de Sitter universe ($\Omega_\Lambda = 1$, $\Omega_m = 0$ which is the other 'attractor' of Λ universes. These interpretations can all be found by using the phase diagrams like figure 2.2. A more general set of diagrams for dark energies can be found in Percival 2005

2.5 Solutions

We have come to understand a lot about the universes without even solving the equations of motion. But we would also like to see how the expansion factor evolves in time. In some cases the time evolution of the Friedmann universes can be solved analytically, while in some other cases they can only be solved using a numerical analysis. One way of solving the equations of motion is by integrating $\dot{a}$ to find t

$$H_0 (t_2 - t_1) = \int_{a_1}^{a_2} \frac{dt}{da} da = \int_{a_1}^{a_2} \frac{a\,da}{\sqrt{\Omega_{m,0}a + \Omega_{\Lambda,0}a^4 + \Omega_{k,0}a^2}} \,. \tag{2.21}$$

This method is quickly set up, but can cause problems for closed universes, as they will have a root at their maximum expansion factor $a = a_{max}$. Another solution is to rewrite the equations of motion into an ordinary differential equation (i.e. $\frac{d\vec{y}}{dt} = \vec{F}(\vec{y}, t)$),

$$\frac{d\vec{y(t)}}{dt} = \frac{d}{dt}\begin{pmatrix} a(t) \\ \dot{a}(t) \end{pmatrix} = \vec{F}(\vec{y}, t) = \begin{pmatrix} \dot{a}(t) \\ H_0^2\left(-\frac{\Omega_{m,0}}{2a(t)^3} + \Omega_{\Lambda,0}\right) \end{pmatrix} . \tag{2.22}$$

The boundary conditions make sure that the curvature is still there. A very useful method to obtain soltions is by moving from time t to Hubble time $\tau = H_0 t$. This makes the initial condition for $\dot{a}(t_0) = 1$, so that the actual solution does not directly depend on the value of H_0. A number of the solutions is solvable in direct analytic form. The first universe we show is the de Sitter universe ($\Omega_\Lambda = 1$, $\Omega_m = 0$), which is the limiting case for a general Λ expanding universe

$$\begin{aligned} a(t) &= \exp\left(H_0(t - t_0)\right) \ , \\ H_0 = H(t) &= \frac{\Lambda}{3} \ . \end{aligned} \tag{2.23}$$

The start for many universes is close to the Einstein-de Sitter universe ($\Omega_\Lambda = 0$, $\Omega_m = 1$), as we can see from figure 2.1. Starting from the big bang at $t = 0$, the solution becomes

$$\begin{aligned} a(t) &= \left(\frac{t}{t_0}\right)^{2/3} \ , \\ t_0 &= \frac{2}{3H_0} \ . \end{aligned} \tag{2.24}$$

For a long time, astronomers thought our universe would be such a universe, until observations pointed out that the universe was not even near $\Omega = 1$ and accelerating. In the case that $\Lambda = 0$ but $\Omega_m \neq 1$ we have two other classes of analytical solutions, the open matter-only model and the closed matter-only model. These solutions have the unique property that the open universe has always negative space curvature, while the closed universe has always positive curvature. The solution for the open matter-only model ($0 < \Omega_m < 1$, $\Omega_\Lambda = 0$) is given by (van de Weygaert 1995; Lahav & Suto 2004)

$$\begin{aligned} a(\eta) &= \frac{\Omega_m}{2(1-\Omega_m)}(\cosh\eta - 1) \ , \\ H_0 t(\eta) &= \frac{\Omega_m}{2(1-\Omega_m)^{3/2}}(\sinh\eta - \eta) \ , \\ H_0 t_0 &= \frac{1}{1-\Omega_m} - \frac{\Omega_m}{2(1-\Omega_m)^{3/2}}\cosh^{-1}\left(\frac{2}{\Omega_m} - 1\right) \ , \end{aligned} \tag{2.25}$$

with $\eta \in [0, \infty)$ a parametrization angle as there is no direct formula for $a(t)$. For the closed matter-only model ($\Omega_m > 1$, $\Omega_\Lambda = 0$) we find

$$\begin{aligned} a(\eta) &= \frac{\Omega_m}{2(\Omega_m - 1)}(1 - \cos\eta) \; , \\ H_0 t(\eta) &= \frac{\Omega_m}{2(\Omega_m - 1)^{3/2}}(\eta - \sin\eta) \; , \\ H_0 t_0 &= \frac{1}{1 - \Omega_m} + \frac{\Omega_m}{2(\Omega_m - 1)^{3/2}} \cos^{-1}\left(\frac{2}{\Omega_m} - 1\right) \; . \end{aligned} \tag{2.26}$$

with $\eta \in [0, 2\pi]$. The similarity between these two classes of universes is strong as they both show a side of the same $\Lambda = 0$ coin. There is also one special class of $\Lambda > 0$ universes with $\Omega_m < 1$ that are exactly flat ($\Omega_\Lambda = 1 - \Omega_m$). The observations show that our universe is close to this model (Komatsu et al. 2011). The solution is given by

$$\begin{aligned} a(t) &= \left(\frac{\Omega_m}{1 - \Omega_m}\right)^{1/3} \left[\sinh\left(\frac{3\sqrt{1 - \Omega_m}}{2} H_0 t\right)\right]^{2/3} \; , \\ H_0 t_0 &= \frac{2}{3\sqrt{1 - \Omega_m}} \sinh^{-1} \sqrt{\frac{1 - \Omega_m}{\Omega_m}} \; . \end{aligned} \tag{2.27}$$

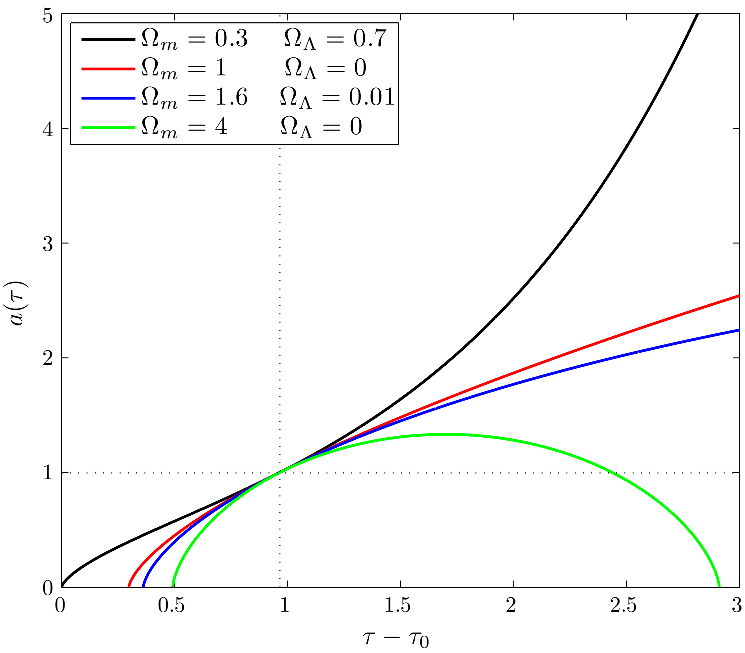

Figure 2.4: Time evolution of several cosmologies, normalised to today with $\tau = H_0 t$. Important are the age of the universe and the acceleration of the expansion. The ΛCDM universe (black) stands out because it is generally much older and accelerates towards exponential expansion.

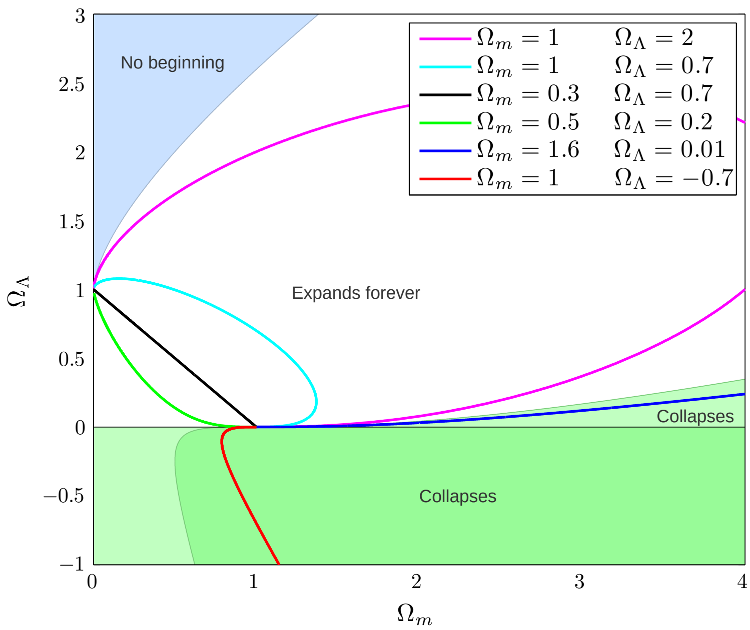

Figure 2.5: Fate diagram for several cosmological models with Λ and matter. All universes with matter and dark energy, that are not in the upper-left blue region (big bounce) start at $\Omega_m = 1$, $\Omega_\Lambda = 0$. The white region corresponds with forever expanding universes, in which Λ eventually takes over, so that they end up as a de Sitter universe ($\Omega_m = 0$, $\Omega_\Lambda = 1$). The green regions correspond to collapsing regions, where the upper triangle shows the part where matter still wins from the cosmological constant. For negative Λ, the universe always collapses. Closed universes evolve to $\Omega_m = \infty$, at which point they turn around ($H = 0$), and then return along the same path to the starting point. Universes without Λ are located along the x-axis, while universes without matter are located on the y-axis. Open matter-only universes do not become de Sitter universes, but eventually end up as empty universes ($\Omega_m = 0$, $\Omega_\Lambda = 0$). The Einstein-de Sitter ($\Omega_m = 1$, $\Omega_\Lambda = 0$) and the de Sitter universes ($\Omega_m = 0$, $\Omega_\Lambda = 1$) are the only universes that do not evolve in this diagram, as they are the begin/end point for many universes.

Figure 2.4 shows the result for the evolution of several universes using the ordinary differential equation approach. This can also be coupled to the fate diagram as shown in figure 2.5.

We have seen how to compute the evolution of the universe and to determine how it will evolve. Some of the properties of the models that we discussed here will later on be useful in understanding the models for spherical perturbations. In the next chapter we continue with cosmology by adding linear perturbations to the smooth universes that we computed here.

3 Structure in the universe

So far we have only looked at the universe as a homogeneous matter distribution. This is thought to be a valid picture at the very largest scales in our universe, but we know that on smaller scales this is not the case, otherwise we would not be here. On small scales, a homogeneous universe would also be unstable, as even the slightest perturbation would within reasonable time grow to a much larger mass. This is what happened with the early universe, which was nearly homogeneous, but accompanied with tiny density and velocity perturbations.

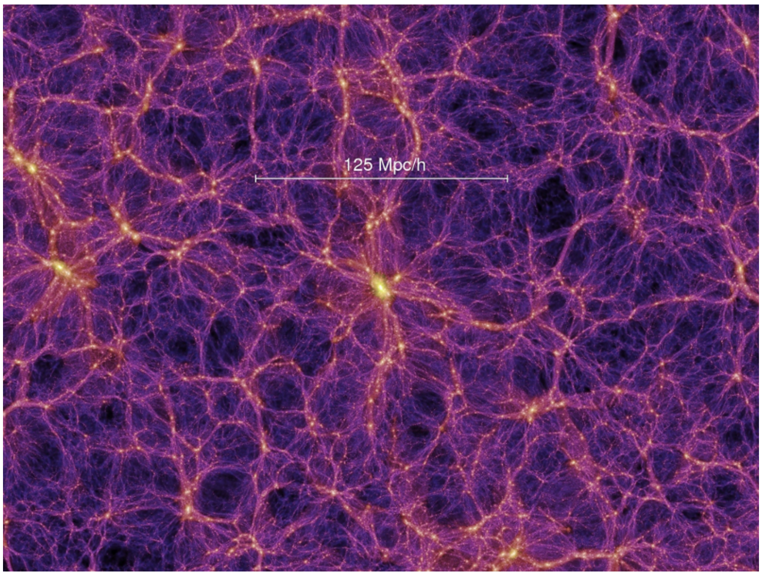

Figure 3.1: Image of a cluster in the Millennium simulation. The Millennium simulation is a simulation of the large scale structure of the universe. The goal was to provide a simulation that could be compared with the real structure in the universe. The simulation used 2160^3 particles in a cubic region of size 500 h^{-1} Mpc (Springel et al. 2005). This specific image shows a cluster in the simulation, surrounded by voids and walls.

The fluctuations that we can observe from the CMB ($\approx 10^{-5}$) are in fact relics of the early matter perturbations, as radiation and matter at that time were still intimately connected. Using gravitational instability, we can try to understand how structure formed from these tiny perturbations. The idea is as follows. As time goes on, small overdensities exert a gravitational attraction to their neighbours, which makes them slow down from the Hubble expansion. Eventually the neighbouring particles decouple from the Hubble flow and fall towards the overdensities. At some point, these objects form stars, galaxies or clusters, depending on the size of the perturbations. Underdensities see a different process, in which more and more matter is attracted to nearby overdensities, which results in a growing void with a overdense wall around it. The centre of the void behaves like an empty universe with a super-Hubble expansion. The walls on the other hand collapse to an outward moving ridge around the void. The resulting global behaviour would be that of a cosmic web, where galaxies act as particles in a cosmic fluid (see figure 3.1).

3.1 Gravitational instability

If we take the global behaviour of structures in our universe as a fluid, then we can use the fluid equations. We can limit ourselves to using Newtonian fluid equations for the matter perturbations, because Dark Energy as a cosmological constant does not form structure, while radiation is not relevant either. The Newtonian fluid equations are given by (Lahav & Suto 2004; Peebles 1980)

$$\begin{gathered}\frac{\partial \rho}{\partial t} + \nabla \cdot (\rho \vec{u}) = 0 \ , \\ \frac{\partial \vec{u}}{\partial t} + (\vec{u} \cdot \vec{\nabla})\vec{u} = -\frac{1}{\rho}\vec{\nabla}p - \vec{\nabla}\Phi \\ \nabla^2 \Phi = 4\pi G \rho \ , \end{gathered} \tag{3.1}$$

respectively the continuity equation, the Euler equation (force equation) and the Poisson equation. In its most convenient form, we can try to rewrite these equations in peculiar and comoving entities, using the comoving radius $\vec{x} = \vec{r}/a(t)$, the peculiar velocity $\vec{v} = a(t)\dot{\vec{x}}$, the density fluctuation $\delta(\vec{x}, t) = \rho(\vec{x}, t)/\rho_u(t) - 1$ and the peculiar potential $\phi = \Phi + \frac{1}{2}a\ddot{a}x^2$ (and use $\nabla_r = \frac{1}{a}\nabla_x$). The fluid equations then reduce to

$$\begin{gathered}\frac{\partial \delta}{\partial t} + \frac{1}{a}\nabla \cdot (1+\delta)\vec{v} = 0 \ , \\ \frac{\partial \vec{v}}{\partial t} + \frac{1}{a}(\vec{v} \cdot \vec{\nabla})\vec{v} + \frac{\dot{a}}{a}\vec{v} = -\frac{1}{\rho a}\vec{\nabla}p - \frac{1}{a}\vec{\nabla}\phi \\ \nabla^2 \phi = 4\pi G \rho a^2 \delta \ . \end{gathered} \tag{3.2}$$

In this section we will only look at the evolution of structure in the linear phase. This means that the resulting overdensities $\delta \ll 1$ and the velocities $v \ll \frac{ct}{d}$ with t_{exp} the expansion time-scale and d the length scale of interest. At the current moment, the linear approximation seems to be valid at scales above 10 Mpc h^{-1}, making this a good starting point for the description of the Large Scale Structure of the universe. At the same time also ignoring the (relativistic) pressure of matter in the universe we can approximate the above equations by (van de Weygaert 2005)

$$\begin{aligned} \frac{\partial \delta}{\partial t} + \frac{1}{a}\nabla \cdot \vec{v} = 0 \ , \\ \frac{\partial \vec{v}}{\partial t} + \frac{\dot{a}}{a}\vec{v} = -\frac{1}{a}\vec{\nabla}\phi \\ \nabla^2\phi = 4\pi G\rho a^2\delta \ . \end{aligned} \tag{3.3}$$

If we then take the divergence of the Euler equation and replace the terms with $\nabla^2\phi$ with the poisson equation and the terms with $\vec{\nabla} \cdot \vec{v}$ with the continuity equation, then we find the differential equation for linear structure growth

$$\frac{\partial^2 \delta}{\partial t^2} + 2\frac{\dot{a}}{a}\frac{\partial \delta}{\partial t} = 4\pi G\delta\rho_{m,0}\, a^{-3} \ . \tag{3.4}$$

This differential equation has only terms with time derivatives, and no spatial derivatives. This means we can seperate the spatial behaviour from the time behaviour with $\delta(\vec{x}, t) = D(t)\Delta(x)$

$$\ddot{D} + 2H\dot{D} = 4\pi G D\rho_m \ . \tag{3.5}$$

On the other hand, we have a second order differential equation. This allows for two solutions, so that the total evolution of δ is given by

$$\delta(\vec{x}, t) = D_1(t)\Delta_1(\vec{x}) + D_2(t)\Delta_2(\vec{x}) \ . \tag{3.6}$$

We see that evolution of perturbations in linear theory will be everywhere the same (i.e. self-similar). Also, perturbations with $\delta < -1$ can exist, as the model does not distinguish between over- and underdensities. This is not a real problem as most of the time linear growth is only applied in the early universe or on large scales, where $\delta \ll 1$. The growth itself strongly depends on the background cosmology through the 'Hubble drag' term ($2H\dot{D}$), and the density term with a^{-3}. The two solutions that can be found turn out to be a growing and a decaying solution, whereby the decaying mode is generally neglected as it should have disappeared already. The general equation for structure growth then becomes

$$\delta(\vec{x}, t_2) = \frac{D(t_2)}{D(t_1)}\delta(\vec{x}, t_1) \ , \tag{3.7}$$

with $D(t)$ now only the growing mode solution.

In the $\Lambda = 0$ case, structure growth can be solved analytically, resulting in the following expressions (Peebles 1980; van de Weygaert 2005)

$$\begin{aligned}
\Omega_m < 1 \quad & D(t) = \frac{3\sinh\eta\,(\sinh\eta - \eta)}{(\cosh\eta - 1)^2} - 2 \ , \\
\Omega_m = 1 \quad & D(t) = a(t) \ , \\
\Omega_m > 1 \quad & D(t) = \frac{3\sin\eta\,(\eta - \sin\eta)}{(\cos\eta - 1)^2} - 2 \ ,
\end{aligned} \tag{3.8}$$

with η the development angle that we saw before for these models. The linear growth for the closed $\Omega_m > 1$ universe reaches infinity at when the universe collapses again ($\eta = 2\pi$). This makes sense because in a collapsing universe, the Hubble drag reverses sign so that it helps creating structure.

The equations of linear growth will later prove to be important, because we can use it to generate initial conditions for our initial model. Most often, we use methods which are normalised to today, but using linear growth, we can for example put a density profile at $z = 1000$. However, the method using the differential equations is not very convenient when used in models, except for finding exact solutions. An alternative is an integral expression, which provides a much more direct approach to the linear growth factor. The first step is to recognize that we can put the Friedmann equations in a similar form as equation 3.5

$$\ddot{H} + 2H\dot{H} = 4\pi G H \rho_m \ . \tag{3.9}$$

Combining both differential equations by carefully multiplying with $H(t)$ and $D(t)$ we can get the following second order differential equation

$$\frac{d}{dt}\left\{a^2 H^2 \frac{d}{dt}\left(\frac{D}{H}\right)\right\} = 0 \ . \tag{3.10}$$

This equation can be integrated to give (Peebles 1980; Heath 1977)

$$D(t) = c_1 H(t)\left(\int_0^t \frac{dt}{\dot{a}^2} + c_2\right) = c_1 H(t)\left(\int_0^{a(t)} \frac{da}{\dot{a}^3} + c_2\right) \ , \tag{3.11}$$

where c_1 represents an arbitrary normalisation of the growth factor, while c_2 represents the presence of the decaying mode. Often c_1 is chosen such that at early times, $D(t) \approx a(t)$, which requires that $c_1 = \frac{5}{2}\Omega_{m,0}H_0^2$ (van de Weygaert 2005). What we can also understand from the integrated growth equation is that the decaying mode is proportional to the Hubble parameter (see figure 3.2 for an example of the Growth factor for several cosmologies).

The integrals for the growth factors of closed universes have a few interesting issues. First of all, this formula mirrors the growing mode around the moment of turn-around which results in an discontinuous break in the result. The mirroring appears because $\dot{a}(a)$ returns

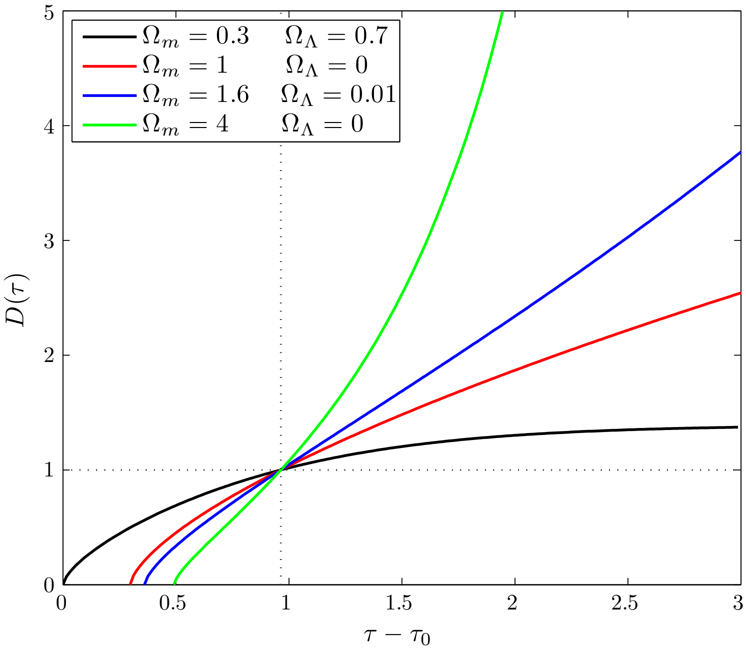

Figure 3.2: Linear growth factors for several cosmologies. The blue and green line represent closed cosmologies, and we see that they have much stronger structure growth. For the ΛCDM universe (black), structure growth comes to a halt, which happens at the moment that the universe transitions to exponential de Sitter expansion.

back to zero. We have already found the exact solution for $\Omega_m > 1$, $\Omega_\Lambda = 0$, which shows that the growth moves on and then diverges the moment where the universe collapses. It turns out that the key ingredient is to add a certain amount of the decaying mode solution to get the full growing mode solution. This is allowed because it is merely an integration constant. Notice also that the decaying mode in fact starts to join the growing mode when in the collapsing phase, as the Hubble parameter reverses sign.

We can try to find the constant c_2 after turnaround that makes the growth factor evolve continuously in a closed universe. We first recognize that because $H = 0$ at the point of turn around, the solution always connects, but not necessarily continuously. To solve this we demand that the first derivative before and after turnaround should be equal. Suppose we approach the integral from both sides towards the critical point. Below the turnaround point, the integral increases ($\dot{D}^+ > 0$), while after turnaround the integral decreases ($\dot{D}^- < 0$), so that $\dot{D}^+_{\text{turn}} = -\dot{D}^-_{\text{turn}}$. We then get the following continuity result

$$\dot{D}^+_{\text{turn}} = -\dot{D}^-_{\text{turn}} + c_2 \dot{H}_{\text{turn}} \Rightarrow \; 2\dot{D}^+_{\text{turn}} = c_2 \left[\frac{\ddot{a}}{a} - H^2\right]_{\text{turn}} = c\frac{\ddot{a}}{a} \; . \tag{3.12}$$

The constant c_2 is then given by

$$c_2 = \frac{2\dot{D}^+_{\text{turn}}}{\ddot{a}/a} \; . \tag{3.13}$$

Another issue with closed universes is that the integral term diverges when numerically integrated. The integrand $\dot{a}$ has a root in the integration interval, while the growth factor as a whole does not diverge because it is multiplied with $H(t)$, which has a zero point at the root. A solution to this problem is to take out the root from the Hubble parameter and move it under the integral. In the expansion rate, we can separate the root $a_{\max}$ as follows

$$\dot{a}^2 = \frac{H_0^2 \Omega_{\Lambda,0}}{a}(a - a_{\max})(a - a_2)(a - a_3) \ , \tag{3.14}$$

with a_2 and a_3 representing the other roots of the expansion rate. The integral then becomes

$$D \propto H(a) \int_0^a \frac{dx}{\dot{a}(x)^3} = \int_0^a dx \frac{(a - a_{\max})^{1/2}}{(x - a_{\max})^{3/2}} f(x) \propto \sqrt{\frac{a - a_{\max}}{a - a_{\max}}} f(p) \ , \tag{3.15}$$

with $f(a)$ a smoothly evolving function that absorbs the other roots (but that does not have any roots in the integration interval). The last step with p a point somewhere in the interval is valid because $f(a)$ has no roots in the interval. We see that the integral should not diverge. To ensure this numerically, we introduce a change of coordinates

$$d\eta = \frac{1}{2} \frac{(a - a_{\max})^{1/2}}{(x - a_{\max})^{3/2}} dx \tag{3.16}$$

so that we have

$$\eta(x) = \sqrt{\frac{a - a_{\max}}{x - a_{\max}}} \ , \qquad x(\eta) = \frac{a - a_{\max}}{\eta^2} + a_{\max} \ . \tag{3.17}$$

This means that the total integral then becomes

$$D(a) = \frac{2}{\Omega_{\Lambda,0} a^{3/2}} \int_{\eta(0)}^{\eta(a)} \frac{\sqrt{a - r_2}\sqrt{a - r_3}}{(x - r_2)^{3/2}(x - r_3)^{3/2}} x(\eta)^{3/2} d\eta \ . \tag{3.18}$$

The same approach can be used for matter only universes, but then only a single root appears in the integration interval. We now have reached a full description of how structure grows in the linear theory. In the next paragraph, we will see how we can use this to find peculiar velocities. This in turn can be used for the initial conditions of a universe.

3.2 Peculiar velocity field

An interesting question is whether vorticity, the rotation of a fluid, can occur in the linear regime. We can investigate this by separating the peculiar velocity flow in a potential flow and a rotational flow

$$\vec{v} = \vec{v}_{\parallel} + \vec{v}_{\perp} \ , \tag{3.19}$$

where the rotational flow can be found from $\vec{\nabla} \cdot \vec{v}_{\perp} = 0$ and the potential flow from $\vec{\nabla} \times \vec{v}_{\parallel} = 0$. From the linearised fluid equations we can then infer that only the gradient flow $\vec{v}_{\parallel}$ couples to the growth of the density perturbations, while the vorticity flow $\vec{v}_{\perp}$ is wiped out by the expansion

$$\begin{aligned} \vec{\nabla} \cdot \vec{v}_{\parallel} &= -a \frac{\partial \delta}{\partial t} \ , \\ \frac{\partial \vec{v}_{\perp}}{\partial t} &= -\frac{\dot{a}}{a} \vec{v}_{\perp} \ . \end{aligned} \tag{3.20}$$

The conclusion is that in the linear regime, the peculiar velocities are only potential flows ($\vec{v} = \vec{v}_{\parallel}$). We can also try to find the source of these motions and see how they evolve. Combining the first of these equations with the Poisson equation, replacing $\vec{g} = -\frac{1}{a}\vec{\nabla}\phi$ and reworking a bit then results in

$$\vec{v} = a \frac{\partial}{\partial t} \left(\frac{\vec{g}}{4\pi G \rho_m a} \right) \ . \tag{3.21}$$

We find that the source of the peculiar velocity field is the exactly the peculiar gravitational field $\vec{g}$. To find the evolution of the peculiar velocity we will need to find how the the peculiar gravity evolves. This can be done by solving the Poisson equation for the peculiar potential ϕ

$$\frac{1}{a^2} \nabla^2 \phi = 4\pi G \rho_u \delta \ . \tag{3.22}$$

The full solution to the peculiar acceleration then becomes (Peebles 1980)

$$\vec{g}(\vec{x}, t) = -\frac{\vec{\nabla}\phi}{a} = G a(t) \rho_u(t) \int d^3x' \, \delta(\vec{x}, t) \, \frac{\vec{x}\,' - \vec{x}}{|\vec{x}\,' - \vec{x}|^3} \ \propto D(t) a(t) \rho_u(t), \tag{3.23}$$

where the last term shows the linear evolution (with the substitution $\delta \propto D$). Using this in the above relation for the peculiar velocity and reworking using the expansion factor a we find

$$\vec{v} = \frac{Hf}{4\pi G \rho_m} \, \vec{g} = \frac{2f}{3H\Omega_m} \, \vec{g} \ , \tag{3.24}$$

with $f = d\ln D/d\ln a$ the linear velocity grow factor. A commonly used approximation for the matter-only case was found by Peebles as $f(\Omega_m) \approx \Omega_m^{0.6}$, while for matter and dark energy an approximation was found by Lahav et al. 1991 as

$$f(\Omega_m, \Omega_\Lambda) \approx \Omega_m^{0.6} + \frac{\Omega_\Lambda}{70} \left(1 + \frac{\Omega_m}{2} \right) \ . \tag{3.25}$$

Matter clearly dominates the evolution of f, but for the peculiar velocity field we should not forget that H also depends on Ω_Λ. We will see later on use these expressions to generate initial peculiar velocities for spherical models with given values of δ. Most often these start just after recombination at $z \approx 1000$, so that they are reasonably valid at the time.

3.3 Adding shear and vorticity

So far the perturbations in the fluid evolved self-similarly, without rotation or deformation. We can add one extra degree of complexity to the formation of structure, by making the velocity field a true vector field, with the possibility of shear and vorticity. Shear can cause the formation of pancakes from spherical structures, while vorticity indicates the rotation in the cosmic fluid. As before, we would like to extract Hubble-like quantities, but now for a 3-dimensional vector field. We also move towards Lagrangian coordinates, in which we fix a volume element and look how it expands or contracts, unlike the Eulerian view we took in the previous chapter. The first step is to look at the Hubble flow tensor (van de Weygaert 2005)

$$H_{ij} \equiv \frac{\partial u_i}{\partial r_j} = \frac{1}{3}\theta\delta^K_{ij} + \sigma_{ij} + \omega_{ij} \ , \tag{3.26}$$

with θ the expansion (the trace of H_{ij}), σ_{ij} the shear, which is the traceless symmetric part, and ω_{ij} the vorticity, which is the antisymmetric part of the flow. Here δ^K_{ij} is the Kronecker delta function and the indices on r_j indicate the three principal axes x, y, z. We can write these velocity objects down as

$$\theta = \frac{\partial u_i}{\partial r_i} = \vec{\nabla} \cdot \vec{u} \ , \tag{3.27}$$

$$\sigma_{ij} = \frac{1}{2}\left(\frac{\partial u_i}{\partial r_j} + \frac{\partial u_j}{\partial r_i}\right) - \frac{1}{3}\theta\delta^K_{ij} \ , \tag{3.28}$$

$$\omega_{ij} = \frac{1}{2}\left(\frac{\partial u_i}{\partial r_j} - \frac{\partial u_j}{\partial r_i}\right) \ . \tag{3.29}$$

A quick inspection learns that for a pure Hubble flow, the shear and vorticity are zero, while $\theta_H = 3H(t)$. Using these equations, we can try to generalise the Euler equation to a tensor equation as (Peebles 1980)

$$\frac{dH_{ij}}{dt} + H_{ik}H_{kj} = \frac{\partial^2\Phi}{\partial r_i \partial r_j} - \frac{\partial}{\partial r_j}\left(\frac{1}{\rho}\frac{\partial p}{\partial r_i}\right) \ . \tag{3.30}$$

We can take the seperate parts of these equations out to find the evolution of the vorticity, shear and expansion. For the matter dominated case, we can again ignore radiation, so that the trace of this equation gives the acceleration or Raychoudhury equation (Raychaudhuri 1955)

$$\frac{d\theta}{dt} + \frac{1}{3}\theta^2 = \omega^2 - \sigma^2 - \nabla^2\Phi \ , \tag{3.31}$$

with $\sigma^2 = \sigma_{ij}\sigma_{ij}$ and $\omega^2 = \omega_{ij}\omega_{ij}$. We see that the shear acts towards compression of the volume element, while the vorticity causes the volume element to expand. The result is that shear speeds up the collapse of structure, while vorticity tends to slow it down. To make this more obvious, we can also combine the Raychaudhury equation with the previous part on linear structure growth. Assuming small perturbations and ignoring vorticity we can get a modified equation for linear growth (van de Weygaert (2005))

$$\frac{\partial^2 \delta}{\partial t^2} + 2\frac{\dot{a}}{a}\frac{\partial \delta}{\partial t} = \frac{2}{3}\Sigma^2 + 4\pi G \delta \rho_{m,0}\, a^{-3} \ , \tag{3.32}$$

with Σ_{ij} the shear tensor for the peculiar velocities v. We see again confirmed that the shear causes the collapse to proceed more quickly. The Raychaudhury equation is not enough to close the fluid equations. We still have the conservation of mass, which in the Lagrangian formalism it becomes

$$\frac{d\rho}{dt} = -\rho\theta \ . \tag{3.33}$$

The antisymmetric part results in the equations describing the evolution of vorticity ω_{ij},

$$\frac{d\omega_{ij}}{dt} + \frac{2}{3}\theta\omega_{ij} + \sigma_{ik}\omega_{kj} + \omega_{ik}\omega_{kj} = 0 \ . \tag{3.34}$$

We see immediately that if the vorticity is zero at any point, then it is zero always, because the evolution depends completely on the vorticity itself. We can therefore take the privileged position to ignore vorticity. The symmetric traceless part of the equation for dH_{ij}/dt then gives

$$\frac{d\sigma_{ij}}{dt} + \frac{2}{3}\theta\sigma_{ij} + \sigma_{ik}\sigma_{kj} - \frac{1}{3}\delta^K_{ij}\sigma^2 + \omega_{ik}\omega_{kj} + \frac{1}{3}\omega^2 = -\Phi_{ij} + \frac{1}{3}\delta^K_{ij}\Phi_{kk} \equiv T_{ij} \ , \tag{3.35}$$

where T_{ij} is the tidal force field. From this we understand that the shear is generated by the tidal field, while vorticity tends to decrease the shear.

From this exercise, we have learned that the description of the fluid as a whole is supplied with another three equations if we allow for vorticity and shear in the Hubble flow. We can also conclude that a fluid with shear can collapse much faster, whereas the spherical collapse is much slower. Later on we will see that the shear and expansion will be key ingredients in the formalism by Thomas Buchert.

4 Spherical Models

Spherical models are a simplified gravitational model for the evolution of regions in a general universe. There are two ways of constructing these models. The first method is using Newtonian dynamics, which seems a valid approximation in small regions (i.e. $r < c/H_0$) of a FRW universe. Another group of models are the Lemaitre-Tolman-Bondi (LTB) models (Lemaître 1933; Tolman 1934; Bondi 1947). These are fully relativistic spherical models which include curvature. The LTB class is very large, and even the FRW can be seen as a member of this class. It turns out that the solutions of the Newtonian approach and the LTB models are exactly the same. The main difference is in terms of the interpretation of the model, because the Newtonian model only knows about a local energy per unit mass, while the LTB model interprets this as curvature of space. The Newtonian model is best used for understanding the principles of spherical models, while the LTB models are better suited for studying backreaction. In fact, there is no backreaction for flat Newtonian cosmologies as will be explained in chapter 5.

The spherical model has the advantage that it is completely non-linear, and does not rely on perturbation theory. The constraint that it is spherical is a reasonable approximation for voids, but not for overdensities. Real overdensities are seldom spherical (see e.g. Shandarin et al. 2006; Zel'Dovich 1970). In a real collapsing structure, any tiny shape disturbance would would lead to tidal forces which greatly enhance the appearance of shear and therefore even more deformation. Non-spherical collapse can therefore occur much faster, as the collapse is concentrated along the minor axis (Icke 1973). But voids evolve in the opposite direction: they become more spherical over time (Icke 1984; Platen et al. 2007). The LTB model was also compared with N-body code for voids, and the results confirmed that a spherical void was well described by a spherical model (Alonso et al. 2010). The spherical model is therefore a good approximation that can qualitatively descibe the evolution of a void profile.

In the following paragraphs we will first analyze a Newtonian homogeneous spherical blob. The basis for this model can be found in several influential articles (Gunn & Gott 1972;

Lahav et al. 1991; Lilje & Lahav 1991; Heath 1977) and the Large Scale Structure handbook (Peebles 1980). It will be shown that such a homogeneous blob evolves similarly to a FRW universe. Then we will analyse a spherical blob with a radial density profile. Again, parallels can be drawn with the FRW universe. During our analysis, we will find that small perturbations from the background universe at initial times barely have a different expansion. At later times, the blobs can completely decouple from the universe and collapse independently. In the last part we will shortly discuss the Lemaitre-Tolman-Bondi model.

4.1 Evolution of a spherical region

The spherical model only involves the gravitational interaction for a non-rotating spherical blob. Our interest will be mostly towards the expansion of the blob relative to the background universe. So what is the most convenient way to define our blob? One of the shell theorems (Zeilik & Gregory 1998) tells us that outside a spherical mass distribution, we can treat the blob as if it were a point in the centre with the same mass as the blob. Therefore we will take the mass of the blob M and keep it conserved, while the outer radius of the blob $r(t)$ will describe the expansion (see figure 4.1).

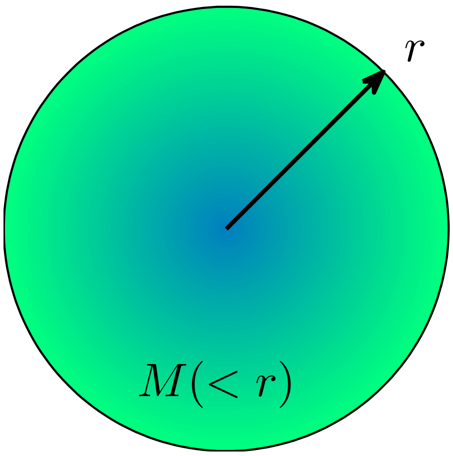

Figure 4.1: A spherical blob of radius r and enclosed mass $M(< r)$. The actual distribution of the density does not matter in such a system, as we are only interested in the evolution of the outer edge of the blob.

The above mentioned shell theorem tells us also that the radial density distribution becomes irrelevant when we want to describe the evolution of the blob as a whole. For ease of notation, we treat the blob as being homogeneous, but one can equally well replace the homogeneous density by the average density of an inhomogeneous but spherically symmetric blob.

With the assumed mass conservation, energy will be conserved as well, because no radiative or decay processes were included in the model. To see how the region expands, we can look at a test particle at the edge of the blob. For a spherical region with enclosed mass M, outer radius $r(t)$ and specific energy E (energy per unit mass of the test particle) we find the following equations of motion

$$\begin{aligned} E &= \frac{1}{2}\dot{r}^2 - \frac{GM}{r} + \frac{\Lambda c^2}{3} r^2 \ , \\ \ddot{r} &= -\frac{GM}{r^2} + \frac{\Lambda c^2}{3} r \ . \end{aligned} \tag{4.1}$$

The first equation is for the conservation of energy for the test particle, while the second equation is Newton's equation with Λ introduced. The shell theorem results from the $1/r^2$ force law. The Λ force term is the only force law that can also partially satisfy this theorem. Outside a spherical mass distribution, the force is still as if the mass were concentrated in a point, but inside a shell, the force does not vanish. Because Λ is very small, no observational constraint is set on the addition of this term.

We assumed that the background universe is exactly homogeneous, so that another of the shell theorems tells us that there is no net force acting from the universe on our blob. The next step is to replace the total mass M by the (average) blob density $\rho_s(t)$, giving the well known equation for the mass of a homogeneous sphere

$$M = \frac{4}{3}\pi \rho_s r^3 \ . \tag{4.2}$$

Our blob was defined using its total conserved mass. From the above equation we can see that mass conservation also implies that the density should evolve as $\rho_s \propto r^{-3}$. This means that when the blob expands, the density should decrease and vice versa. We can make this relation more explicit if we replace the radius r by a unitless scale factor $R(t)$, defined as

$$r(t) \equiv R(t) r_i \ . \tag{4.3}$$

The scale factor is normalized with $R(t_i) \equiv 1$ at some time t_i. This scale factor has again only a local meaning, describing how the blob expands or contracts. Using the scale factor, the explicit equation for the density evolution becomes

$$\rho_s(t) = \rho_{s,\,i} R^{-3} \ , \tag{4.4}$$

where $\rho_{s,\,i} \equiv \rho_s(t_i)$. We can use the normalization at t_i also for the mass M, so that we find $M = \frac{4}{3}\pi \rho_{s,\,i} r_i^3$. The same reasoning holds for the energy of the system E. But before we can define the energy we need to set the kinetic energy by fixing $\dot{R}(t_i)$. One way of doing this is by defining a local Hubble parameter $H_s(t) \equiv \dot{R}(t)/R(t)$.

When we insert the Hubble parameter into the first of the differential equations and take $t = t_i$, we find the energy to be

$$E = \frac{1}{2} H_{s,i}^2 r_i^2 - GM r_i^{-1} - \frac{\Lambda c^2}{3} r_i^2 \ , \tag{4.5}$$

with $H_{s,i} \equiv H_s(t_i)$. The equations of motion that describe the evolution of the blob now become

$$\begin{aligned} \dot{R}^2 &= \frac{8\pi G \rho_{s,i}}{3} R^{-1} + \frac{\Lambda c^2}{3} R^2 + \left(H_{s,i}^2 - \frac{8\pi G \rho_{s,i}}{3} - \frac{\Lambda c^2}{3} \right), \\ \ddot{R} &= -\frac{4\pi G \rho_{s,i}}{3} R^{-2} + \frac{\Lambda c^2}{3} R \ . \end{aligned} \tag{4.6}$$

This looks very much like the FRW equations for a universe without pressure, but now with a local scale factor $R(t)$, a local density $\rho_s(t)$ and a local Hubble parameter $H_s(t)$.

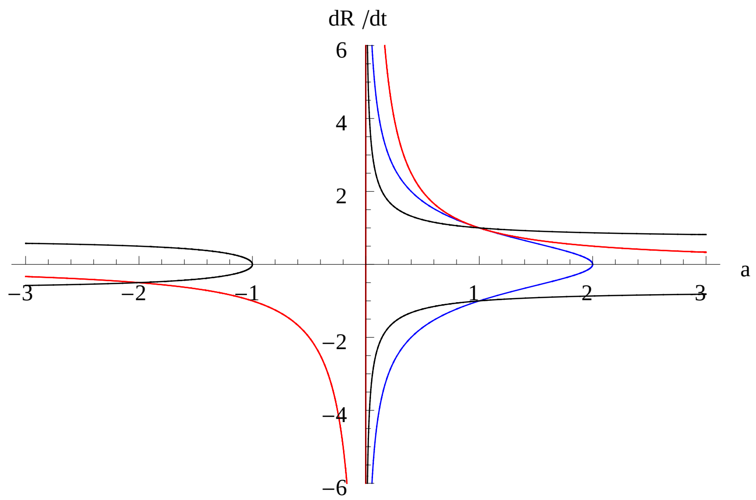

Figure 4.2: Typical curves in the phase diagram for a shell without Λ. The black line corresponds to an open shell, with one root at the negative axis. The red line corresponds to a critical shell, with no roots, but effectively one could say it has two roots at $\pm\infty$. Finally, the blue curve shows a general closed universe, where we have one root on the positive axis. Each of the lines has a positive and negative branch since the energy equation has a square of the velocity. One limiting case which was omitted is $M = 0$. In that case the two branches are horizontal lines, meaning constant velocity so that $R(t) \propto t$. This solution can eventually become relevant inside voids.

The most important equation that determines how the shells evolve is in fact the energy equation, which is the equivalent of the Hubble equation (see fig. 4.2 and equation 2.11). We can plot $\dot{R}$ vs. R to obtain the phase diagram. For the evolution we assume that we start with a singularity at $R = 0$. The equation for $\dot{R}$ has a positive and a negative branch. At $R = 0$ we generally start with the positive branch, the negative branch would correspond to a time-reversed shell. If $\dot{R}(R = 0) > 0$ then the shell starts to expand. This can in principle continue forever, unless the line for $\dot{R}$ crosses the $\dot{R} = 0$ axis at some finite R. This is exactly the moment of turn around at which the shell starts to collapse. Determining how the shell evolves therefore means finding the roots to the energy equation. For the case of $\Lambda = 0$ we find the root at

$$R_{max} = \left(1 - \frac{3H_{s,\,i}^2}{8\pi G\rho_{s,\,i}}\right)^{-1} \quad . \tag{4.7}$$

When $\frac{8}{3}\pi G\rho_{s,\,i} > H_{s,\,i}^2$ ($E < 0$) the energy equation has one positive root at R_{max}, indicating that the shell closes. When $\frac{8}{3}\pi G\rho_{s,\,i} = H_{s,\,i}^2$ ($E = 0$) there is no root because the energy equation only has an R^{-1} term left. Finally, when $\frac{8}{3}\pi G\rho_{s,\,i} < H_{s,\,i}^2$ ($E > 0$) the energy equation has one negative root at R_{max}. This means that the shell will forever expand and never collapse.

We will now try to find the actual solutions to these equations when $\Lambda = 0$. When integrating these equations, we assume that the evolution started at $t = t_B$ with a singularity (t_B as 'Bang time'), so that we have $R(t_B) = 0$. In the specific case that $E = 0$, the solution for this equation is found straightforwardly by integrating the first differential equation. The result is given by

$$R(t) = (6\pi G\rho_{s,\,i})^{1/3}\,(t - t_B)^{2/3} \quad . \tag{4.8}$$

If we let time start at t_B, that is, $t_B = 0$, then we see that this solution is exactly the critical or Einstein-de Sitter solution with $t \propto t^{2/3}$. In the cases where $E \neq 0$ there is no direct formula, but there is a parametrized solution. To find the parametrization we first rewrite both equations into one differential equation (van de Weygaert 2005)

$$R\frac{d}{dt}\left(R\frac{dR}{dt}\right) = E'R + M' \ , \tag{4.9}$$

where we let $E' \equiv H_{s,\,i}^2 - 2M'$ and $M' \equiv \frac{4\pi G\rho_{s,\,i}}{3}$. This differential equation suggests a parametrization in the development angle η, which is defined as $\frac{1}{\sqrt{E'}}R\frac{d}{dt} \equiv \frac{d}{d\eta}$. We then get the following differential equation

$$\frac{d^2R}{d\eta^2} = R + \frac{M'}{E'} \ . \tag{4.10}$$

The solutions to this equation split in two branches, a set of bound solutions for $E < 0$ and a set of unbound solutions for $E > 0$,

$$\begin{aligned} E > 0: \ \ R(\eta) &= \frac{M'}{E'}\,(\cosh\eta - 1) \ , \\ E < 0: \ \ R(\eta) &= \frac{M'}{E'}\,(\cos\eta - 1) \ . \end{aligned} \tag{4.11}$$

The parameter η is called the development angle, because it is effectively an angle that describes the evolution of the system. But knowing how R evolves with η is not enough, we would also like to know how time runs with η. This can be obtained by integrating the definition of η, resulting in

$$\begin{aligned} E > 0: \; t(\eta) - t_B &= \frac{M'}{|E'|^{3/2}} (\sinh\eta - \eta) \;, \\ E < 0: \; t(\eta) - t_B &= \frac{M'}{|E'|^{3/2}} (\eta - \sin\eta) \;, \end{aligned} \tag{4.12}$$

where we fixed $\eta(R = 0) = 0$. These are in fact exactly the closed/bound and open/unbounded solutions from the FRW equations without radiation or dark energy, apart from a few constants and multiplication values.

So far we have seen that for $\Lambda = 0$ the correspondence between a spherical blob and the FRW dust universe is remarkable. It turns out that this holds in general for the solutions of the spherical model. Now what if we make our blob a completely normal region in such a FRW universe? In that case we need to take the density of the universe $\rho_u(t)$ and the global Hubble parameter $H(t)$. In cosmology, we often set the boundary conditions at today, so that $t_i = t_0$ where t_0 is today (and we replace all subscripts i with 0). We then see that the resulting expansion exactly matches that of the background universe. Therefore it is reasonable to replace the local scale factor $R(t)$ by the global scale factor $a(t)$. The equations of motion then become

$$\begin{aligned} H^2 &= \frac{8\pi G\rho_{u,0}}{3} a^{-3} + \frac{\Lambda c^2}{3} + \left(H_0^2 - \frac{8\pi G\rho_{u,0}}{3} - \frac{\Lambda c^2}{3}\right) a^{-2} \;, \\ \frac{\ddot{a}}{a} &= -\frac{4\pi G\rho_{u,0}}{3} a^{-3} + \frac{\Lambda c^2}{3} \;, \end{aligned} \tag{4.13}$$

Finalizing the transformation of the spherical model to the common form of the FRW equations we can again introduce the critical density ρ_c and the density parameter Ω (see equation 2.15).

$$\begin{aligned} H^2 &= H_0^2 \left(\frac{\Omega_{m,0}}{a^3} + \Omega_{\Lambda,0} + \frac{1 - \Omega_{m,0} - \Omega_{\Lambda,0}}{a^2}\right) \;, \\ \frac{\ddot{a}}{a} &= H_0^2 \left(-\frac{\Omega_{m,0}}{2a^3} + \Omega_{\Lambda,0}\right) \;, \end{aligned} \tag{4.14}$$

with $\Omega_{m,0} \equiv \Omega_m(t_0)$. We can find the specific energy of the test particle by combining equation 4.5 with the above result to find

$$E = \tfrac{1}{2} H_0^2 \left(1 - \Omega_{m,0} - \Omega_{\Lambda,0}\right) r_0^2 \;. \tag{4.15}$$

We might be tempted to call this the curvature as we do with the FRW equations, because this term has exactly the same mathematical form. However, in our local approach there is no curvature. Classical dynamics does not know about curvature, it assumes a flat space. Therefore, we can only interpret this term as the energy of the blob. Interpretating this term as the curvature of the universe is only justified when using General Relativity. On the other hand, the effective result on the expansion is the same, therefore allowing us to ignore this difference when not dealing with proper distances.

What we have proven so far is that we can describe the evolution of a spherical region in the universe as a whole by using (semi-) classical dynamics. We also showed that the specific case where the region is exactly a part of the universe results in the same evolution as the background universe for universes without pressure.

4.2 Evolution of a spherical density profile

So far we only considered how a homogeneous spherical region evolves as a whole. What if we want to know how the density inside the region evolves with time? To approach this problem we can again use the shell theorems. This means that outside a spherical mass distribution, the force is the same as that of a point-source, and inside a spherical shell, no force is present, except for Λ. So if the density distribution is spherically symmetric, then at each point in the sphere we can ignore the matter further outward. At the same time, all that matters for the gravitational interaction is the matter at smaller radii. This opens up the possibility to separate our continuous profile in a set of concentric shells (see figure 4.3).

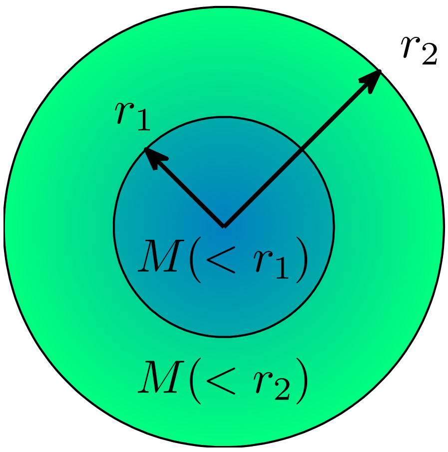

Figure 4.3: A spherical blob with two shells of radius r_1 and r_2. For the evolution of the shells, all that matters is the enclosed mass within their radius. This model works as long as the shells do not cross, which can happen if the inner region is sufficiently empty.

For each shell the mass within the radius of the shell, i.e. $M(< r)$ determines its evolution. Generally we would like to use the shells as thin as possible to get the smoothest result for the evolution of the density profile. The method to evolve the profile is to take each shell and compute the total mass it encloses. After that, we let it evolve using the same equations of motion as in the previous paragraph. The difference with the evolution of the blob as a whole is that *each* shell can have different boundary conditions on density and initial velocity. The resulting equations of motion then become

$$\begin{aligned}\dot{R}_n^2 &= \frac{8\pi G\bar{\rho}_{n,i}}{3}R_n^{-1} + \frac{\Lambda c^2}{3} + \left(H_{n,i}^2 - \frac{8\pi G\bar{\rho}_{n,i}}{3} - \frac{\Lambda c^2}{3}\right), \\ \ddot{R}_n &= -\frac{4\pi G\bar{\rho}_{n,i}}{3}R_n^{-2} + \frac{\Lambda c^2}{3}\ ,\end{aligned} \tag{4.16}$$

with n the index for each concentric shell, $\bar{\rho}_{n,0}$ the average density of the enclosed mass and $H_{n,0}$ the shell Hubble parameter. This average density $\bar{\rho}_{n,0}$ seems artificial, but remember that it is the enclosed mass M_n that determines the evolution of the shell.

The introduction of a radial dependence has a very important new feature: shell crossing. This is caused by the crowding of shells and can occur in steep void profiles. The inner shells in a void expand much faster, and catch up with the outer shells. The sharper the transition between void and wall, the more chance of shell crossing. With shell crossing there is however the problem that the inner shells do not only catch up with the outer shells, but they also move beyond them. This causes a violation of the radial mass conservation, meaning that the spherical model starts to lose its significance. It has been found that beyond shell-crossing the actual evolution continues in a self-similar manner (Bertschinger 1985). This means that the shape remains the same, but the size expands. The spherical model cannot reproduce this result because it only deals with pressureless matter, while pressure would play a role in preventing the shell crossing. Therefore, if shell crossing occurs then the shells involved lose their physical meaning, which should be done by marking all observables in these shells as invalid. Averaging over all shells is in that case also not possible. A full overview of shell crossings is provided in Hellaby & Lake 1985.

4.3 Evolving a small perturbation

In this paragraph we will build a model that applies the spherical model to evolve small matter perturbations in a FRW dust universe. We already showed that we can use the spherical model to find the FRW equations for pressureless dust. But we would really be interested in how a perturbed spherical region in such a FRW universe would evolve. This can be achieved by introducing a background universe and then inserting a spherical blob. The spherical blob will be defined in terms of the background, though its evolution is still determined by the spherical model. We will show that in this case, the physical interpretation of the blob (such as whether it collapses) is directly tied to the background universe. This allows us to really see how perturbations evolve in a universe.

Let us assume we have a matter dominated universe. At very early times (in our universe at $z \approx 1000$), this universe was nearly completely homogeneous, apart from small (Gaussian) perturbations in density and/or velocity. We can separate the universe in the homogeneous part, which we use as the background, and the inhomogeneous part, which we use for the spherical blobs. Let us assume we can find the density profile of a typical density perturbation in the universe. First of all, we can define the density perturbation as

$$\delta(\vec{r}, t) \equiv \frac{\rho(\vec{r}, t)}{\rho_u(t)} - 1 \ , \tag{4.17}$$

where $\rho(\vec{r}, t)$ is the density at some position $\vec{r}$ and time t, while $\rho_u(t)$ is the background density at that time. In the case of a radial perturbation profile $\delta(r, t)$ we can split the profile in a set of concentric shells. As we explained in the previous paragraph, all that matters is the mass within the shell, which means integrating over the profile

$$M(< r) = \int_0^r 4\pi r'^2 dr' \rho(r') = \frac{4\pi r^3}{3}\rho_u \left(1 + \frac{3}{r^3}\int_0^r r'^2 dr' \delta(r')\right) \ . \tag{4.18}$$

If we take the mean density of matter $\bar{\rho}(r)$ inside radius r we can also find the mean overdensity $\Delta(r, t)$. The mean overdensity tells us how much the mean density of the enclosed mass differs from the background density

$$\Delta(r) \equiv \frac{\bar{\rho}(r)}{\rho_u} - 1 = \frac{M(< r)}{\frac{4}{3}\pi r^3 \rho_u} - 1 = \frac{3}{r^3}\int_0^r r'^2 dr' \delta(r') \tag{4.19}$$

What we have done is introducing a moving average: an average that is defined for each and every shell over all shells that lie within that shell.

As explained before, the initial conditions are set at early times in the universe. For the evolution of the perturbations we are now interested in the expansion of the shells compared to the expansion of the universe. If the global expansion factor is given by $a(t)$ with $a(t_0) = 1$ with t_0 fixed at today, and the local expansion factor given by $R(t)$ with $R(t_i) = 1$ with t_i set at early times, then the comoving radius of a shell is given by

$$x(t) \equiv \frac{r(t)}{a(t)} = \frac{R(t)}{a(t)} r_i \ , \tag{4.20}$$

where one has a different comoving radius for each shell. The comoving radius therefore tells us about the relative expansion of the spherical region with respect to the background universe. Using the reference time t_i we can also set up how the average overdensity $\Delta(r, t)$ evolves with time. Within each shell we have mass conservation, while the shell mass is given by $M(< r) = \frac{4}{3}\pi r^3 \rho_u (1 + \Delta)$. To conserve mass, we need that the average overdensity $\Delta(r, t)$ evolves as $1 + \Delta \propto R^{-3} a^3$ because we know that $\rho_u = \rho_0 a^{-3}$. Explicity, the evolution of $\Delta(r, t)$ becomes

$$1 + \Delta = \left(\frac{a}{a_i}\right)^3 R^{-3} (1 + \Delta_i) = \left(\frac{x}{x_i}\right)^{-3} (1 + \Delta_i) \ , \tag{4.21}$$

with $\Delta_i = \Delta(r_i, t_i)$ and $x_i = x(t_i)$. The above equation tells us how the average density perturbation evolves with time while the universe expands in its own way. The mean density within a shell at initial time is now given by $\rho_{u,i}(1 + \Delta_i)$. We can rewrite this in terms of the density parameter Ω by using the critical density of the universe ρ_c, resulting in

$$\frac{8\pi G \bar{\rho}_i}{3H_i^2} = \Omega_i (1 + \Delta_i) \equiv 1 + \Delta_{ci} \ , \tag{4.22}$$

where the last equation introduces Δ_{ci} for ease of notation. What remains is to define the energy of the shells. We define the kinetic energy perturbation $\alpha(r, t)$ as the energy deficit with respect to the kinetic energy of the Hubble flow

$$\alpha \equiv \left(\frac{v}{v_H}\right)^2 - 1 \ , \tag{4.23}$$

with $v_H = Hr$. We can try to find the local Hubble parameter $H_s = v/r$ using the above expression, resulting in

$$H_s^2 = H^2 (1 + \alpha) \, . \tag{4.24}$$

We then find at time t_i that $H_{s,i}^2 = H_i^2 (1 + \alpha_i)$, with α_i again only a minor perturbation from the Hubble flow at t_i. A commonly used α_i is the one that can be found using the linear theory approximation for the peculiar velocity

$$v_{\text{pec}} = -\frac{1}{3} H_i r_i f(\Omega_m) \Delta_i \ . \tag{4.25}$$

This can be derived by using the potential of a spherical mass distribution in the expression for the peculiar velocity (equation 3.24).
The total equations then become

$$\begin{aligned} \dot{R}^2 &= H_i^2 \left[\frac{\Omega_{m,i}(1 + \Delta_i)}{R} + \Omega_{\Lambda,i} R^2 + (\alpha_i - \Delta_{ci} - \Omega_{\Lambda,i}) \right] \ , \\ \ddot{R} &= -H_i^2 \frac{\Omega_{m,i}(1 + \Delta_i)}{2R^2} + \Omega_{\Lambda,i} R \ , \end{aligned} \tag{4.26}$$

leaving out the shell index n for clarity. We only relabelled the known differential equation with information on the perturbations and the background. The solutions are again those as before, but the difference in the model is now in what observables we look at. For the matter dominated non-critical case, we find the solution factors as (see equations 4.12, 4.13) as

$$\frac{M'}{E'} = \frac{1}{2} \frac{1 + \Delta_{ci}}{\alpha_i - \Delta_{ci}} \ . \tag{4.27}$$

$$\frac{M'}{|E'|^{3/2}} = \frac{1}{2H_i} \frac{1 + \Delta_{ci}}{|\alpha_i - \Delta_{ci}|^{3/2}} \ . \tag{4.28}$$

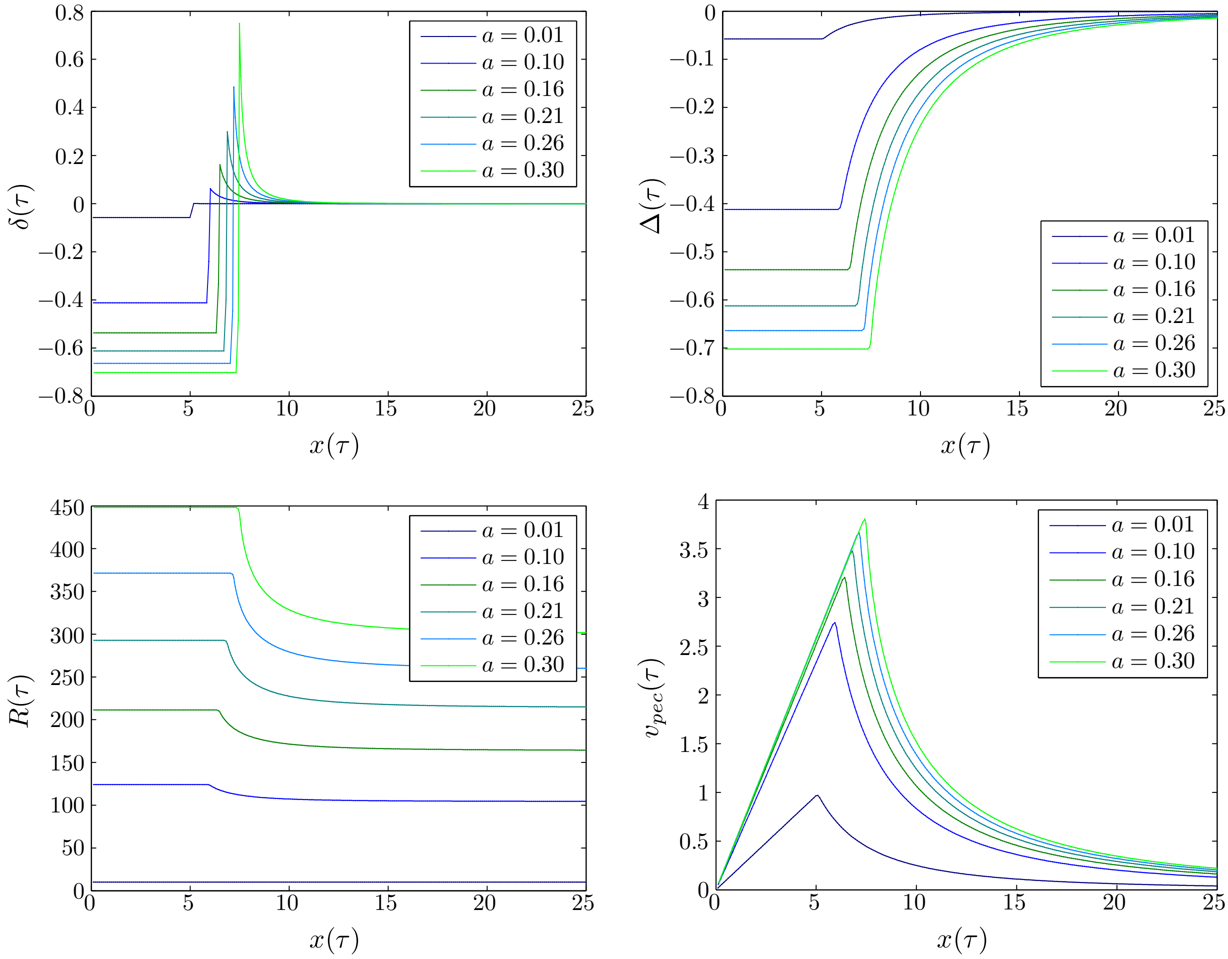

Figure 4.4: Expanding tophat void in comoving space ($\delta_L = -10$) for an Einstein-de Sitter universe. On the horizontal axes is the comoving radius x in Mpc. Top left: overdensity δ. As we can see, the boxy void shape expands rapidly in the centre, while at the edge of the void, a strong overdensity is created. This overdensity is not caused by the collapse of shells as with the collapse of a cloud of matter, but by the crowding of shells near the edge. Eventually these shells will cross, causing the shell-crossing phenomena in which radial mass conservation does not hold anymore. Top right: integrated overdensity Δ. This represents the enclosed mass, thus evolving smoothly without forming ridges. Bottom left: Local expansion factor R. We clearly see that it runs ahead of the global expansion inside the void. Notice also that if we normalize it as $R_0 = 1$ then the expansion factor would seem to be behind at first in the void. Bottom right: peculiar velocities. We see that a strong outward motion is present in the void, which only slowly decays beyond the ridge of the void.

The evolution of the density perturbation $\delta(r, t)$ is not determined by only the evolution of the shell, but by the evolution of the shell with respect to the expansion of the universe.

Figure 4.4 shows an example of the model with a tophat void profile (i.e. a stepfunction) in

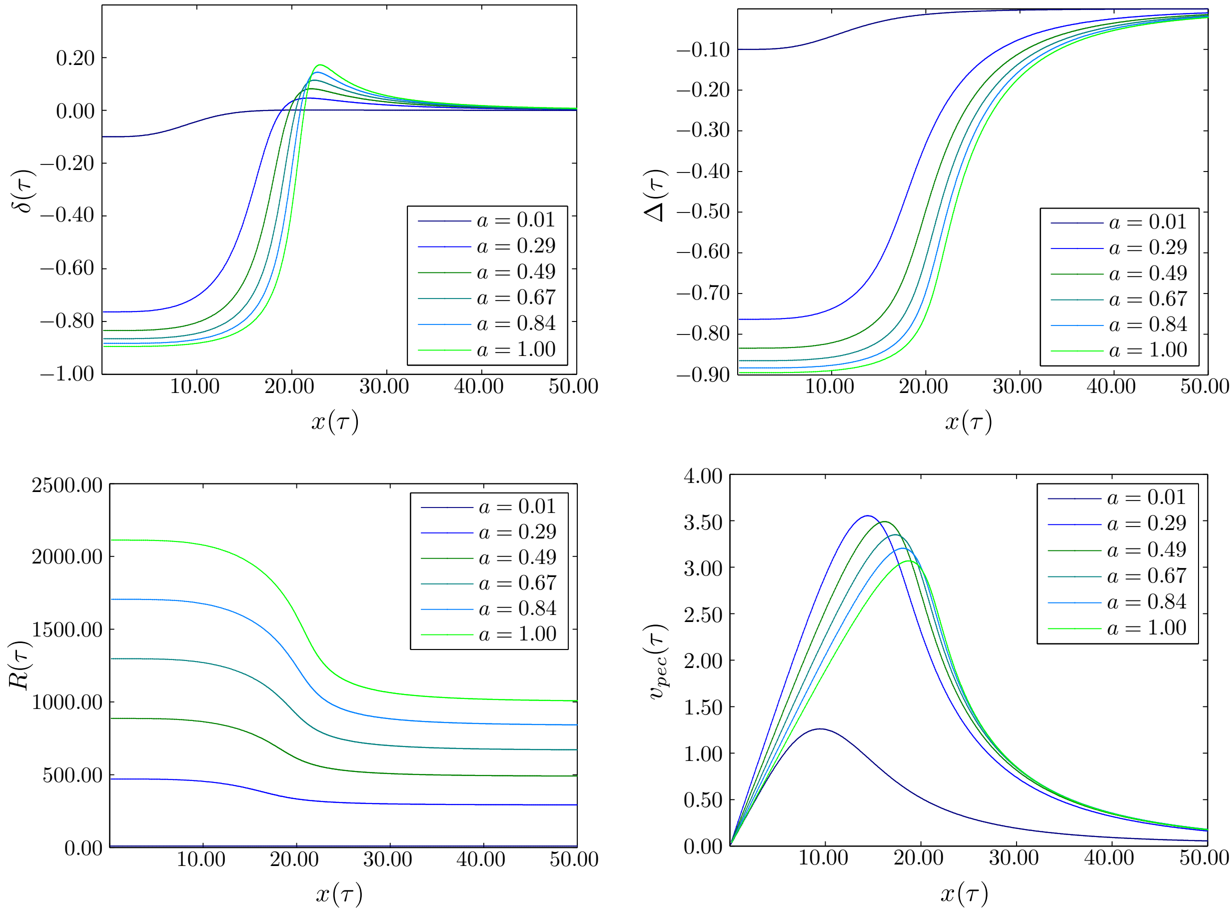

Figure 4.5: Expanding CDM void in comoving space ($\delta_L = -5$) for an $\Omega_m = 0.3$ universe. On the horizontal axes is the comoving radius x in Mpc. The different plots are as in figure 4.4. The behaviour of this more realistic void is similar to that of the tophat void, but the sharpness of the ridge around the void is not there. This means that shell-crossing will not occur until much later in the evolution of the ridge. To make the comparison better, this void was even evolved to $a = 1$ instead of $a = 0.3$.

an Einstein-de Sitter universe. Around the ridge, a strong velocity field emerges, moving outward. Eventually the outer shells will not be able to keep up with the inner shells, causing shell crossing. This happens rather quick for top-hat voids, while for ordinary voids it can only happen if the profile is steep enough (see figure 4.5).

4.4 Special cases

At early times we have a very small expansion factor ($a_i \ll 1$), which we can use to find $\Omega_{m,\,i}$ (for typical values of $\Omega_{m,\,0}$ and $\Omega_{\Lambda,\,0}$ in the range 0.1 to 2)

$$\Omega_{m,\,i} = \frac{H_0^2}{H_i^2}\Omega_{m,\,0}a_i^{-3} = \left(1 + \frac{\Omega_{\Lambda,\,0}}{\Omega_{m,\,0}}a_i^3 + \frac{1-\Omega_{m,\,0}-\Omega_{\Lambda,\,0}}{\Omega_{m,\,0}}a_i\right)^{-1} \approx 1 \ . \tag{4.29}$$

At initial times, $\Omega_{m,\,i}$ is brought very close to 1, while at late times it can deviate a lot from this. A small perturbation at initial time may therefore significantly change the effective value of $\Omega_{m,\,0}$ a lot compared to the background universe. This is exactly why this model is interesting, because we can really study whether a shell collapses, and how the density profile evolves.

We will now shortly describe a few situations in matter dominated universes, which are also reasonably valid for small Λ. If the universe is closed and the shell is open, then the shell will not close until very near the collapse time of the universe. This is because only at the very last moment the shrinking of the universe is large enough to take over the expanding shell. Another situation is a system where we have an open universe and a shell perturbed to collapse. In that case we can find the collapse time by looking at the closed solution with development angle $\eta = 2\pi$

$$t_c - t_B = \pi H_i^{-1}\frac{\Omega_{m,\,i}\,(1+\Delta_i)}{(\alpha_i - \Delta_{ci})^{3/2}} \ . \tag{4.30}$$

Using the initial conditions for the peculiar velocity (4.24) we find that $\alpha_i - \Delta_{ci} \approx \frac{5}{3}\Delta_i$. Using this and the expansion of H_i to $\Omega_{m,\,0}$ we find for the collapse time (at fixed H_0 and a_i)

$$t_c - t_B \propto \left(\sqrt{\Omega_{m\,0}}\Delta_i^{3/2}\right)^{-1} \ . \tag{4.31}$$

This means that a larger perturbation collapses faster, but an emptier universe pulls it the other way. These results will be modified by Λ, generally delaying or preventing collapse for $\Lambda > 0$, while accelerating collapse for $\Lambda < 0$.

Two important numbers can be derived from the overdense matter dominated spherical model. First of all, we can derive the linear overdensity at turnaround δ_t. This is the density that is obtained through the linear theory, at the time that the spherical model collapses. It is found by assuming a background Einstein-de Sitter universe and looking at the moment of turn-around or collapse ($\eta = \pi$ or $\eta = 2\pi$ respectively). We proceed from here by approximating $\alpha_i - \Delta_{ci} \approx \frac{5}{3}\Delta_i$. We rewrite this using the linear growth law in an EdS universe ($D(t)/D(t_i) = (t/t_i)^{2/3}$) and solve towards Δ_i, which is the value δ_t^L that we are looking for. So the first steps give

$$\delta^L = \frac{5}{3}\left(\frac{3(\sin\eta - \eta)}{4}\right)^{2/3} \ . \tag{4.32}$$

This results in

$$\delta_t^L = \frac{3}{5}\left(\frac{3\pi}{4}\right)^{2/3} \approx 1.062 \ . \tag{4.33}$$

We can also look at the linear density of collapse, by looking at the moment of collapse ($\eta = 2\pi$). We then find the result

$$\delta_c^L = \frac{3}{5}\left(\frac{3\pi}{2}\right)^{2/3} \approx 1.686 \ . \tag{4.34}$$

The evolution of these numbers is linear, so $\delta_c(z) = D(t)\delta_c$. These numbers will be useful in determining which structures can be collapsed in a linear density field. A similar approach can be followed for voids using the underdense spherical model. In that case, we would like to know when a void really can be marked as such. One proposal is to look for the moment of shell-crossing, which occurs at the moment that the shells crowd in comoving space

$$\frac{dR(r_i, t)}{dr_i} = 0 \ . \tag{4.35}$$

In a spherical tophat void, this can already happen quite early in the evolution of the void. Doing the full analysis with a tophat, one can prove that this happens when $\eta \approx 3.53$. We can then find the linear density (using the open shell) as

$$\delta_v \approx -2.81 \ . \tag{4.36}$$

This number is often used to mark voids in a linear density field.

4.5 Lemaitre-Tolman-Bondi models

The Lemaitre-Tolman-Bondi (LTB) solutions are the relativistic generalization of the spherical model. The solutions that we found for the Newtonian spherical model are also found in the LTB models. The important difference is that the interpretation of the energy is that of a local curvature. The result is that the observed quantities are slightly disturbed due to the curvature of space. A thorough review can be found in Sussman 2008 and Sussman 2010.

The LTB model has attracted quite some attention during the years, because it allows a fully relativistic description of a spherical void or blob in time. Many models that try to find alternatives for dark energy have been simulated using LTB models. But even the Friedmann models are contained in the wide class of LTB models, as they are the homogeneous models in the LTB class.

The starting point for the LTB models is the metric, which contains a radial gradient in the expansion factor

$$ds^2 = -c^2 dt^2 + \frac{r'^2}{1-k(r_i)} dr_i^2 + r^2 d\Omega \ , \tag{4.37}$$

with r_i the comoving coordinate, r the physical coordinate, $k(r_i)$ the curvature and $r' = dr/dr_i$ the position dependence. We assume that $r(r_i, t) = R(r_i, t) r_i$. Doing the full math (with a cosmological constant), we find again a Hubble equation with $H_s = \dot{r}/r$ as

$$H_s^2(r_i, t) = H_i^2 \left(\frac{1 + \Delta_{ci}}{R(r_i, t)^3} + \Omega_{\Lambda,i} + \frac{\alpha_i - \Delta_{ci} - \Omega_{\Lambda,i}}{R(r_i, t)^2} \right) . \tag{4.38}$$

Very often these equations are presented with the Ω's defined locally with each its own Hubble parameter $H_s(r_i, t)$

$$\Omega_i(r_i) = \frac{8\pi G \bar{\rho}_i}{3H_{s,\,i}^2} . \tag{4.39}$$

However, this replacement hides the perturbations and the fact that Λ remains the same throughout the universe. The density within the shells is still the average as defined before, with one difference. The enclosed mass is now the quasi-local, because the average did not take into account the curvature of space. This means that the actual density will slightly differ from the proper observed density. One solution would be to solve for the curvature so that density profile matches with the 'observed' boundary conditions. But the difference is not very important, because we want to see the magnitude of some density profile. The actual density profile is just slightly altered from the input profile.

The solutions can be shown to be exactly those of the Newtonian spherical model. As already indicated, there is a difference in averaging observables, because this model has curvature. Proper distances are therefore different than in the Newtonian model. We find the following volume element with the curvature of space

$$dV = 4\pi r(r_i, t)^2 r'(r_i, t) dr_i \Rightarrow dV = 4\pi \frac{r(r_i, t)^2 r'(r_i, t)}{\sqrt{1 - k(r_i)}} dr_i . \tag{4.40}$$

This will later turn out to be essential for the evaluation of the cosmic backreaction problem, as it remains only in non-flat spaces, so that the full integral with curvature is essential. However, the curvature is generally very small, because the curvature is given by

$$k(r_i) = \frac{H_i^2 r_i^2}{c^2} \left(\alpha_i(r_i) - \Delta_{ci}(r_i) - \Omega_{\Lambda,i} \right) , \tag{4.41}$$

with $\frac{H_i^2 r_i^2}{c^2}$ of order 10^{-6}. A series expansion of the volume element gives (Mattsson & Mattsson 2010)

$$\frac{1}{\sqrt{1 - k(r_i)}} = 1 + \frac{k(r_i)}{2} + \mathcal{O}(k^2(r_i)) . \tag{4.42}$$

The difference with curvature is therefore only present in the higher order terms. The effect of curvature is present, but for subhorizon structures ($r < c/H$) it is not a large factor.

We now have a model that can describe the evolution of a void for a given density profile. In the next section we will see how to apply backreaction in these models, while after that we will make the initial conditions for these models.

5 Cosmic backreaction

Around 1997, the field of cosmic backreaction was set in motion when Thomas Buchert published his first article with Jürgen Ehlers on averaging Newtonian cosmologies. The idea is that evolution and averaging are two operators that do not necessarily commute. This is important in cosmology, because the universe is not strictly homogeneous, but only homogeneous in an average sense, as far as we can observe (see figure 5.1). How can we be sure that the average dynamics of the universe is described by the evolution of the average universe?

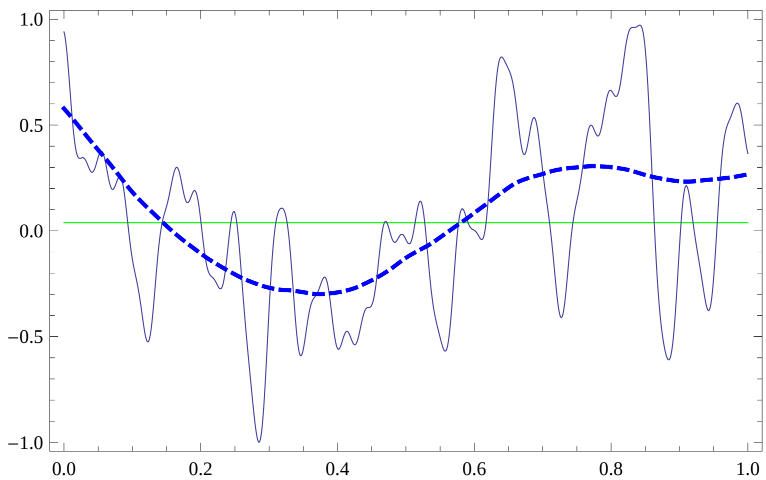

Figure 5.1: Cross-section of a universe with density fluctuations. The different lines represent averaging on different scales. The thin blue line shows averaging on small scales, which results in much structure, while the thick dashed line shows the result of averaging on a much larger scale. Finally, the thin green line shows the average over the whole universe. The question is whether averaging influences our picture of the dynamics of the universe.

A very down to earth example, where averaging causes trouble is the production efficiency of workers in a factory. Suppose the workers in the factory are equally efficient, until beyond age 55, when their efficiency slowly drops by 2% per year. If our factory consists of a homogeneous population of workers at age 40, then the average efficiency of the workers is equal to the efficiency of the average worker. So any worker will do to describe the efficiency of the whole factory. On the other hand, suppose the factory has an inhomogeneous workforce of 70% workers at age 40, and the other 30% at age 60. In that case, the average worker will not be representative of the efficiency of the factory, because some workers are less efficient. We see that averaging sometimes obscures peculiarities in underlying distributions.

This is exactly what Buchert tries to convey. Perhaps the necessity for Dark Energy comes from our description of the universe, in which the average universe is taken as the basis for the Friedmann equations. What if the average universe does not directly relate to the background? This is exactly what happens in the Buchert formalism, as an extra layer is included between a true, inhomogeneous universe, and the observed averaged universe. The Buchert formalism does this by introducing a proper averaging scheme that actually can lead to effects similar to that of Λ, though the magnitude of the effect is still heavily debated.

5.1 Averaging the equations of motion

The first step in the Buchert formalism is to define an average. Evidently, gauge choice problems may arise, though generally these can be ignored if we only consider a universe with irrotational dust. Another issue is that the average of a tensor is not easily defined in a nice covariant way. The Buchert formalism instead only focuses on the averaging of scalars, which is a well-defined problem. In that case, we can define a spatial average by integrating over a hypersurface of constant proper time t and divide by the volume of the hypersurface (see Buchert 2000; Räsänen 2008). We can define the average of a scalar $S(x,t)$ over some domain $\mathcal{D}$ as follows

$$\langle S \rangle_{\mathcal{D}} = \frac{\int_{\mathcal{D}} S(x,t) dV}{\int_{\mathcal{D}} dV} \ , \tag{5.1}$$

with g the determinant of the spatial metric. The relativistic volume element dV is given by

$$dV = \sqrt{g} d^3x = \frac{r(\vec{x},t)^2 r'(\vec{x},t) \sin\theta}{\sqrt{1-k(x)}} dx d\theta d\phi \ , \tag{5.2}$$

with x the comoving radius (which for the spherical model is r_i) and $x' = \partial r / \partial x$. In the non-relativistic case, the curvature part becomes 1, while in a strictly homogeneous universe we find the standard expansion of a fluid element

$$\sqrt{g} d^3x = \frac{x^2 a^3(t) \sin\theta}{\sqrt{1-k}} dx d\theta d\phi \ . \tag{5.3}$$

We continue with the full volume element. The expansion of dV is fully contained in $J \equiv \sqrt{g}$. The expansion scalar can then be found by taking the time derivative of J

$$\dot{J} = \theta J \ , \tag{5.4}$$

with θ the velocity divergence. With this relation we can find the average of θ as

$$\frac{\dot{V}_{\mathcal{D}}}{V_{\mathcal{D}}} = \frac{\int_{\mathcal{D}} \dot{J} d^3x}{\int_{\mathcal{D}} J d^3x} = \frac{\int_{\mathcal{D}} \theta dV}{\int_{\mathcal{D}} dV} = \langle \theta \rangle_{\mathcal{D}} \ . \tag{5.5}$$

This allows us to find the time evolution of the average of a scalar

$$\frac{d}{dt} \langle S \rangle_{\mathcal{D}} - \left\langle \frac{dS}{dt} \right\rangle_{\mathcal{D}} = \langle \theta S \rangle_{\mathcal{D}} - \langle \theta \rangle_{\mathcal{D}} \langle S \rangle_{\mathcal{D}} \tag{5.6}$$

For the expansion scalar θ this results in the following relation

$$\frac{d}{dt} \langle \theta \rangle_{\mathcal{D}} - \left\langle \dot{\theta} \right\rangle_{\mathcal{D}} = \left\langle \theta^2 \right\rangle_{\mathcal{D}} - \langle \theta \rangle_{\mathcal{D}}^2 \tag{5.7}$$

In the last section on structure growth, we already saw the Raychoudhury equation. We derived it indirectly using a generalized Hubble flow. It can also be found directly from the Einstein equations, being one of the two equations that is found trough the scalar part. The continuity equation comes from the covariant conservation law. The resulting equations of motion are in that case

$$\dot{\theta} + \frac{1}{3}\theta^2 = -4\pi G\rho + \Lambda - \sigma^2 + \omega^2 \ , \tag{5.8}$$

$$\frac{1}{3}\theta^2 = 8\pi G\rho + \Lambda - \frac{1}{2}{}^{(3)}R + \frac{\sigma^2}{2} - \frac{\omega^2}{2} \ , \tag{5.9}$$

$$0 = \dot{\rho} + \theta\rho \ , \tag{5.10}$$

with ${}^{(3)}\mathcal{R}$ the Ricci scalar, representing the curvature. Before using the Buchert formalism on the equations of motion, we need to define the average expansion factor $a_{\mathcal{D}}(t)$

$$a_{\mathcal{D}}(t) = \left(\frac{V_{\mathcal{D}(t)}}{V_{\mathcal{D}(t_0)}} \right)^{1/3} \ , \tag{5.11}$$

from which we can infer the relation with $\langle \theta \rangle_{\mathcal{D}}$

$$\langle \theta \rangle_{\mathcal{D}} = 3\frac{\dot{a}_{\mathcal{D}}}{a_{\mathcal{D}}} \equiv 3H_{\mathcal{D}} \ . \tag{5.12}$$

The last step also defined the average Hubble parameter. Without initial vorticity, no vorticity will show up, therefore we can ignore the vorticity when averaging the Einstein equations. The average of the equations of motion then becomes (Buchert, 2000)

$$\frac{\ddot{a}_{\mathcal{D}}}{\dot{a}_{\mathcal{D}}} = -\frac{4\pi G \langle\rho\rangle}{3} + \frac{\mathcal{Q}_{\mathcal{D}}}{3} + \frac{\Lambda c^2}{3} \ , \tag{5.13}$$

$$\frac{\dot{a}_{\mathcal{D}}^2}{a_{\mathcal{D}}^2} = \frac{8\pi G \langle\rho\rangle}{3} + \frac{\Lambda c^2}{3} - \frac{1}{6}\left\langle {}^{(3)}\mathcal{R} \right\rangle - \frac{1}{6}\mathcal{Q}_{\mathcal{D}} \ , \tag{5.14}$$

$$0 = \frac{d\langle\rho\rangle}{dt} + \langle\theta\rangle\langle\rho\rangle \ . \tag{5.15}$$

These equations were set up in such a way that they exactly reduce to the ordinary FRW equations in the case of no backreaction. The backreaction is contained in the term $\mathcal{Q}_{\mathcal{D}}$, which is given by

$$\mathcal{Q}_{\mathcal{D}} \equiv \frac{2}{3}\left(\left\langle\theta^2\right\rangle - \langle\theta\rangle^2\right) - 2\left\langle\sigma^2\right\rangle \ . \tag{5.16}$$

This term quantifies the effect of inhomogeneities on the evolution of the universe. Finally, the averaging resultets in one extra equation, which is only an integrability condition

$$\frac{1}{a_{\mathcal{D}}^6}\partial_t\left(\mathcal{Q}_{\mathcal{D}} a_{\mathcal{D}}^6\right) + \frac{1}{a_{\mathcal{D}}^2}\partial_t\left(\left\langle {}^{(3)}\mathcal{R}\right\rangle_{\mathcal{D}} a_{\mathcal{D}}^2\right) = 0 \ . \tag{5.17}$$

This equation makes sure that the average equations can be written nearly as the FRW equations.

We notice that apparently the average dynamics result in an emergent contribution of the inhomogeneity to the equations of motion. This effect is not seen when only considering local non-averaged equations. The resulting equations are not a solution of Einstein's field equation, but they provide an intermediate layer between what we observe on the largest scales, and what the universe actually is. Their most appealing effect is that they might be able to explain some of the cosmological constant.

5.2 Averaging in a spherical model

We can try and apply the Buchert formalism to a spherical model, including curvature. First of all we take the spherical volume element

$$dV = 4\pi\frac{r(r_i,t)^2 r'(r_i,t)}{\sqrt{1-k(r_i)}}dr_i \ , \tag{5.18}$$

with r_i the comoving coordinate and $r(r_i,t) = R(r_i,t)r_i$ the physical coordinate. In that case, the volume expansion scalar θ is given by

$$\theta = \vec{\nabla}\cdot\vec{u} = \frac{1}{r^2}\frac{\partial}{\partial r}\left(r^2 u\right) = \frac{2u}{r} + \frac{du}{dr} = 2\frac{\dot{r}}{r} + \frac{d\dot{r}}{dr} \ , \tag{5.19}$$

with $\vec{u} = du/dr$ the physical velocity. There is no effect of curvature in this equation. This can be seen in the definition of the volume element, in which the curvature part is time independent. This results in the term dropping out as in the expansion rate θ. The shear is slightly more difficult, as we are now in spherical coordinates, unlike in the previous chapter. The only non-zero components are those along the trace, which contain the terms $-\frac{1}{3}\theta$, while the σ_{rr} term also contains dv/dr. We find the following non-zero elements

$$\sigma_{rr} = \frac{d\dot{r}}{dr} - \frac{1}{3}\theta \ , \tag{5.20}$$

$$\sigma_{\theta\theta} = -\frac{1}{3}\theta \ , \tag{5.21}$$

$$\sigma_{\phi\phi} = -\frac{1}{3}\theta \ . \tag{5.22}$$

The squared shear is then given by

$$\sigma^2 = \sigma_{ij}\sigma^{ij} = \sigma_{rr}^2 + \sigma_{\theta\theta}^2 + \sigma_{\phi\phi}^2 = \frac{2}{3}\left(\frac{\dot{r}}{r} - \frac{d\dot{r}}{dr}\right)^2 \ . \tag{5.23}$$

We can use this to find the backreaction.

$$\mathcal{Q} = \frac{2}{3}\left(\left\langle\theta^2\right\rangle_{\mathcal{D}} - \langle\theta\rangle_{\mathcal{D}}^2\right) - \left\langle\sigma^2\right\rangle_{\mathcal{D}} = \left\langle\frac{2}{3}\theta^2 - \sigma^2\right\rangle_{\mathcal{D}} - \frac{2}{3}\langle\theta\rangle_{\mathcal{D}}^2 \ , \tag{5.24}$$

whereby some terms have been rearranged. It turns out that both terms on the right in brackets can be rewritten as a total derivative (Mattsson & Mattsson 2010). First we rewrite the expansion scalar

$$\theta = 2\frac{\dot{r}}{r} + \frac{d\dot{r}}{dr} = \frac{1}{r^2 r'}\frac{\partial}{\partial r_i}\left(\dot{r}r^2\right) \ , \tag{5.25}$$

with $r' = \partial r/\partial r_i$. Second, we rewrite the shear scalar with the squared expansion scalar

$$\frac{2}{3}\theta^2 - \sigma^2 = 2\frac{\dot{r}^2}{r^2} + 4\frac{\dot{r}}{r}\frac{d\dot{r}}{dr} = \frac{1}{r^2 r'}\frac{\partial}{\partial r_i}\left(\dot{r}^2 r\right) \ . \tag{5.26}$$

We already see that the terms are divided by a factor $r^2 r'$ which is also seen in the volume element $dV = 4\pi r^2 r' \left(1 - k(r_i)\right)^{-1/2} dr_i$. This results in the following expression for the integral of the expansion scalar

$$\frac{2}{3}\langle\theta\rangle^2 = \frac{2}{3}\left(\frac{1}{V_{\mathcal{D}}}\int_{V_{\mathcal{D}}} dV\ \theta\right)^2 \overset{k=0}{=} \frac{2}{3}\left(3\frac{\dot{r}}{r}\right)^2 = 6\frac{\dot{r}^2}{r^2} \ , \tag{5.27}$$

where the last two steps are only valid in the case of zero curvature, flat space. For the shear and squared expansion we find

$$\left\langle\frac{2}{3}\theta^2 - \sigma^2\right\rangle = \frac{1}{V_{\mathcal{D}}}\int_{V_{\mathcal{D}}} dV\left(\frac{2}{3}\theta^2 - \sigma^2\right) \overset{k=0}{=} 3\frac{2\dot{r}^2 r}{r^3} = 6\frac{\dot{r}^2}{r^2} \ . \tag{5.28}$$

Again, the last two steps can only be done in flat space. The total backreaction is the difference of these terms, so for flat space we find $\mathcal{Q}_\mathcal{D} = 0$:

$$\text{Flat space} \Rightarrow \text{No backreaction} \tag{5.29}$$

This was already pointed out by Buchert in his first article on averaging Newtonian cosmologies (Buchert & Ehlers 1997), in which he showed that the backreaction can be reduced to the integral over a divergence. This reduces to an integral over the surface by using Gauss's theorem. For cases where space is compact, such as N-body simulations with periodic boundary conditions, this must lead to zero backreaction at the boundaries. The general picture is therefore that for Newtonian cosmologies, and any effect that would be observed on scales smaller than the boundary is due to cosmic variance. This limits the usefulness of the Buchert formalism, as we can apparently not reproduce its effect in the limiting Newtonian case. Also notice that there is no backreaction in FRW cosmologies as there are no inhomogeneities.

In the relativistic non-flat case backreaction can exist. The reason is that the curvature of space changes the volume element so that the backreaction is not zero anymore. In that case we can look at the integrability condition, as it relates the average curvature to the backreaction. If no backreaction is present, the expansion is behaves as a local FRW universe. In that case, the integrability condition implies that the average curvature 'conspires' to go exactly as a^{-2}, as we would expect for a statistically FRW universe.

5.3 Application to the model

In this section we will shortly discuss the approach that we tried to follow. Our main question is whether the backreaction might lead to an apparent acceleration, for an open $\Omega_m = 0.3$, $\Omega_\Lambda = 0$ universe. The best candidate for the study of backreaction are voids. Collapsing structures eventually take negligible volume, while voids provide the universe with large volumes of faster than average expansion. This exploration has focused on the deceleration parameter, because the chosen background universe is decelerating. If backreaction is strong, then it might cause an acceleration which we can measure. To find out we computed the backreaction $\mathcal{Q}_\mathcal{D}$ and the matter density $\langle\rho\rangle_\mathcal{D}$ to find the deceleration parameter $q_\mathcal{D}$ (See Nambu & Tanimoto 2005)

$$q_\mathcal{D} \equiv -\frac{\ddot{a}_\mathcal{D} a_\mathcal{D}}{\dot{a}_\mathcal{D}^2} = -\frac{1}{H_\mathcal{D}^2}\left(-\frac{4\pi G\langle\rho\rangle_\mathcal{D}}{3} + \frac{\mathcal{Q}_\mathcal{D}}{3}\right) = \frac{1}{2}\Omega_{\mathcal{D},m} - \Omega_{\mathcal{D},\mathcal{Q}} \ , \tag{5.30}$$

where we defined

$$\Omega_{\mathcal{D},m} \equiv -\frac{4\pi G\langle\rho\rangle_\mathcal{D}}{3H_\mathcal{D}^2} \ , \qquad \Omega_{\mathcal{D},\mathcal{Q}} \equiv \frac{\mathcal{Q}_\mathcal{D}}{3H_\mathcal{D}^2} \ . \tag{5.31}$$

The evolution of the density can be derived using mass conservation in the shell, so that $\rho r^2 dr = \rho_i r_i^2 dr_i$. This can be rewritten as

$$\rho(r_i, t) = \frac{\rho_i(r_i) r_i^2}{r(r_i,t)^2 r'(r_i,t)} \ . \tag{5.32}$$

The average of the density then becomes

$$\frac{4\pi G \langle \rho \rangle_{\mathcal{D}}}{3} = \frac{1}{2} H_i^2 \Omega_{m,i} \frac{1}{V_{\mathcal{D}(t)}} \int \frac{(1 + \delta_i(r_i)) r_i^2 dr_i}{\sqrt{1 - k(r_i)}} \ . \tag{5.33}$$

We can simplify the integral even more to get

$$\frac{4\pi G \langle \rho \rangle_{\mathcal{D}}}{3} = \frac{1}{2} H_i^2 \Omega_{m,i} \left(\frac{a_{\mathcal{D}(t_i)}}{a_{\mathcal{D}(t)}} \right)^3 \left(1 + \langle \delta_i \rangle_{\mathcal{D}(t_i)} \right) \ . \tag{5.34}$$

Notice that the actual density that we used as input does not exactly correspond to the observed density profile, because the curvature enters once again. Without backreaction this equation becomes exactly the result that we obtained for the spherical model. To make an explicit comparison with the background universe we need the deceleration parameter for the universe

$$q_u \equiv -\frac{\ddot{a}a}{\dot{a}^2} = \frac{\Omega_m}{2} \tag{5.35}$$

We will generally use the ratio $q_{\mathcal{D}}/q_u$ as an observable because the actual value of q might be less interesting. If backreaction is important and causes enough acceleration, then this ratio should become negative.

5.4 Minor computational issues with spherical models

The effect of backreaction can be small or even zero. When using the spherical model with a limited number of shells (250-500), discretization errors appear when averaging using a trapezoid rule. This was discovered by looking at the flat case, in which the backreaction will vanish, which did not completely. The problem arises mainly because the shear and the variance in the expansion can be large, while the backreaction is small.

The solution to this problem is to use a spline and then integrate over the shells when averaging. Splines are piecewise polynomials built from the data points with continuous first derivatives. It turns out that with a limited amount of points, numerical differentiation or integration of a spline from these data points gives much better results. This can be understood because the spline is simply a polynomial that can be analytically integrated or differentiated.

The velocity derivative dv/dr, necessary to compute the velocity divergence, can be explicitly written down and found by perturbing the solution (i.e. going to initial conditions at $r_i + \epsilon$). This gradient should in theory be reasonably close to the real gradient, but analysis showed some inconsistencies. An alternative is simply to take the derivative of v to r, again using the spline derivative. The overall result of both applications of the splines was that the backreaction did indeed vanish for flat space. Even with small numbers of shells the null-result can be obtained.

We now have obtained the necessary steps in order to apply backreaction to a void and to see if backreaction does have the magnitude and effect that we aim for. In the next chapters we will see how to make density profiles for the spherical model and how to gather them in a cosmic Swiss cheese.

6 Making density profiles

In this section I will try to explain how to generate a typical radial density profile for a void or peak using Gaussian random fields. We can use them as initial conditions in the early universe ($z = 1000$), so that the linear initial conditions that the field can provide are still reasonably valid. Most of this section relies on the influential paper on Gaussian random fields by Bardeen, Bond, Kaiser and Salazay (Bardeen et al. 1986).

6.1 Gaussian Random Fields

The seeds for structure formation are thought to be quantum noise that was blown up to cosmic scales by inflation (Guth 1981; Linde 1982; Starobinsky 1982). If this is indeed true then the fluctuations can be described by a Gaussian random field. This means that every set of points from whatever locations in such a field results in a density drawn from a multivariate Gaussian distribution. But even if the distribution for a point is not Gaussian, then still the joint distribution may converge to a Gaussian by means of the central limit theorem.

For the cosmological random field we have a field of *linear* perturbations δ_L. In the linear case, perturbations range from $-\infty$ to $+\infty$, resulting in a distribution with mean zero. This will greatly simplify the following steps. In the case that we draw n values of δ (labelled δ_i) at positions x_i in the field, the probability to find the value of δ in the range $(\delta_i,\, \delta_i + d\delta_i)$ is

$$P(\delta_1, \ldots, \delta_n) d\delta_1 \ldots d\delta_n = \frac{1}{\sqrt{(2\pi)^n |M|}} \exp\left(- \sum_{i,j} \delta_i \, (M^{-1})_{ij} \, \delta_j \right) d\delta_1 \ldots d\delta_n \; . \tag{6.1}$$

The matrix M_{ij} is the covariance matrix, which tells us how much two points are correlated. For a scalar Gaussian random field, this covariance matrix is just the two-point correlation function $\xi(\vec{r_1}, \vec{r_2}) = \langle \delta(\vec{r_1}) \delta(\vec{r_2}) \rangle$. The covariance matrix ensures that we get continuous noise because when we move to smaller scale, the noise becomes ever more strongly correlated (i.e. the variance drops). Integration or differentiation of random fields is not always possible (it is for Gaussian fields), but this can be overcome by introducing filtering on the smallest scales. Another property is that any function, differentiation or integration of the Gaussian random field itself is again a Gaussian random field.

The Gaussian field that we consider here is strictly homogeneous and isotropic, this means that the correlation function depends only on the distance between two points $\xi(\vec{r_1}, \vec{r_2}) = \xi(|r_1 - r_2|)$. It is often very convenient to move to Fourier space, where we can define the correlation function as the Fourier transform of the power spectrum. In Fourier space, we can find the density and correlation function as

$$\delta(\vec{r}) = \frac{1}{(2\pi)^3} \int d^3k \delta(\vec{k}) e^{i\vec{k}\cdot\vec{r}} \ , \tag{6.2}$$

$$\left\langle \delta(\vec{k})\delta^*(\vec{k}') \right\rangle = (2\pi)^3 P(\vec{k}) \delta_D(\vec{k} - \vec{k}\,') \ . \tag{6.3}$$

The power spectrum is the amount of power in the field at some Fourier mode $\vec{k}$. The correlation function then becomes

$$\xi(\vec{r}) = \int \frac{d^3k}{(2\pi)^3} P(\vec{k}) e^{i\vec{k}\cdot\vec{r}} \ , \tag{6.4}$$

so that the whole Gaussian random field is effectively fixed by choosing the power spectrum. We can simplify the equations even more, because the field is strictly homogeneous. Therefore we can replace the product $\vec{k} \cdot \vec{r}$ in the transform by $kr\cos(\theta)$ and integrate over angles ϕ and θ to get

$$\xi(r) = \int_0^\infty \frac{dkk^2}{4\pi^2} P(k) \int_{-\pi/2}^{+\pi/2} d\theta \sin\theta e^{ikr\cos\theta} = \int \frac{dkk^2}{2\pi^2} \operatorname{sinc}(kr) P(k) \tag{6.5}$$

An important tool in analysing the random field is a filter which removes fluctuations smaller than the filter scale. The two most commonly used filters are the Gaussian filter, which convolves the field with a Gaussian (see figure 6.1), and the top hat filter, which convolves the field with a multidimensional step function. For a Gaussian filter on a field $\delta(\vec{k})$ smoothed on scale R_G the resulting operation looks like

$$\delta(\vec{r}|R_G) = \int \exp\left(-\frac{|\vec{r} - \vec{r}'|^2}{2R_G^2}\right) \delta(\vec{r}') \frac{d^3r'}{(2\pi R_f)^{3/2}} \ . \tag{6.6}$$

In Fourier space, a convolution is a multiplication with the Fourier transform $W_G(k)$ of the Gaussian filter, which is again a Gaussian. The resulting filter $W_G(k)$, the field $\delta(k|R_G)$ and the power spectrum $P(k|R_G)$ are then given by

$$W_G(x) = \exp\left(-x^2/2\right) \ , \tag{6.7}$$

$$\delta(k|R_G) = W_G(kR_G) F(k) \ , \tag{6.8}$$

$$P(k|R_G) = W_G^2(kR_G) P(k) \ , \tag{6.9}$$

where the power spectrum is filtered with the square of the filter as it is proportional to the square of the field $\delta(k|R_G)$. The top hat filter is given by (Bardeen et al. 1986)

$$\delta(\vec{r}|R_{TH}) = \int \theta\left(1 - \frac{|\vec{r} - \vec{r}'|}{R_{TH}}\right)\delta(\vec{r}')\frac{d^3r'}{\frac{4}{3}\pi R_{TH}^3} \ . \tag{6.10}$$

The filter W_{TH}, field $\delta(k|R_{TH})$ and power spectrum $P(k|R_{TH})$ are given by

$$W_{TH}(x) = \frac{3(\sin x - x\cos x)}{x^3} = \frac{3}{x}\frac{d\,(\mathrm{sinc}(x))}{dx} \ , \tag{6.11}$$

$$\delta(k|R_{TH}) = W_{TH}(kR_{TH})F(k) \ , \tag{6.12}$$

$$P(k|R_{TH}) = W_{TH}^2(kR_{TH})P(k) \ . \tag{6.13}$$

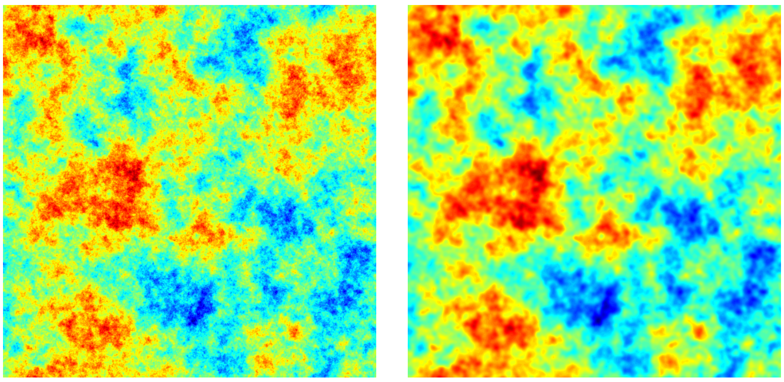

Figure 6.1: 2D realisation of a Gaussian random field on a 1024x1024 pixel box. The left image shows the full unfiltered field, while the right image has been smoothed with a Gaussian on a scale of 4 pixels. Image created using a Matlab code by Jakob van Bethlehem. The effect of the filter is to remove the small scale fluctuations in the field, while the Gaussian filter also strongly smooths the field.

In Fourier space, the top hat filter gives rise to ringing effects, which can be seen from the Fourier transform of the filter W_{TH}. The filter contains the derivative of a sinc function, which causes oscillations to many times the cut-off scale in Fourier space. An important difference between the filters is the amount of mass they enclose within their filter radius. For the top hat and Gaussian filters they are respectively

$$V_{TH} = \frac{4\pi}{3}R_{TH}^3 \ , \tag{6.14}$$

$$V_G = (2\pi)^{3/2}R_G^3 \ . \tag{6.15}$$

Most often one is interested in a certain volume or mass, meaning that the filter scale should be derived from the demanded volume depending on the filter that is being used.

The main difference between both filters is that the Gaussian filter balances smoothing and filtering, while the top hat filter is only used to filter out small fluctuations.

We can also define a set of spectral moments of the power spectrum by weighing with powers of k^2

$$\sigma_j^2 = \int_0^\infty \frac{k^2 dk}{2\pi^2} P(k) k^{2j} \ . \tag{6.16}$$

The mean square density fluctuation of the field is then $\sigma_0 = \sqrt{\xi(0)}$. Two other important results are the spectral parameter γ and the (comoving) length parameter R_*

$$\gamma \equiv \frac{\sigma_1^2}{\sigma_2 \sigma_0} \ , \tag{6.17}$$

$$R_* \equiv \sqrt{3} \frac{\sigma_1}{\sigma_2} \ . \tag{6.18}$$

What we omitted so far is that the field evolves with time, but because we are in the linear regime, it evolves self-similarly as in linear theory. This means that the field evolves as $\delta(k,t) \equiv \frac{D(t)}{D(t_0)} \delta(k, t_0)$ and the power spectrum as $P(k,t) \equiv \left(\frac{D(t)}{D(t_0)}\right)^2 P(k, t_0)$. The spectral parameters γ and R_* are therefore invariant under time translations.

6.2 Power spectrum

The most important ingredient for the random field is the power spectrum. It consists of two separate elements, the primordial power spectrum $P_{\rm prim}(k)$, usually assumed a power law with index n, and the transfer function $T(k)$. The primordial power spectrum describes how the pure primordial power spectrum looked just after the Big Bang. The transfer function describes the evolution of the resulting fluctuations until the moment of last scattering, when the fluctuations were frozen in. The total power spectrum is then given by

$$P(k) = T(k)^2 P_{\rm prim} = T(k)^2 A k^n \ , \tag{6.19}$$

with A the normalisation of the power spectrum. The normalisation is most often arranged by demanding that the value of σ_0 is fixed at a filter scale of R_8 =8 Mpc h^{-1}

$$A = \frac{\sigma_8^2}{\sigma_0^2(R_8)} \ . \tag{6.20}$$

Typically, σ_8 ranges between 0.8 and 0.9, with 0.8 generally being the most accepted result from the CMB and galaxy clustering (see e.g. Komatsu et al. 2011).
Typical combinations of transfer functions and primordial spectra are the Zel'dovich spectrum ($n = 1$) with adiabatic cold dark matter (CDM) fluctuations, and isocurvature CDM

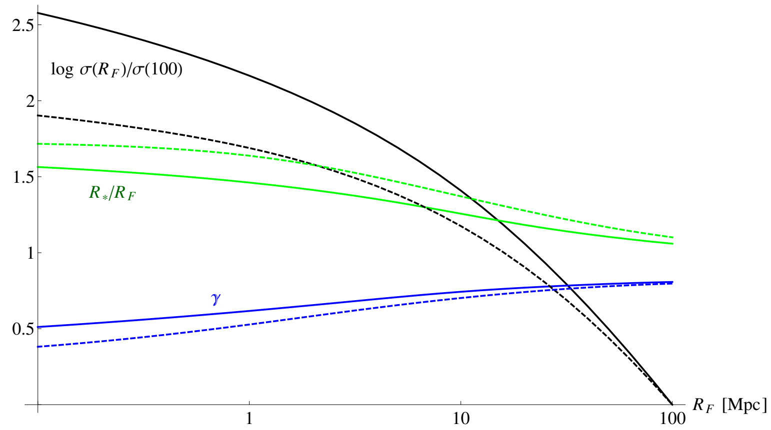

Figure 6.2: Spectral parameters for adiabatic Zel'dovich power spectrum (solid line) and isothermal flicker spectrum (dotted line) as a function of Gaussian filtering scale R_G. In this specific plot we used $\Omega_D M = 1$ and $h = 0.5$. We can see that the adiabatic Zel'dovich spectrum has less power at larger scales, and more at smaller scales. The parameters γ and R_* relate to the 0th, 1st and 2nd moments of the power spectrum.

fluctuations with a flicker spectrum ($n = -3$) (see figure 6.2). The transfer function in the case of adiabatic CDM fluctuations is given by (Bardeen et al. 1986)

$$T_{\mathrm{CDM,ad,DM}}(k) = \frac{\log(1+2.34q)}{2.34q}\left(1+3.89q+(16.1q)^2+(5.46q)^3+(6.71q)^4\right)^{-1/4}, \quad (6.21)$$

$$q \equiv \frac{k}{\Omega_{\mathrm{DM}} h^2 \mathrm{Mpc}^{-1}}, \quad (6.22)$$

with Ω_{DM} the density parameter for dark matter. Adiabatic dark matter fluctuations are those for which the fluctuations in the photon and dark matter components in the universe are equal. The transfer function for isocurvature fluctuations is given by

$$T_{\mathrm{CDM,isoc,DM}} = (5.6q)^2 \left[1 + \frac{(40q)^2}{1+215q+(16q)^2(1+0.5q)^{-1}} + (5.6q)^{8/5}\right]. \quad (6.23)$$

In this case the fluctuations of photons and dark matter are counter correlated so that the total energy perturbation is zero.

The specific combinations of the transfer function and the initial power spectrum are restricted because of the $k \to \infty$ behaviour of $P(k)$. If too much power remains at high k then the resulting matter distribution would not reach a scale of homogeneity, which would contradict our observations. The CMB is our best probe of the initial random field, though the large scale structure should have preserved also some of the initial field (see e.g. Eisenstein et al. 2005). Observations on the CMB indicate that the isocurvature scenario is very unlikely, but the adiabatic scenario is much favoured by the data. The primordial power spectrum appears close to $n = 1$, though not exactly a Zel'dovich primordial spectrum (see the results in Komatsu et al. 2011 and a discussion in Pandolfi et al. 2010).

6.3 A typical profile

We will now continue with obtaining a general profile using Gaussian random fields. The essential idea is to take the correlation function near a peak (local maximum) and do a Taylor expansion. Because the field is symmetric in δ we do not need to treat voids or peaks seperately. We first define two parameters, the peak (or void) height ν and the peak curvature x,

$$\nu \equiv \frac{\delta}{\sigma_0} \ , \tag{6.24}$$

$$x \equiv -\nabla^2\delta/\sigma_2 \ , \tag{6.25}$$

with both times $\delta(r)$ evaluated at $r = 0$. With high curvature, peaks are generally located in a void, while voids are surrounded by a wall. In the case of low curvature, voids and peaks are directly embedded in the background. The condition that we are located in a maximum of the Gaussian field means that the first derivative of the field is zero. Near a peak, the Taylor expansion then only depends on the second (vector) derivative, which is contained in the curvature x. Around a peak of height ν and curvature x we then find

$$\delta(r,\theta,\phi|\nu,x) = \nu\sigma_0 - x\sigma_2\frac{r^2}{2}\left[1 + A(\theta,\phi|e,p)\right] \ , \tag{6.26}$$

with e and p the ellipticity and oblateness respectively, and $A(\theta,\phi|e,p)$ a function describing the anisotropy of the peak. In the general case, this results in pancake shaped blobs (see figure 6.3), as in the Zel'dovich formalism (Zel'Dovich 1970). The anisotropy function $A(\theta,\phi|e,p)$ vanishes if averaged over all angles, so that we can use this procedure to eventually find the most general radial profile.

To find the average constrained profile one needs to perform an average over the field (appendix D in Bardeen et al. (1986)). What results is the most typical peak in a gaussian random field, given the constrains,

$$\frac{\langle\delta(r,\theta,\phi|e,p,x,\nu)\rangle}{\sigma_0} = \left(\frac{\nu-\gamma\nu}{1-\gamma^2}\right)\Psi(r) + \left(\frac{\nu-x/\gamma}{1-\gamma^2}\right)\frac{R_*^2}{3}\nabla^2\Psi(r) + B(r)A(\theta,\phi|e,p) \ , \tag{6.27}$$

with $\Psi(r) \equiv \frac{\xi(r)}{\xi(0)} = \frac{\xi(r)}{\sigma_0^2}$ and $B(r)$ a function that is only relevant when considering anisotropic profiles. For voids one can take the same profile with $\nu = |\nu|$ and negated density. The second derivative $\nabla^2\Psi(r)$ can be solved by using the spherical Laplacian on the sinc function under the integral, which carries all information on r,

$$\nabla^2\mathrm{sinc}(kr) = \frac{1}{r^2}\frac{\partial}{\partial r}r^2\frac{\partial}{\partial r}\mathrm{sinc}(kr) = -k^2\mathrm{sinc}(kr) \ . \tag{6.28}$$

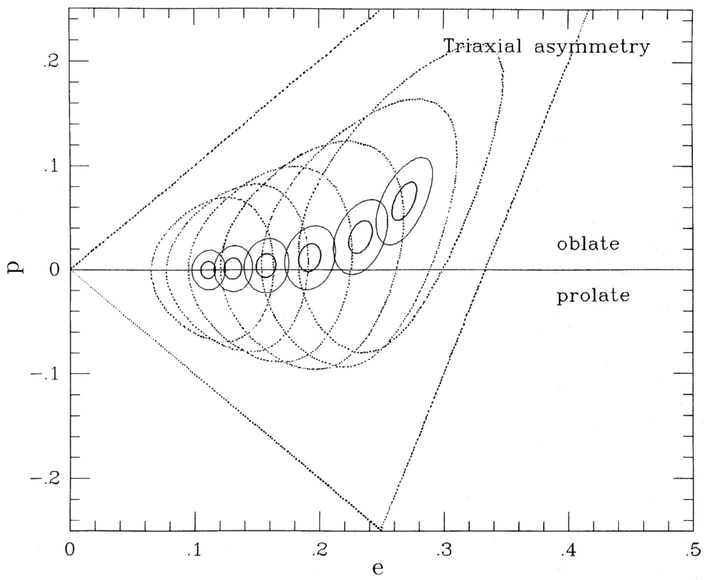

Figure 6.3: Contours for 95%, 90% and 50% of the ellipticity-oblateness distribution for peaks of height $\nu = 1 \ldots 6$ (from right to left). The triangle shows the area containing valid values of e and p. This image clearly shows that peaks are inherently asymmetric, though as the height increases, the peaks tend to be more spherically symmetric.

Typical values for the curvature can be found from the mean of the distribution $P(x|\nu)$

$$\langle x|\nu\rangle = \gamma\nu + \Theta(\gamma,\nu) \ , \tag{6.29}$$

$$\Theta(\gamma,\nu) = \frac{3(1-\gamma^2) + (1.216 - 0.9\gamma^4)\exp\left[-\gamma/2(\gamma\nu/2)^2\right]}{\sqrt{3(1-\gamma^2) + 0.45 + (\gamma\nu/2)^2} + \gamma\nu/2} \ . \tag{6.30}$$

The effect of curvature depends on the typical size of the void. For small and shallow voids, the effect is generally larger. Figure 6.5 and 6.4 show some realisations of a profile. The final step in generating an initial profile is to place it at $z = 1000$ using the linear growth theory

$$\delta(r_i, t_i) = \frac{D(t_i)}{D(t_0)}\delta(r_i) \ , \tag{6.31}$$

with $r_i = a_i r$.

We have obtained a framework that can be used to create density profiles to model a void. We can also use toy models which show some characteristics of the spherical models. Examples are the top hat void, which quickly goes towards shell-crossing, or the smoother 'tanh' void, which shows the same behaviour but slightly smoothed. The derived profiles are very smooth and reach shell-crossing very slowly.

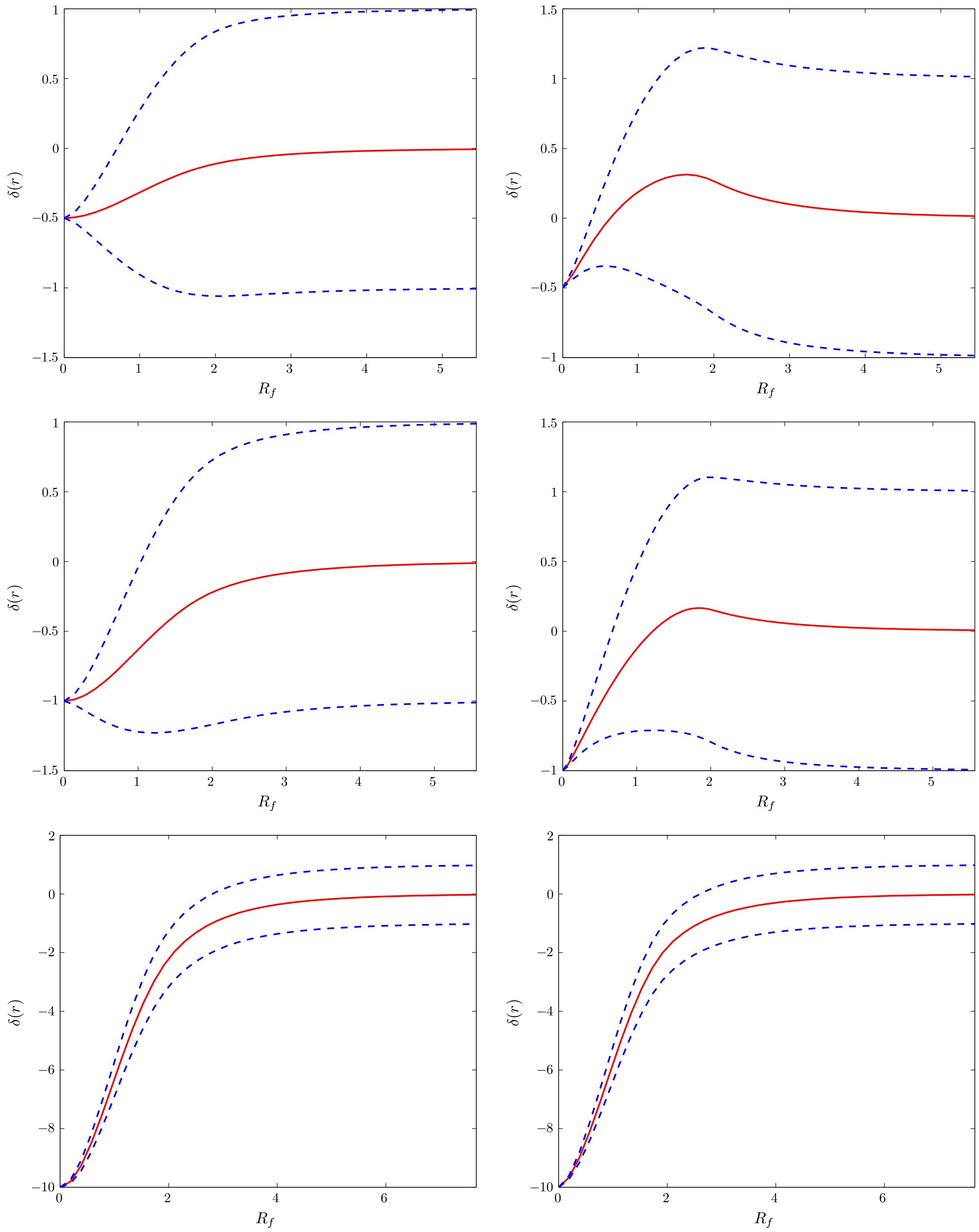

Figure 6.4: Void profiles with and without curvature (left: $x = 0$; right: $x = 4\langle x \rangle$) for the case $R_{TH} = 3$, $\delta = -0.5, 1, 10$ (from top to bottom respectively). The power spectrum used is the Zel'dovich primordial spectrum with adiabatic fluctuations, filtered with a top hat. What we can see is that smaller voids (smaller filter radius) are more enhanced by the curvature, while also shallow voids are more enhanced by the curvature.

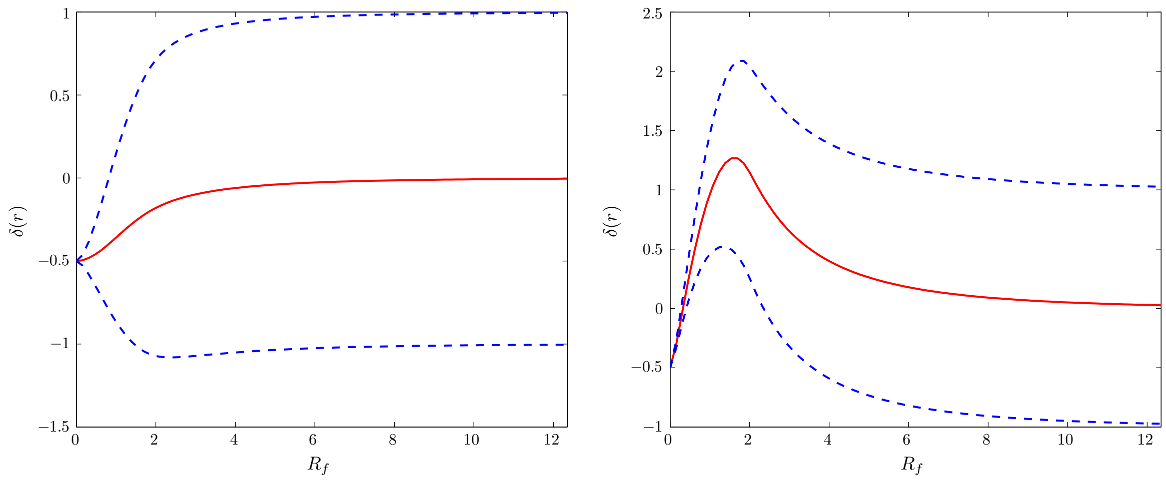

Figure 6.5: Void profiles with and without curvature (left: $x = 0$; right: $x = 4\langle x\rangle$) for the case $R_{TH} = 1$. The curvature makes the void steeper, while also creating an overdense ridge around the void. The power spectrum used the Zel'dovich primordial spectrum with adiabatic fluctuations, filtered with a top hat.

7 Making Cheese: Mass-distribution functions

In this section we will explore the size-distribution functions for cosmic structures. The reason for this is that we want to make a realistic 'cheese' in which the voids are distributed as they would be in the universe. In this way, the results allow a better comparison of the results with observations. Our goal is to obtain a suitable distribution of void sizes, though most of the work in this field has focused on halo mass distributions. This may at first be confusing, but eventually we will switch to void distributions, as both distributions are intricately related.

7.1 Press-Schechter formalism

One of the most important probes of cosmology is the distribution of matter on large scales. The first structures in the universe are thought to be the Gaussian density fluctuations, just after the last scattering of the CMB photons. Over time, gravity caused overdense regions to attract more matter, until eventually the first tiny clouds started collapsing by gravitational instability. From these clouds, the first stars are thought to have formed. As the universe evolved, larger and larger structures started to form, starting with galaxies, then clusters and eventually the cosmic web. This is the so-called bottom-up hierarchical formation scenario, which tells us that overdensities on small scales already entered the phase of non-linear collapse quite early in the universe, while the large scale structures of today are still in the (quasi-) linear phase. In the linear phase, the fluctuations simply scale up as the universe expands, while in the non-linear phase, the fluctuations uncouple from the universe and collapse. Little information on the initial perturbations is therefore retained on small scales. But on Megaparsec scales, the structures are expected to be still an excellent probe of the initial density field.

The Press-Schechter formalism relates the distribution of the large scale structures to the initial random field (Press & Schechter 1974). To find how masses are distributed, we simply need to look how the structures that have collapsed at some time are distributed with mass. First of all, the distribution of (linear) density fluctuations δ on some mass scale m is approximately a Gaussian distribution

$$p(m,\delta)d\delta = d\delta \frac{1}{\sqrt{2\pi}\sigma(m)} \exp\left(-\frac{2\delta^2}{\sigma^2(m)}\right) , \tag{7.1}$$

with $\sigma(m)$ the variance of δ. This of course only holds if the δ and m are such that we are above the non-linear scale. For the Press-Schechter formalism we resort to the top-hat window for the power spectrum, so that the mass m is defined as the simple top-hat mass $M_{TH} = \frac{4}{3}\pi\rho_u R^3$. The variance $\sigma(m)$ is clearly very important since it directly connects to the primordial power spectrum, determining the evolution of structure. In the scenario of hierarchical structure formation, the largest fluctuations (large $\sigma(m)$) occur on the smallest scales, while the smaller fluctuations (smaller $\sigma(m)$) occur on larger scales as the background universe is approached. The order in which structure evolves in the universe is therefore completely contained in the variance $\sigma(m)$.

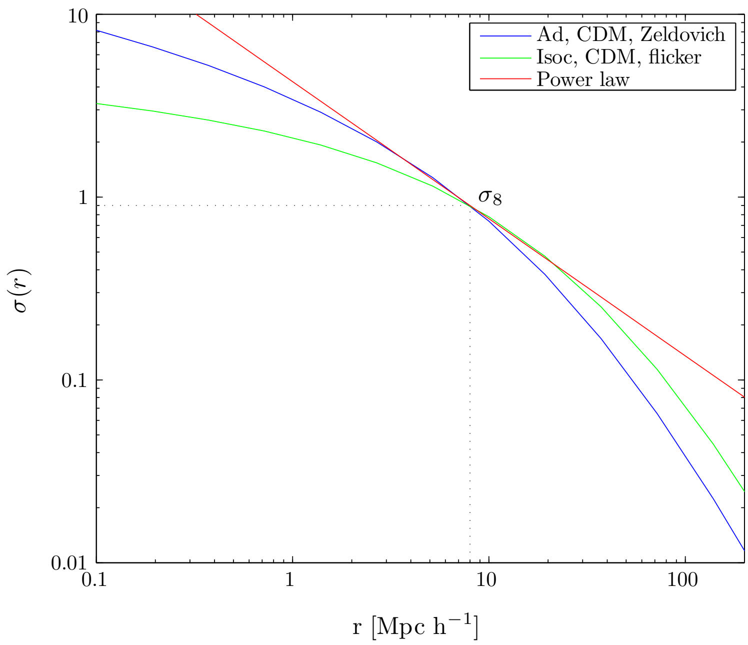

Figure 7.1: An example of $\sigma(m)$ in a hierarchical structure formation scenario. In this case σ was plotted for the Zel'dovich primordial power spectrum with adiabatic CDM fluctuations, for the flicker spectrum with isocurvature fluctuations and for a power law ($n = -2.5$) (see Bardeen et al. 1986, section A).

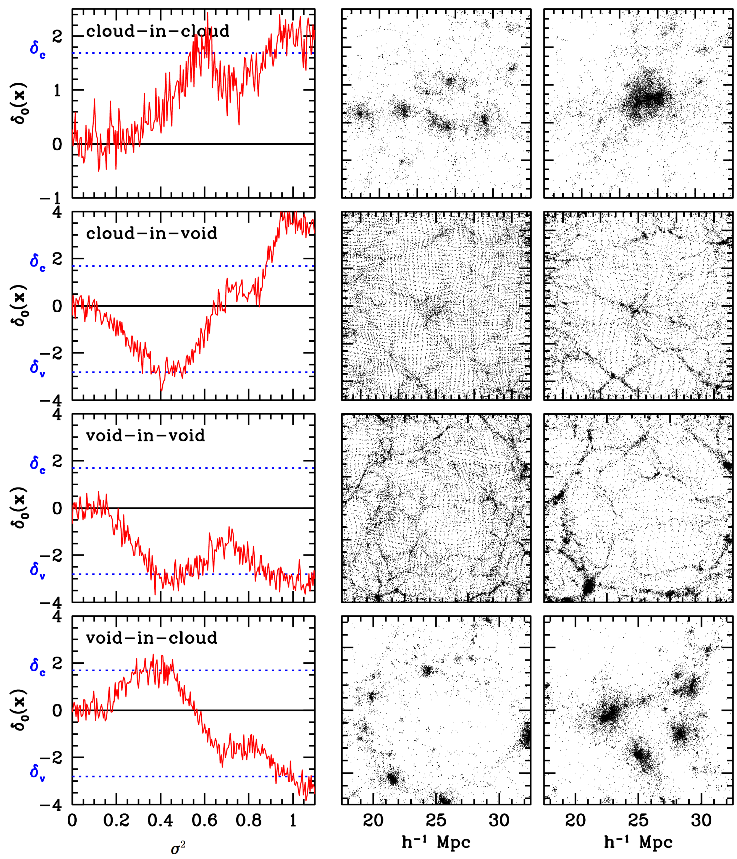

Figure 7.2: An overview of the void sociology with random walks and N-body simulations. On the left-hand side we see the random walks, while on the right-hand side we see how the associated particle distribution evolves from initial times (left frame) to later times (right frame). In the case of voids we are facing a two-barrier problem where we have to be aware of double counting, both with the void-in-void and the void-in-cloud situations. For the cloud-in-cloud situation, we eventually end up with only one cloud, while the void-in-cloud simply vanishes as the larger scale cloud collapses. Adapted from Weygaert & Sheth 2004.

To find the average fraction of collapsed structures, we look at the densities where the $\sigma(m) \to \delta_c = 1.69$ border has been crossed. One thing to notice here is that the linear theory predicts these quantities to evolve as $\sigma(z) = D(z)\sigma(z=0)$ and $\delta_c(z) = D(z)\delta_c(z=0)$. This implicates that even at different redshifts, the same border has to be crossed, so that the fraction of collapsed objects is found to be

$$F(m) = \int_{\delta_c(z)}^{\infty} p(m,\delta)d\delta = \frac{1}{2}\mathrm{erfc}\left(\frac{\delta_c}{\sqrt{2}\sigma(m)}\right) . \tag{7.2}$$

However, we see that even as $\sigma \to \infty$ that the collapsed fraction is still $1/2$ because only the overdense regions contribute to the collapse. This therefore completely ignores that underdense regions can be contained in larger overdense regions which will eventually collapse and remove the underdensities. Press and Schechter resolved this by introducing an ad hoc factor of 2, making the collapse indeed complete. A more rigorous explanation using the Extended Press-Schechter formalism will be given later on.

From the average fraction of collapsed objects $F(m)$ we can try to find the differential fraction of collapsed objects $f(m)dm$. We achieve this by taking the derivative to mass scale m

$$f(m) = \frac{dF}{dm} = \frac{dF}{d\sigma}\frac{d\sigma}{dm} = \sqrt{\frac{2}{\pi}}\frac{1}{m}\frac{\delta_c}{\sigma}\left|\frac{d\ln\sigma}{d\ln m}\right| \exp\left[-\frac{\delta_c^2}{2\sigma^2}\right] . \tag{7.3}$$

The differential number density $n(m)dm$ is found by multiplying the differential fraction $f(m)$ by the number density of a region of mass scale m. The effective number density for a region is related to the volume of the region v as $1/v = \rho_u/m$, which results in

$$n(m) = \sqrt{\frac{2}{\pi}}\frac{\rho_u}{m^2}\frac{\delta_c}{\sigma}\left|\frac{d\ln\sigma}{d\ln m}\right| \exp\left[-\frac{\delta_c^2}{2\sigma^2}\right] . \tag{7.4}$$

We can also make the behaviour of f more clear without explicitly calculating σ, by looking at $f(\nu)$ with $\nu = \delta_c/\sigma$. To do this we use the invariance of the distribution under coordinate transformations, $f(\nu)d\nu = f(m)dm$, so that the distribution is given by

$$f(\nu) = \sqrt{\frac{2}{\pi}}\exp\left(-\frac{\nu^2}{2}\right) . \tag{7.5}$$

The resulting distribution has a strong cut-off at $\nu > 1$, while at low ν it behaves as $\nu^{-1/2}$.

7.2 Extended Press-Schechter formalism

The extended Press-Schechter formalism or excursion set formalism couples the primordial Gaussian random field to a Brownian random walk. The main idea is that for a given point in a random field, one can see the trajectory of δ through the different scales σ^2 as a random walk, with σ^2 acting as a time coordinate. The walk starts at the largest scale with $\delta = 0$, representing the homogeneous universe. It then moves to smaller scales (larger σ) until it has a first up-crossing to the $\delta_c = 1.69$ barrier, at which moment we count everything within this scale to be part of the collapsed object. Therefore, the border can be crossed many times, but these crossings correspond to again smaller structures, which will all collapse in the largest structure (the so-called cloud-in-cloud situation).

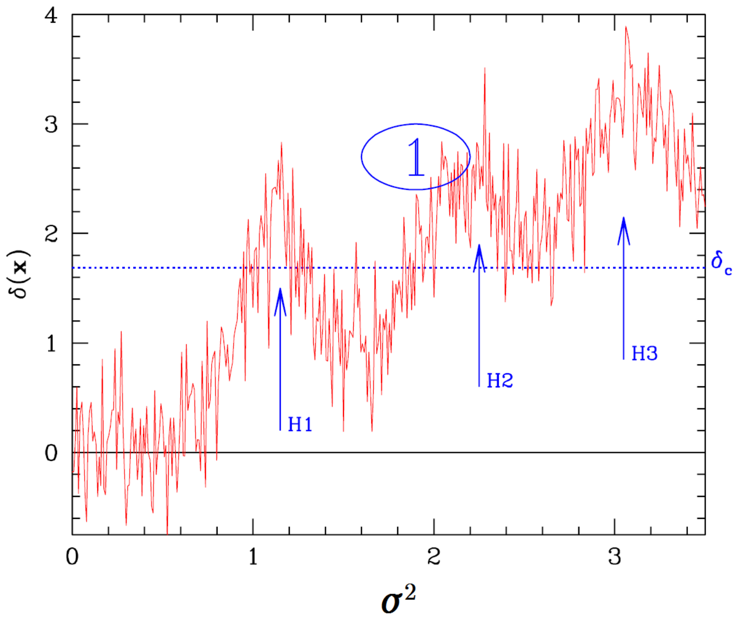

Figure 7.3: Example of a random walk of the linear density perturbation δ as a function of scale, parametrized by σ^2. The largest scale (smallest σ^2) at which δ crosses the barrier estimates the mass of the halo which will form around this region. Adapted from Sheth & Van de Weygaert 2004B

The tophat filter is very convenient in the Extended Press-Schechter formalism, because moving from scale σ^2 to scale $\sigma^2 + d\sigma^2$ means adding a small amount of extra k-space to the walk. This means that only a Gaussian variate with variance $d\sigma^2$ has to be added, without the need to consider what the history of the path was (also known as a Markov process). With other filters we would need to consider the whole history, which would make this exercise much more difficult (Bond et al. 1991). What we now obtain is the (continuous) Brownian random walk. For the case of no barrier the distribution of 'position' δ at 'time' σ^2 is again a Gaussian

$$p(\delta, \sigma^2) = \frac{1}{\sqrt{2\pi}\sigma} \exp\left(-\frac{2\delta^2}{\sigma^2}\right) . \tag{7.6}$$

Worth mentioning here is that the method has only a statistical meaning. This is quickly understood by looking at two nearby points in the same structure, which would actually be able to cross the boundary at completely different scales, while in reality they collapse together. Despite this drawback, the excursion set formalism has a much more clear view of collapsed objects by looking at the first crossing distribution. To find the distribution $p(\delta, \sigma^2)$ in the case of a boundary δ_c we need to solve a special case of the Fokker-Planck equation, namely the diffusion equation

$$\frac{dp}{d\sigma^2} = \frac{1}{2} \frac{d^2 p}{d(\sigma^2)^2} \; . \tag{7.7}$$

Using the proper boundary conditions we can find p, but we can also resort to a simpler graphical method as depicted in figure 7.4. Consider a path that has crossed the boundary at some 'time' σ^2. The path afterwards has equal chances to be found above and below the barrier, meaning that a cloud is equally likely to be in a void as in another cloud.

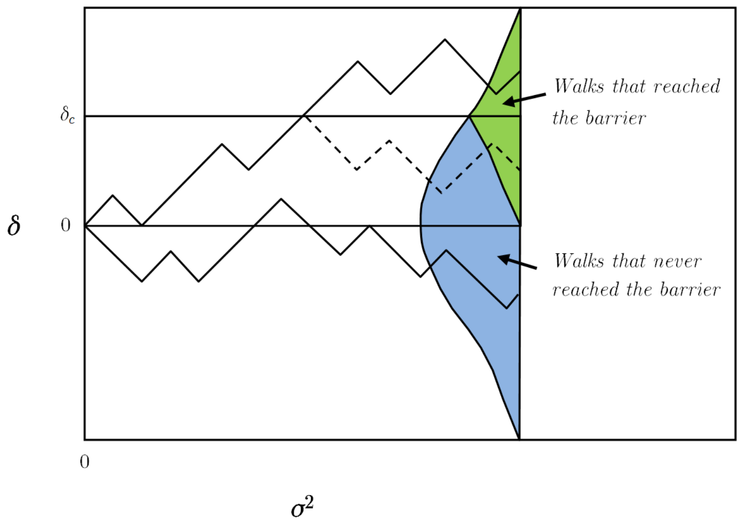

Figure 7.4: Typical random walks of δ at some position r. Without a border, the probability for δ is a Gaussian with variance σ. As we can see, the upper triangle is the result from Press and Schechter, integrating only the tail of the Gaussian. However, for each of these walks, there is an equally likely mirrored path from the point the path touched the barrier. Taking these properly into account resolves the problem of the Press-Schechter formalism in a rigorous way. Adapted from Bond et al. 1991.

As the drawing shows we now have a rigorous way of finding the extra factor of 2. One can now for example look at the total distribution without the reflected paths and integrate up to δ_c to find the fraction that never collapsed, or just read the result from the graph. Taking the former method, the fraction that never collapsed is given by

$$1 - F(M) = \int_{-\infty}^{\delta_c} d\delta \left\{ p(\delta, \sigma^2) - p(2\delta_c - \delta, \sigma^2) \right\} = 1 - \text{erfc}\left(\frac{\delta_c}{\sqrt{2}\sigma} \right) \; , \tag{7.8}$$

so that indeed the factor 2 is obtained without resorting to ad hoc arguments. The distribution is again found by finding the fraction of collapsed objects in the range m, $m + dm$, giving again the same result as in equation 7.4.

7.3 Voids in the Press-Schechter formalism

One might think at first that extending the formalism to voids is straightforward, since one only has to replace the collapse boundary δ_c by the boundary that represents the emergence of a void. Usually one uses the moment of shell-crossing for the spherical model as the boundary, meaning that $\delta_v = -2.81$. For halos we only had to take into account the cloud-in-cloud situation, but voids have another important case, the void-in-cloud situation. When a void is located in a cloud at some larger scale, the void will eventually collapse and vanish. An image depicting the void sociology is given in figure 7.2.

The fraction of excursions F that cross δ_v at σ^2 and that do not cross δ_c until after they have crossed can be found in an analytic form as

$$F(\sigma^2, \delta_c, \delta_v) = \sum_{j=1}^{\infty} \left(\frac{j^2 \pi^2 \mathcal{D}^2}{\delta_v^2} \right) \exp \left(\frac{j^2 \pi^2 \mathcal{D}^2}{\delta_v^2 / \sigma^2} \right) \tag{7.9}$$

where $\mathcal{D} = |\delta_v| / (\delta_c + |\delta_v|)$ parametrizes the impact of the void-in-cloud process (Van de Weygaert & Sheth 2004). In the case the void-in-cloud process can be ignored $\mathcal{D}$ goes to 0, whereas if it is dominant, $\mathcal{D}$ goes to 1. We again require that the general evolution of these parameters is self-similar with the linear growth factor, so that the boundary crossing condition remains valid for different epochs. The distribution function can be rewritten in a more useful and familiar form using $\nu = \delta_c / \sigma(M)$,

$$f(\nu) \approx \sqrt{\frac{2}{\pi}} \exp \left(-\frac{\nu^2}{2} \right) \exp \left(-\frac{|\delta_v|}{\delta_c} \frac{\mathcal{D}^2}{4\nu^2} - 2 \frac{\mathcal{D}^4}{\nu^4} \right) . \tag{7.10}$$

This distribution has a clear peakedness for $D > 0$, but as $D \to 0$ it converges to the usual Press-Schechter formula (see figure 7.5). As the image shows, the void-in-cloud process is mainly important for smaller voids, whereas the largest voids are almost insensitive to the value of $\mathcal{D}$.

The distribution can now be written down in three forms (see for example $n(r)$ in figure 7.6), depending on which parameter should be used for the distribution

$$n(m) = \frac{\rho_u}{m^2} \left| \frac{d \ln \sigma}{d \ln m} \right| \nu f(\nu) \ , \tag{7.11}$$

$$n(v) = \frac{1}{v} \frac{1}{2\sigma^2} \left| \frac{d\sigma^2}{dr} \right| \frac{dr}{dv} \nu f(\nu) \ , \tag{7.12}$$

$$n(r) = \frac{1}{v(r)} \frac{1}{2\sigma^2} \left| \frac{d\sigma^2}{dr} \right| \nu f(\nu) \ . \tag{7.13}$$

Most convenient in this case is the volume distribution, which I will use hereafter.

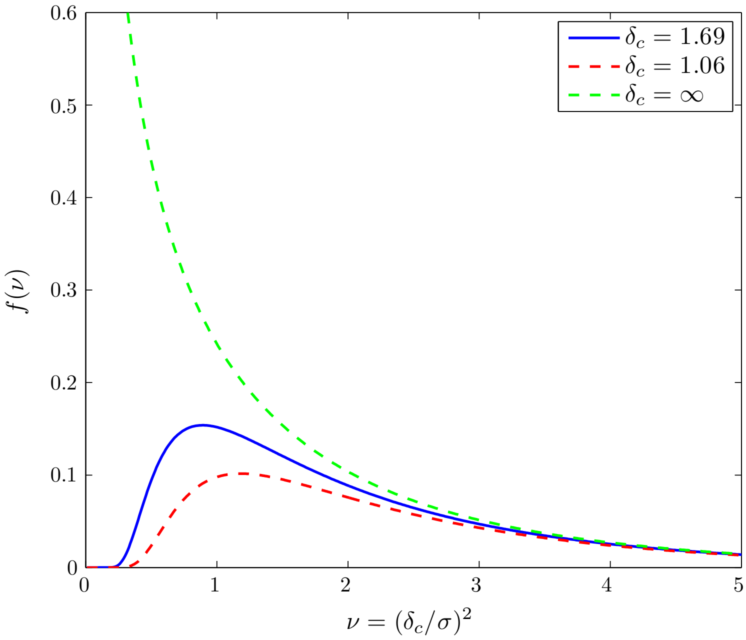

Figure 7.5: The Sheth-Van de Weygaert void fraction $f(\nu)$ plotted for different ratios $\mathcal{D}$ for the void-in-cloud process. The solid curve is for $\delta_v = -2.81$ and $\delta_c = 1.69$. The dashed curve shows $\delta_c = 1.06$ and the dotted curve is for $\mathcal{D} = 0$. From the plot it is clear that the largest voids are not affected by the void-in-cloud process, the effect is peaked around smaller voids.

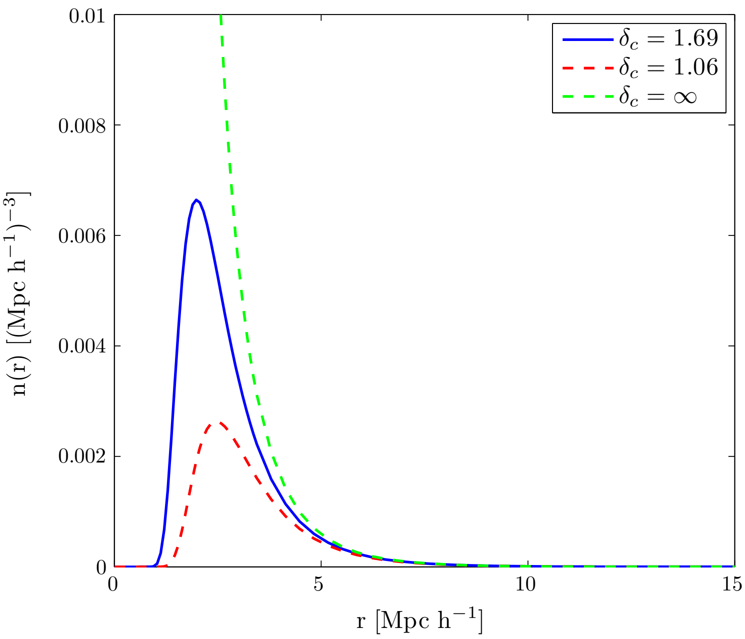

Figure 7.6: The Sheth-Van de Weygaert distribution $n(r)$ plotted for different ratios $\mathcal{D}$ for the void-in-cloud process. The solid curve is for $\delta_v = -2.81$ and $\delta_c = 1.69$. The dashed curve shows $\delta_c = 1.06$ and the dotted curve is for $\mathcal{D} = 0$.

7.4 Sampling the void distribution

For the model we can use the void distribution as given above. But it turns out that the actual void profiles that are generated using the Gaussian random fields are much larger than one would expect from the filter radius R_f. The following relation seems a good approximation for the size of a void with deepness δ and filter scale R_{TH}

$$R_{\max} = 10 + 0.7|\delta| + 4R_{TH} \ . \tag{7.14}$$

From observations of galaxies it was already found that voids are typically much larger than the voids predicted from the Press-Schechter formalism (see e.g. Furlanetto & Piran 2006). This is thought to occur because of observational reasons, but perhaps the discrepancy between filter radius and void size is also a source of this issue. We can now try to fill a volume with these voids to simulate a universe. First of all, the total number of voids in a region (with voids in a range V_{max}, V_{min}) is given by

$$N = V_{box} \int_{V_{min}}^{V_{max}} n(v) dv \ . \tag{7.15}$$

These voids take the following volume fraction

$$V_{voids} = V_{box} \int_{V_{min}}^{V_{max}} n(v) v \, dv = V_{box} \int_{v_{min}}^{v_{max}} f(v) dv \ . \tag{7.16}$$

Simulating 10,000 similar voids is not very convenient, Instead, we try to simulate only a number of voids that are typical of the whole distribution. Say we want to simulate p typical voids and then describe the whole region. We would like to find $V_1 \ldots V_{p-1}$ so that

$$\frac{1}{p} = \frac{V_{box}}{V_{voids}} \int_{V_{i-1}}^{V_i} f(v) dv \ = \frac{\int_{V_{i-1}}^{V_i} f(v) dv}{\int_{V_{min}}^{V_{max}} f(v) dv}, \tag{7.17}$$

with $V_0 = V_{min}$ and $V_p = V_{max}$. This results in p intervals in the void space. The next step is to find the typical volume within this interval, which can be found through a weighted mean with $f(v)$

$$V_{typ,i} = \langle V \rangle_i = \frac{\int_{V_{i-1}}^{V_i} f(v) \, v \, dv}{\int_{V_{i-1}}^{V_i} f(v) \, dv} \ . \tag{7.18}$$

What remains is the multiplicity factor n_i of this void so that the total volume in the interval is conserved. Note here that we use here the actual volume of the void because otherwise we would get overlapping voids. The true volume of these typical voids is $V_{t,i}$, so that we get

$$n_i V_{t,i} = \frac{V_{voids}}{p} \Rightarrow n_i = \frac{V_{voids}}{p V_{t,i}} \ . \tag{7.19}$$

The typical volumes are shown in figure 7.7, the volume distribution in table 7.1. The largest voids occur fewer than one times in this volume, but this is not a problem since we use this as a weight for making an average volume.

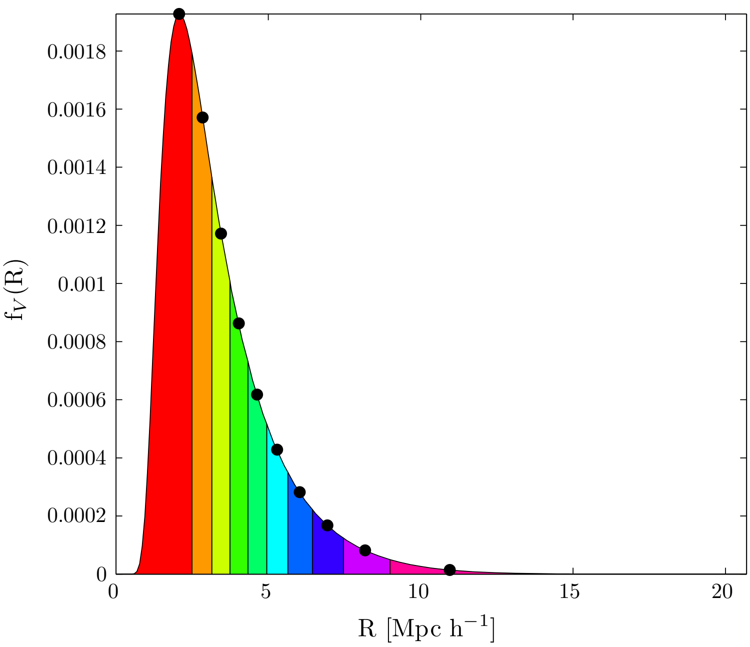

Figure 7.7: Typical volumes for 10 voids from the Sheth-Van de Weygaert distribution, plotted in the volume distribution function $f(V)$. The voids have been selected by volume, here the radial coordinate is the radius R. This makes the binning more apparent.

i	V_{i-1} [(Mpc h^{-1})^3]	V_i [(Mpc h^{-1})^3]	V_{typ} [(Mpc h^{-1})^3]	R [Mpc h^{-1}]	n_i
1	0.0	55.7	33.3	2.0	3.6
2	55.7	105.0	79.4	2.7	2.7
3	105.0	167.8	134.1	3.2	2.2
4	167.8	250.5	205.8	3.7	1.8
5	250.5	362.5	301.8	4.2	1.5
6	362.5	519.1	433.8	4.7	1.2
7	519.1	750.6	623.4	5.3	1.0
8	750.6	1127.7	917.7	6.0	0.8
9	1127.7	1888.5	1447.3	7.0	0.6
10	1888.5	21102.7	3257.4	9.2	0.4

Table 7.1: Typical void sample for a 150 h^{-1} Mpc box. The distribution was found using $\delta_v = -2.81$ and $\delta_c = 1.69$ and adiabatic CDM with Zel'dovich primordial spectrum.

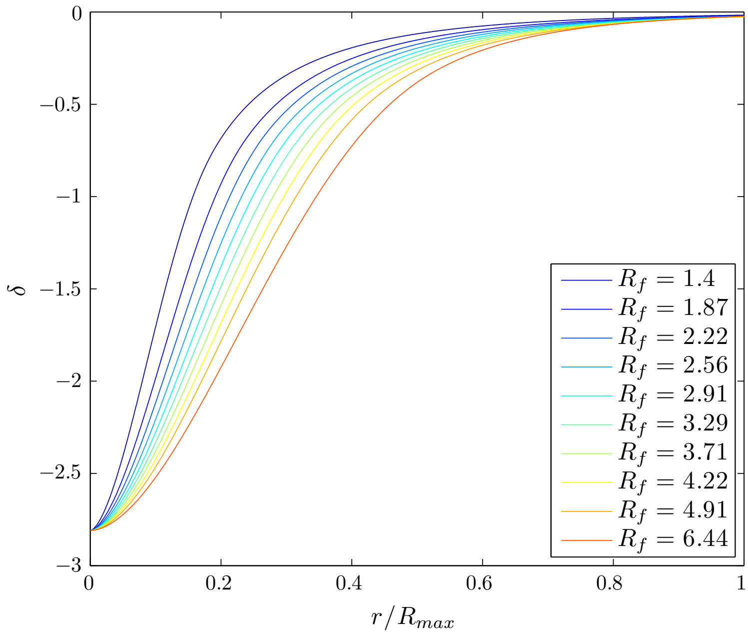

Figure 7.8: The voids from table 7.1 plotted versus radius in units of R_{max} (see equation 7.14). The actual voids are much broader but then they would not fit in one image. The large voids are less steep, while the small voids are much steeper. Instead of R in units of h^{-1} Mpc, the radii here are in Mpc

7.5 Connecting the voids

One final step in the model is to put the separate pieces together. Between the voids we have a homogeneous universe, while the voids are inhomogeneous. We recognize that the averages should be performed over whole space, while we would actually perform them per void. For a scalar S that is defined on the whole box we then find

$$\langle S \rangle_{box} = \lambda_b S_b + \sum_i \lambda_i \langle S \rangle_i \ , \tag{7.20}$$

with λ_i the volume weight factors for the voids and λ_b the weight factor for the intermediate space,

$$\lambda_i = n_i \frac{V_i}{V_{box}} \ , \tag{7.21}$$

$$\lambda_b = 1 - \sum_i \lambda_i \ . \tag{7.22}$$

No boundary conditions have been applied on the growth of the voids. The volumes in these equations evolve in time, so at one point it may happen that the total volume goes beyond the volume in the box. In that case the model breaks down and the background universe is subtracted from the average. We should therefore monitor the volume fraction of voids, if it comes even near 1 then we should stop. However, as a toy model this suffices.

We can simply describe each separate void using the spherical model, and then use the above formulas to describe the box as a whole. The averaging over the whole box will effectively dilute the effect of backreaction, because there is no backreaction on the space between the voids. With a typical volume filling factor of 0.2, we already can assume that the backreaction will be diluted by a factor of 5 over the whole volume.

In the next section we will see how the backreaction behaves in these voids and discuss our findings.

8

Results and discussion

In this section we will first discuss the effect of backreaction in a simplified void. This will stand as an example when we look at the typical voids in the void distribution for the Swiss cheese. Finally, we will compare the results of this work with the work of others.

8.1 Backreaction in a simple void

To show the magnitude of backreaction we computed its effects for a smooth 5 Mpc void. The profile was computed up to 120 Mpc to show the long-ranging effects of voids.

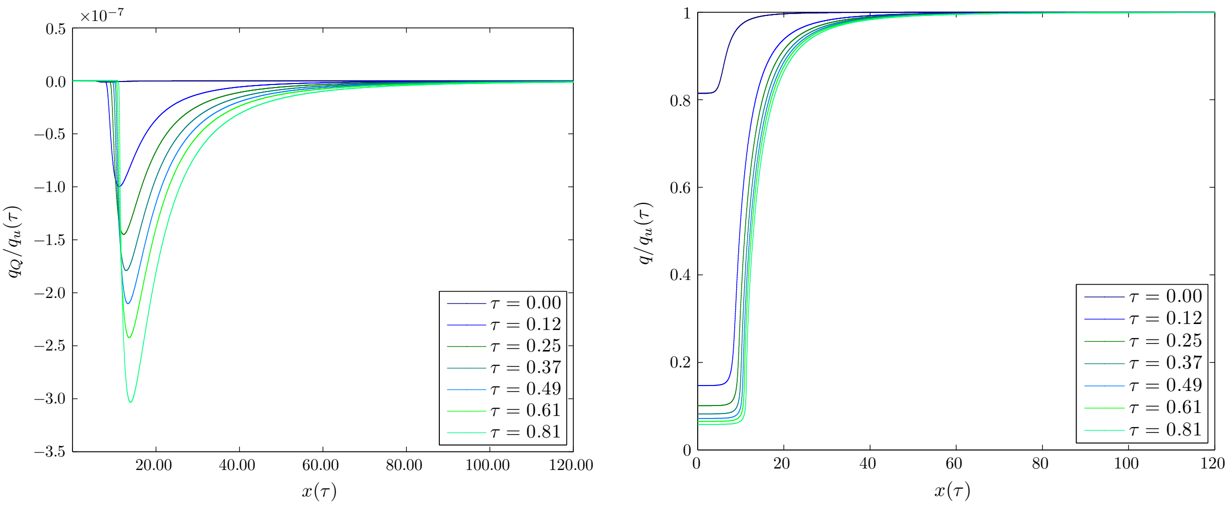

Figure 8.1: The deceleration by backreaction up to $a = 1$ for a simulated void ($\delta^L = -10$, $R = 5$ Mpc), using a hyperbolic tangent as a smooth step function. Horizontally is the comoving radius x in Mpc. The left image show the deceleration caused by $\mathcal{Q}_\mathcal{D}$, the right image shows the total deceleration for the same voids (see equation 5.30). Backreaction is clearly not able to provide an apparent acceleration.

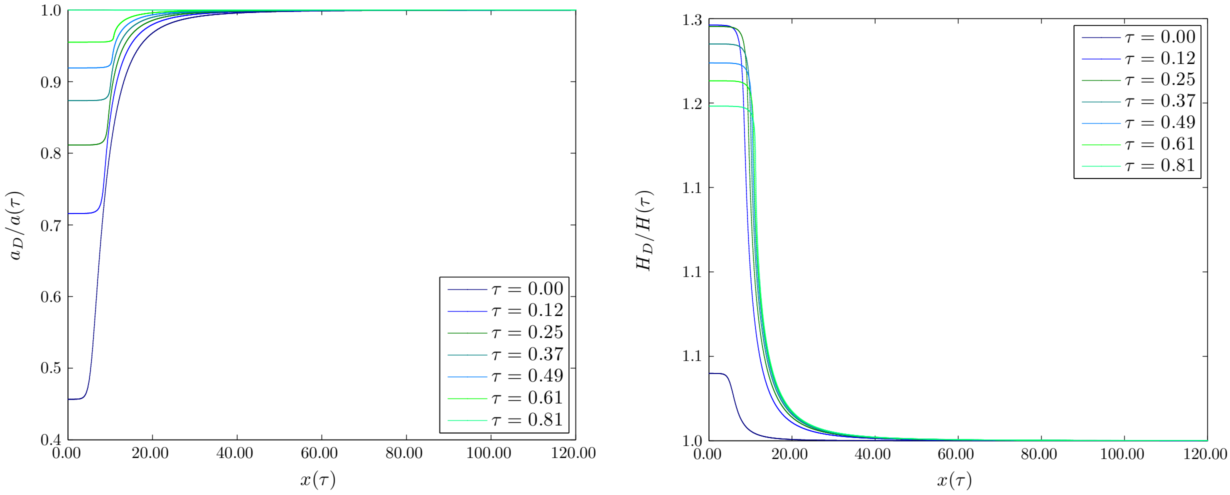

Figure 8.2: The average expansion factor $a_{\mathcal{D}}$ and the average Hubble parameter $H_{\mathcal{D}}$ relative to the background for the void in figure 8.1. The existence of the void is nearly unnoticeable at around 40 Mpc. The expansion factor seems to lag behind because of the normalization of $a_{\mathcal{D}}$ to t_0. This void is steeper and has a larger empty region than a typical CDM void (compare for example with figure 4.5).

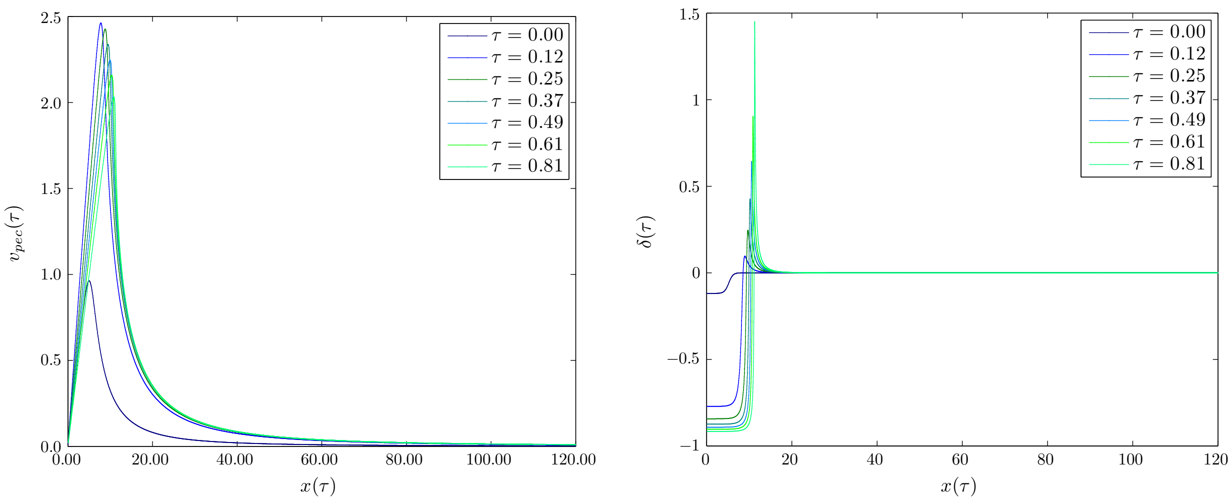

Figure 8.3: The true peculiar velocities v_{pec} and overdensity δ for the void from figure 8.1. We see the development of a strong ridge around the void. This void is much emptier in the centre and steeper at the edge than typical CDM voids that we used for the Swiss cheese.

Figure 8.1 shows the deceleration caused only by the backreaction, so without the matter term (see equation 5.30). We see that it causes a small acceleration which is completely overshadowed by the deceleration of the universe.

The average dynamics of this void is shown in figure 8.2. We see that the average expansion $a_{\mathcal{D}}$ and the average Hubble rate $H_{\mathcal{D}}$ in the void are different inside the void, while outside the void this effect decays down. At around 40 Mpc the presence of the void is nearly unnoticable in the expansion. Finally, figure 8.3 shows the corresponding peculiar velocity field v_{pec} and overdensity δ.

8.2 CDM voids

The results for the simple void are similar to what we find for the CDM voids that we defined in table 7.1. Figure 8.4 shows an example of these voids. The backreaction is even smaller and is again negligible. The cheese model would only dilute the backreaction even more, so that we can safely conclude that the effect of backreaction in this model is not large enough to cause an apparent acceleration.

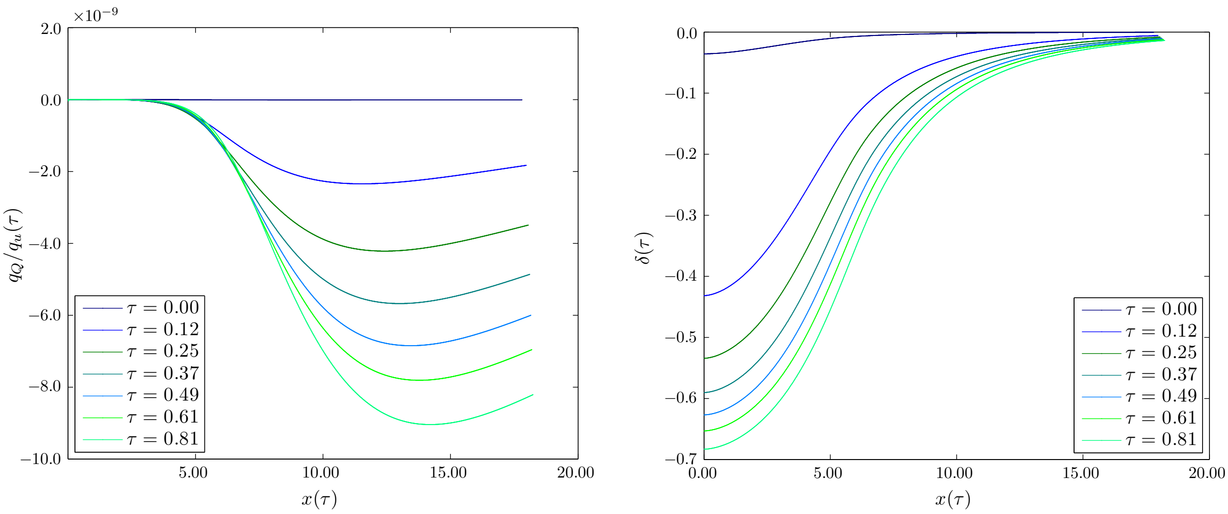

Figure 8.4: The deceleration by backreaction up to $a = 1$ for the 5th void from table 7.1. On the horizontal axes is the comoving radius x in Mpc. The left image show the deceleration caused by $\mathcal{Q}_{\mathcal{D}}$, the right image shows the density profile. These voids are less deep ($\delta^L = -2.81$) and also a lot less steep than the simple void from figure 8.1. Apparently this causes even less backreaction than for the simple void. The backreaction in the simple void was plotted for an enormous radius, while here the radius is more limited. We can see that the backreaction has not reached the zero level yet within this radius.

That the backreaction is small can already be seen from the size of the curvature. The effect of the backreaction arises from the mismatch between the terms

$$\frac{2}{3}\langle\theta\rangle^2 \quad \text{and} \quad \left\langle \frac{2}{3}\theta^2 - \sigma^2 \right\rangle , \tag{8.1}$$

i	x_{max}	$q/q_u(x_{max})$	$-q_{\mathcal{Q}}/q_u(x_{max})$	$H_{\mathcal{D}}(x_{max})/H_u$	$a_{\mathcal{D}}(x_{max})/a$
1	14.9703	0.14184	2.4744×10^{-10}	1.0068	1
2	15.981	0.13977	4.5958×10^{-10}	1.0086	1
3	16.7481	0.13839	6.643×10^{-10}	1.0098	1
4	17.483	0.13719	8.9473×10^{-10}	1.0109	1
5	18.2342	0.13609	1.164×10^{-9}	1.0118	1
6	19.0391	0.13503	1.489×10^{-9}	1.0127	1
7	19.9467	0.13397	1.8994×10^{-9}	1.0137	1
8	21.0422	0.13284	2.4543×10^{-9}	1.0147	1
9	22.5255	0.13155	3.3056×10^{-9}	1.0158	1
10	25.7862	0.12941	5.559×10^{-9}	1.0178	1

Table 8.1: Table with the backreactions for the profiles described in the previous chapter. x_{max} is the maximum comoving radius of the void, q/q_u is the total average deceleration at that position, $q_{\mathcal{D}}/q_u$ the acceleration from the backreaction. The relative average Hubble rate is given by $H_{\mathcal{D}}/H$ and the relative expansion by $a_{\mathcal{D}}/a$. The main point is that the profiles may have been cut off too quickly, but that still the backreaction is negligible.

as we saw in equation 5.28. The non-vanishing backreaction occurs because the left term has a single average, while the right term is the square of an average. Only in the flat case they exactly cancel out. But we also saw that the curvature is small for typical sub-horizon voids (see equation 4.41). The Taylor expansion indicates that backreaction is only a second order effect at $\mathcal{O}(H_i^2 r_i^2/c^2) \approx 10^{-6}$, independent whether we treat voids or structures. Unless the variance of the expansion and the shear are somehow decoupled, we should find that the effect of backreaction is small. It seems therefore that at least in this model backreaction can be ruled out as a possible explanation for dark energy.

8.3 Discussion

Backreaction is a popular topic, and many workers in the field have tried to find significant effects. As it turns out, some models have brushed away part of the shear, and were therefore able to find a significant amount of backreaction. An example of such a model is found by just connecting an empty FRW region to an EdS region, both of which do not have shear (Räsänen 2006). This is not realistic because in reality a ridge will form around the junction between the two regions, and shell crossing should soon set in. Near the junction, significant shear will develop. And as we have seen, the shear is able to exactly compensate the expansion variance. Ignoring the shear is therefore a key ingredient in *overestimating* the effect of cosmic backreaction (see Mattsson & Mattsson 2010). The shear and the variance in the expansion can in principle be very large, but the backreaction is much smaller.

Strong critics of backreaction have relied mostly on perturbation theory. But the problem with perturbation theory is where to stop including higher order terms. Most often they rely on a first order perturbed Newtonian metric, with higher order density perturbations included. A thorough investigation in perturbation was done by Baumann et al. 2010, and they also found that backreaction cannot play a large role in cosmology. Typical sizes of the backreaction effect are around $\mathcal{O}(H_i^2 r_i^2/c^2)$ (Gruzinov et al. 2006) which corresponds to our results. Even a no-go theorem was drawn up (Kasai et al. 2006).

Some authors suggest that these studies miss that backreaction is strongest at the moment that inhomogeneities become non-linear, so that (low order) perturbation theory is not useful anymore (see Räsänen 2010 and Kolb et al. 2008 for a full overview of the discussion on perturbed cosmologies). They state that the equations of motion in that case become highly non-linear, and the validity of writing the metric as a perturbed Newtonian metric does not hold anymore. The full metric can then also not be transformed back to the perturbed Newtonian metric. But in an article by Alonso et al. (Alonso et al. 2010) it was shown that the LTB model is quite well reproduced by Newtonian N-body simulations, except for the most extreme voids. This therefore questions the argument that a full relativistic approach is necessary. Another argument is that we locally ($r \ll c/H_0$) are always allowed to adopt a Newtonian frame. But if the universe is inhomogeneous on many scales, then perhaps this argument is less convincing.

The essential difference between the two groups in the discussion seems therefore to revolve around the issue whether the cosmos is close to a FRW or Newtonian limit. If so, then perturbation theory rightfully indicates that backreaction is not essential. If space is locally very inhomogeneous and non-spherical, then backreaction might be strong enough to mimic dark energy, while the Buchert formalism could make the average behaviour to be comparable to that of an FRW universe with a cosmological constant.

Even though the Buchert formalism is radically conservative and quite elegant, at the same time precision cosmology provides us with more and more very well matching results. A side note here is that the limitations in the parameter space might be partially responsible for Λ. For a flat universe with $\Omega_m = 0.3$ a negligible radiation, we can only end up with $\Omega_\Lambda = 0.7$. Λ should be seen as an option, but perhaps not necessarily the only option for cosmology. The solution would be to find a model-independent language, that does really distinguish between the different cosmological models without relying too much on the assumptions in cosmology.

As for backreaction models, perhaps an interesting direction would be to step down from the spherical LTB models and to experiment with ellipsoidal models. The full shear could be analysed and perhaps in that case the shear and the variance in the expansion would decouple. In the LTB models, shear can not fully develop, as it is always restricted to a spherical shape.

9 Conclusion

We may conclude that Buchert formalism seems unable to produce any sizeable acceleration in spherical models of voids. Because the Swiss cheese model dilutes the backreaction even more, the effect for the box as a whole is even less significant. This indicates that the effect of backreaction by structure formation is minimal. Perhaps more advanced models that allow for elliptic evolution could find more significant effects of backreaction. The nature of backreaction seems such that it is even stronger suppressed in flat space. If our universe is almost flat, as observations indicate, then we should expect that backreaction is negligible. The general picture seems therefore that for our universe as a whole, the assumptions on homogeneity and isotropy are a valid starting point for cosmology.

The main answers on the goals for my project are therefore (ending with the main question):

- *How to integrate backreaction in the spherical model?* We have seen how to use spherical models, especially the Lemaître-Tolman-Bondi models, to find the effect of cosmic backreaction. In the spherical models, the shear and expansion can be written down directly so that the magnitude of the backreaction can be found.

- *How to generate a universe filled with voids (i.e. Swiss cheese)?* Using the Sheth-van de Weygaert mass function we have been able to construct a typical sample of voids in a cubic box. The general effect of this box is to dilute the magnitude of the backreaction. The cosmic backreaction is simply too weak to cause any acceleration of the average expansion of a void. We therefore have to conclude that the Swiss cheese step is unfortunately not of any use if the backreaction is small. With significant backreaction, the Swiss cheese would have been able to clarify how much backreaction would be found in a more realistic setting.

- *Can we obtain backreaction using spherical voids in a background universe?* We have seen that for spherical models the backreaction does not vanish if space is not flat. For flat models, the curvature vanishes which causes the variance in the expansion to cancel against the average squared shear. This is a realization of what Thomas Buchert already indicated in his 1997 article (Buchert & Ehlers 1997).

- **Is cosmic backreaction an alternative to dark energy?** Probably not. For typical spherical voids, the effects seems not nearly enough to cause an acceleration to the average expansion of the universe. This was already pointed out by several other articles, though they often relied on perturbation theory. However, N-body simulations of voids apparently give the same results as the LTB-models, so that the perturbation theory seems a valid approach, and cosmic backreaction can be ruled out, at least for (spherical) voids.

Another important issue is that in cosmology the observations rely heavily on the used assumptions and models. More attempts are needed to find model-independent observables that can be used to really distinguish between the different cosmological options. Or at least we need to find alternatives, because within the Friedmann framework there is no other choice than dark energy. But dark energy does not seem to be well understood yet. The Buchert formalism appeared a viable alternative, but since its effectiveness seems low we have to keep searching for other models that provide alternatives for dark energy or find a fundamental explanation for dark energy.

10

Acknowledgements

I would like to thank everyone that has helped with this work. First of all, I would like to thank Rien van de Weygaert for his ongoing support in this work as my supervisor. We have had many nice meetings and discussions, both on cosmological topics, as well about the world around us. I would also like to thank my colleagues that helped me correct this report, including Marlies, Patrick, Eva and Jarno. In general I would like to thank all students of Kapteyn, with whom I have had many animated lunches, coffee breaks, discussions, and much support during our studies. I would also like to thank the members of the Cosmology group, with their fascinating discussions (especially when Bernard Jones is around!) on many interesting topics. Special thanks also to Jakob as he has provided me with a very useful code to generate 2-D Gaussian random fields.

Groningen, February 2011

Bibliography

Alonso, D., García-Bellido, J., Haugbølle, T., & Vicente, J. 2010, Phys. Rev. D, 82, 123530

Amanullah, R., et al. 2010, ApJ, 716, 712

Bardeen, J. M., Bond, J. R., Kaiser, N., & Szalay, A. S. 1986, ApJ, 304, 15

Baumann, D., Nicolis, A., Senatore, L., & Zaldarriaga, M. 2010, ArXiv e-prints

Bertschinger, E. 1985, ApJS, 58, 1

Bond, J. R., Cole, S., Efstathiou, G., & Kaiser, N. 1991, ApJ, 379, 440

Bondi, H. 1947, MNRAS, 107, 410

Buchert, T. 2000, General Relativity and Gravitation, 32, 105

Buchert, T., & Ehlers, J. 1997, A&A, 320, 1

Buist, J. 2009, Dark Matter in the Solar System, Master Thesis

Célérier, M. 2007, ArXiv Astrophysics e-prints

Clifton, T., Ferreira, P. G., & Land, K. 2008, Physical Review Letters, 101, 131302

Clifton, T., Ferreira, P. G., & Zuntz, J. 2009, J. Cosmology Astropart. Phys., 7, 29

Einstein, A. 1915, Sitzungsberichte der Königlich Preußischen Akademie der Wissenschaften (Berlin), Seite 844-847., 844

Eisenstein, D. J., et al. 2005, ApJ, 633, 560

Friedman, A. 1922, Zeitschrift fur Physik, 10, 377

Friedmann, A. 1924, Zeitschrift fur Physik, 21, 326

Furlanetto, S. R., & Piran, T. 2006, MNRAS, 366, 467

Gruzinov, A., Kleban, M., Porrati, M., & Redi, M. 2006, J. Cosmology Astropart. Phys., 12, 1

Gunn, J. E., & Gott, III, J. R. 1972, ApJ, 176, 1

Guth, A. H. 1981, Phys. Rev. D, 23, 347

Heath, D. J. 1977, MNRAS, 179, 351

Hellaby, C., & Lake, K. 1985, ApJ, 290, 381

Hubble, E. 1929, Proceedings of the National Academy of Science, 15, 168

Icke, V. 1973, A&A, 27, 1

—. 1984, MNRAS, 206, 1P

Kapteyn, J. C. 1922, ApJ, 55, 302

Kasai, M., Asada, H., & Futamase, T. 2006, Progress of Theoretical Physics, 115, 827

Kolb, E. W., Marra, V., & Matarrese, S. 2008, Phys. Rev. D, 78, 103002

Komatsu, E., et al. 2011, ApJS, 192, 18

Lahav, O., Lilje, P. B., Primack, J. R., & Rees, M. J. 1991, MNRAS, 251, 128

Lahav, O., & Suto, Y. 2004, Living Reviews in Relativity, 7, 8

Lemaître, G. 1927, Annales de la Societe Scietifique de Bruxelles, 47, 49

—. 1933, Annales de la Societe Scietifique de Bruxelles, 53, 51

Lilje, P. B., & Lahav, O. 1991, ApJ, 374, 29

Linde, A. D. 1982, Physics Letters B, 108, 389

Mattsson, M., & Mattsson, T. 2010, J. Cosmology Astropart. Phys., 10, 21

McClure, M. L., & Dyer, C. C. 2007, New A, 12, 533

Nambu, Y., & Tanimoto, M. 2005, ArXiv General Relativity and Quantum Cosmology e-prints

Pandolfi, S., Cooray, A., Giusarma, E., Kolb, E. W., Melchiorri, A., Mena, O., & Serra, P. 2010, Phys. Rev. D, 81, 123509

Peacock, J. A. 1999, Cosmological Physics (Cambridge Astrophysics)

Peebles, P. J. E. 1980, The large-scale structure of the universe (Princeton University Press)

Percival, W. J. 2005, A&A, 443, 819

Perlmutter, S., et al. 1999, ApJ, 517, 565

Platen, E., van de Weygaert, R., & Jones, B. J. T. 2007, MNRAS, 380, 551

Press, W. H., & Schechter, P. 1974, ApJ, 187, 425

Räsänen, S. 2006, J. Cosmology Astropart. Phys., 11, 3

—. 2008, J. Cosmology Astropart. Phys., 4, 26

—. 2010, Phys. Rev. D, 81, 103512

Raychaudhuri, A. 1955, Physical Review, 98, 1123

Riess, A. G., et al. 1998, AJ, 116, 1009

Robertson, H. P. 1935, ApJ, 82, 284

Schramm, D. N., & Turner, M. S. 1998, Reviews of Modern Physics, 70, 303

Shandarin, S., Feldman, H. A., Heitmann, K., & Habib, S. 2006, MNRAS, 367, 1629

Sheth, R. K., & van de Weygaert, R. 2004, MNRAS, 350, 517

Spergel, D. N., et al. 2003, ApJS, 148, 175

Springel, V., et al. 2005, Nature, 435, 629

Stanton, S. J. 2011, Celestial Mechanics, Encyclopaedia Britannica

Starobinsky, A. A. 1982, Physics Letters B, 117, 175

Sussman, R. A. 2008, ArXiv e-prints

—. 2010, Classical and Quantum Gravity, 27, 175001

Tegmark, M., et al. 2004, Phys. Rev. D, 69, 103501

Tolman, R. C. 1934, Proceedings of the National Academy of Science, 20, 169

Tomita, K. 2009, ArXiv e-prints

van de Weygaert, R. 1995, Notes on the Spherical Model, private notes

—. 2005, Notes Linear Perturbation Theory, Private notes

van de Weygaert, R., & Platen, E. 2009, ArXiv e-prints

Walker, A. G. 1935, The Quarterly Journal of Mathematics, 6, 81

Zeilik, M., & Gregory, S. 1998, Introductory Astronomy and Astrophysics (Harcourt College Publishers)

Zel'Dovich, Y. B. 1970, A&A, 5, 84